5 Depth-sensing Nanoindentation Techniques for Nanomechanical Characterization

Bharat Bhushan

Abstract
To measure nanomechanical properties of surface layers of bulk materials and thin films, depth-sensing nanoindentation measurement techniques are used commonly. The nanoindentation apparatus continuously monitors the load and the position of the indenter relative to the surface of the specimen (depth of an indent or displacement) during the indentation process. Indentation experiments can be performed at a penetration depth of as low as about 5 nm. This chapter presents an overview of various nanoindentation techniques, various measurement options, and data analysis. Data on elastic-plastic deformation behavior, hardness, elastic modulus, scratch resistance, film-substrate adhesion, residual stresses, time-dependent creep and relaxation properties, fracture toughness, and fatigue are presented.

Keywords
Nanoindentation · Depth-sensing nanoindentation · Picoindentation · Continuous stiffness · Thin films · Hardness · Elastic modulus · Scratch resistance · Adhesion · Stiffness · Creep · Toughness · Fatigue

5.1 Introduction

Mechanical properties of solid surfaces and thin films are important in various applications including those requiring tribological performance (Bhushan 1996, 1999a, 2001, 2011, 2013a, b, 2017). Among the mechanical properties of interest are elastic-plastic deformation behavior, hardness, elastic modulus, scratch resistance, film-substrate adhesion, residual

B. Bhushan (✉)
Nanoprobe Laboratory for Bio- and Nanotechnology and Biomimetics, The Ohio State University, 201 W. 19th Ave., W390 Scott Laboratory, Columbus, OH 43210, USA
e-mail: bhushan.2@osu.edu

© Springer International Publishing AG 2017
B. Bhushan (ed.), *Nanotribology and Nanomechanics*,
DOI 10.1007/978-3-319-51433-8_5

stresses, time-dependent creep and relaxation properties, fracture toughness, and fatigue. Indentation measurements can assess structural heterogeneities on and underneath the surface such as the presence of buried layers, grain boundaries, graded material, and multilayered structures. These properties can be obtained using commercial and specialized indentation testers.

Physical contacts between sliding interfaces in magnetic storage devices and micro/nanoelectromechanical systems (MEMS/NEMS) occur at very low loads. Thus, friction and wear of sliding surfaces is controlled primarily by the physical and chemical properties of a few surface atomic layers. Ultrathin films, as thin as 1–2 nm, and nanocomposites are used in many applications including magnetic storage devices and MEMS/NEMS (Bhushan 1996, 2017). Measurements of surface layers and ultrathin films and nanocomposites require specialized instrumentation. Depth-sensing nanoindenter and atomic force microscope (AFM) are used commonly for measurements on the nanoscale (Bhushan et al. 1996a; Bhushan 1999a; Bhushan and Li 2003).

Mechanical properties of materials on the nanoscale are size-dependent (Bhushan et al. 1996a, 2014; Bhushan and Li 2003). Nanomechanical characterizations have been motivated partly by the development of nanocomposites and the application of nanometer-thick films for miniaturization of engineering and electronic components, and partly by newly available methods of probing mechanical properties in small volumes. Compared to their bulk material counterparts, nano-objects exhibit enhanced mechanical, electrical, magnetic, chemical, friction, and wear-reducing properties (Bhushan et al. 2014; Maharaj and Bhushan 2015). Nano-objects include nanoparticles, nanorods, and nanowires. Nanomechanical characterization of nano-objects is needed.

A depth-sensing nanoindenter is an important tool for probing the mechanical properties of small volumes of material. Indentation load-displacement data contain a wealth of information. From the load-displacement data, many mechanical properties such as hardness and elastic modulus can be determined without imaging the indentation impression. The nanoindenter also has been used to measure the fracture toughness and fatigue properties of ultrathin films, which cannot be measured by conventional indentation tests. Nanoscratch, nanowear, and adhesion tests can be performed at ramping loads using a tangential force sensor. AFMs are ideal for imaging of nanometer-scale indents, providing useful information about nanoindentation deformation (Bhushan 1999a, 2011, 2017). When an indentation system is used in conjunction with an AFM, in situ imaging can be obtained.

In this chapter, we review two commercial depth-sensing nanoindentation test apparatuses, followed by various measurement options, data analysis, and their use for determination of various mechanical properties of interest (Bhushan et al. 1996a; Bhushan 1999a, 2011; Bhushan and Li 2003). Emphasis here is on measurements of surface layers of bulk materials and ultrathin films at shallow indentation depths as small as 5–20 nm.

5.2 Nanoindentation Measurement Techniques and Data Analysis

Hardness measures resistance to local deformation. The most commonly used hardness measurements are: scratch hardness and static indentation hardness (Tabor 1951). Scratch hardness is the oldest form of hardness measurement. It depends on the ability of one material to scratch another or to be scratched by another solid. Solid and thin-film surfaces are scratched by a sharp stylus made of hard material, typically diamond. As a measure of scratch hardness and/or interfacial adhesion, either the loads required to scratch or fracture the surface or delaminate the film are used or the normal/tangential load-scratch size relationships are used (Heavens 1950; Tabor 1951, 1970; Benjamin and Weaver 1960; Campbell 1970; Ahn et al. 1978; Bhushan 1987; Wu 1991; Bhushan et al. 1995, 1996a; Bhushan and Gupta 1995; Hainsworth et al. 1996; Blau et al. 1997; Bhushan 1999a; Bhushan and Li 2003).

The methods most widely used in determining the hardness of materials are the (quasi) static indentation methods. Indentation hardness is essentially a measure of the plastic deformation properties of materials and only to a secondary extent a measure of their elastic properties. There is a large hydrostatic component of stress around the indentation, and since this plays no part in plastic flow, the indentation pressure is appreciably higher than the uniaxial flow stress of the materials. For many materials, the indentation pressure is about three times as large, but if the material shows appreciable elasticity, the yielding of the elastic hinterland imposes less constraint on plastic flow and the factor of proportionality may be considered less than 3. Indentation hardness depends on the time of loading and on the temperature and other operating environmental conditions. In the indentation tests, a spherical, conical, or pyramidal indenter is forced into the surface of the material, which forms a permanent (plastic) indentation in the surface of the material to be examined. The hardness number (GPa or kg/mm^2), equivalent to the average pressure under the indenter, is calculated as the applied normal load divided by either the curved (surface) area (Brinell, Rockwell, and Vickers hardness numbers) or the projected area (Knoop and Berkovich hardness numbers) of the contact between the indenter and the material being tested under load (Lysaght 1949; Berkovich 1951; Tabor 1951, 1970; Mott 1957; O'Neill 1967; Westbrook and Conrad 1973; Blau and Lawn 1986; Bhushan and Gupta 1997; VanLandingham et al. 2001; Fisher-Cripps 2002).

In a conventional indentation hardness test, the contact area is determined by measuring the indentation size using a microscope after the sample is unloaded. For metals, there is a small change in the size of the indentation on unloading so that the conventional hardness test is essentially a test of hardness under load, although it is subject to some error due to varying elastic contraction of the indentation (Stilwell and Tabor 1961). The first depth-sensing indentation hardness test was developed in the early 1980s. In this test, the contact area is determined by measuring the indentation depth during the loading/unloading cycle (Pethica et al. 1983; Nastasi et al. 1993; Bhushan et al. 1996a; Bhushan and Gupta 1997; Bhushan 1999a; Bhushan and Li 2003). Hardness data can be obtained without imaging the indentations with high reproducibility. This is useful particularly for small indents required for hardness measurements at very shallow depths. Depth measurements have, however, a major weakness arising from "piling-up" and "sinking-in" of material around the indentation. The measured indentation depth needs to be corrected for the depression (or the hump) of the sample around the indentation before it can be used for calculation of the hardness (Doerner and Nix 1986; Doerner et al. 1986; Nix 1989; Oliver and Pharr 1992). Elastic modulus is the slope of the stress-strain curve in the elastic regime. It can obtained from the slope of the unloading curve (Oliver and Pharr 1992).

In addition to measurements of hardness and elastic modulus, static indentation tests have been used for measurements of a wide variety of material properties such as elastic-plastic deformation behavior (Pethica et al. 1983; Doerner and Nix 1986; Fabes et al. 1992; Oliver and Pharr 1992; Bhushan et al. 1996a; Bhushan 1999a; Bhushan and Li 2003), flow stress (Tabor 1951), scratch resistance and film-substrate adhesion (Heavens 1950; Tabor 1951; Benjamin and Weaver 1960; Campbell 1970; Ahn et al. 1978; Bhushan 1987; Wu 1991; Bhushan et al. 1995, 1996a; Bhushan and Gupta 1995; Gupta and Bhushan 1995a, b; Blau et al. 1997), residual stresses (Swain et al. 1977; Marshall and Lawn 1979; LaFontaine et al. 1991), creep (Westbrook 1957; Mulhearn and Tabor 1960; Atkins et al. 1966; Walker 1973; Chu and Li 1977; Li et al. 1991; Raman and Berriche 1992; Bhushan et al. 1996a), stress relaxation (Chu and Li 1980; Mayo and Nix 1988; LaFontaine et al. 1990; Wu 1991; Nastasi et al. 1993; Bhushan et al. 1996a), fracture toughness and brittleness (Lawn et al. 1980; Chantikul et al. 1981; Lawn 1993; Bhushan et al. 1996a, b; Li et al. 1997; Hainsworth et al. 1998; Li and Bhushan 1998a), and fatigue (Li and Chu 1979; Wu et al. 1991; Li and Bhushan 2002b, c).

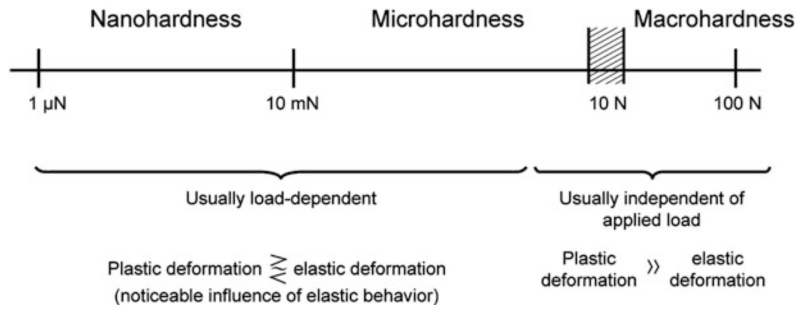

Fig. 5.1 Extended load range of static indentation hardness testing

The extended load range of static indentation testing is shown schematically in Fig. 5.1. We note that only the lower micro- and nanohardness load range can be employed successfully for measurements of extremely thin (submicron-thick) films. The intrinsic hardness of surface layers or thin films becomes meaningful only if the influence of the substrate material can be eliminated. The minimum load for most commercial microindentation testers available is about 10 mN. Loads on the order of 1 μN or less to 1 mN are desirable if the indentation depths are required to be a few nanometers. In this case, the indentation size sometimes reaches the resolution limit of a light microscope, and it is impossible to find such a small imprint if the measurement is made with a microscope after the indentation load has been removed. Hence, either the indentation apparatuses are placed in situ a scanning electron microscope (SEM) or in situ indentation depth measurements are made. In addition, the latter measurements would offer the advantages of observing the penetration process itself. In viscoelastic/viscoplastic materials, since indentation size changes with time, in situ measurements of the indentation size are particularly useful. In addition, they can provide more complete creep and relaxation data for the materials.

In this section, we will review two commercial depth-sensing nanoindentation test apparatuses, followed by data analysis and various measurement options.

5.2.1 Nanoindentation Apparatuses

Earlier research by Alekhin et al. (1972), Ternovskii et al. (1973), and Bulychev et al. (1975, 1979) led to the development of depth-sensing apparatuses (Pethica et al. 1983). In the depth-sensing indentation apparatus, the load-indentation depth is monitored continuously during the loading and unloading processes (Newey et al. 1982; Pethica et al. 1983; Wierenga and Franken 1984; Bhushan et al. 1985, 1988; Hannula et al. 1986; Wierenga et al. 1986; Tsukamoto et al. 1987; Williams et al. 1988; Yanagisawa and Motamura 1987; Wu et al. 1988; Loubet et al. 1993; Bhushan et al. 1996a; Randall et al. 1996). For detailed reviews, see Bhushan (1999a) and Bhushan and Li (2003).

In commercially available nanoindenters, an indenter is pushed into the sample until bulk plastic deformation occurs, and then unloaded. Indentation load is applied by various methods including using an electromagnet or electrostatic actuation. The indentation displacement is measured in situ using a capacitive displacement sensor in almost all cases. The apparatus continuously monitors the load and the position of the indenter relative to the surface of the specimen (depth of an indent) during the indentation process. The area of the indent is then calculated from a knowledge of the geometry of the tip of the diamond indenter.

5.2.1.1 General Description and Principle of Operation

Commercially available nanoindenters are made by various companies. The major manufacturers include Keysight Technologies, Santa Rosa, CA, U.S.A. (first major manufacturer established in the mid-1980s as Nano Instruments, Inc., Knoxville, TN, later acquired by MTS System Corp., followed by Agilent Technologies), Micro Materials, Wrexham, U.K., and CSM Instruments Inc., Neuchâtel, Switzerland. These can be used with a minimum indentation depth of about 20 nm. Hysitron Inc., Minneapolis, MN, launched in the late 1990s, used an AFM platform and electrostatic actuation for loading/unloading. The minimum depth achieved was about 10 nm, and it remains a major research tool (Bhushan et al. 1996a). One of the benefits of this apparatus is that the nanoindenter head can be used to replace the AFM head in a commercial AFM without requiring new scanning and imaging capabilities.

Next we briefly describe the Keysight and Hysitron indenters.

Keysight Nanoindenter

Initial development of this apparatus has been described by Pethica et al. (1983) and Oliver et al. (1986). Mechanical properties measurements can be made at a minimum penetration depth of about 20 nm (or a plastic depth of about 15 nm) (Oliver et al. 1986). Specifications and commonly-used operating parameters for a commercial nanoindenter are given in Table 5.1 (Anonymous 2014).

The nanoindenter consists of three major components: the indenter head, an X–Y–Z motorized precision table for positioning and transporting the sample, and an AFM and/or optical microscope, Fig. 5.2a. The load on the indenter is generated using a voice-coil in a permanent magnet assembly attached to the top of the indenter (loading) column. The generated load is simply the vector product of the current through the coil and the magnetic field strength of the permanent magnet. This type of load application allows for very fast, closed-loop feedback control over the displacement as it completely separates the load application system and the displacement measuring system. Various interchangeable indenter heads are available with load ranges typically from 0 to 500 mN, with a high-load option up to 10 N. The displacement of the indenter is measured using a three-plate capacitive displacement sensor. All three plates are circular disks approximately 1.5 mm thick. The two outer plates have a diameter of approximately 50 mm, and the inner, moving plate is half that size. The indenter column is attached to the moving plate. Two outer plates are maintained at equal and opposite drive voltages (2 V at 12.5 kHz). The output voltage of the center pick-up plate is related to the position of that plate in the capacitive gap uniquely. The pick-up voltage is measured using an analog to digital converter (ADC) running at a typical rate of 4 kHz. The displacement system is calibrated using a laser-interferometer. This plate-and-indenter assembly is supported by two leaf springs cut to have very low stiffness. The motion is damped by airflow around the central plate of the capacitor, which is attached to the loading column. At the bottom of the indenter rod, an indenter, typically a three-sided pyramidal diamond tip (Berkovich indenter, to be discussed later) is attached.

The indenter head assembly is attached to the "U" beam rigidly, below which the X–Y–Z table rides, Fig. 5.2a. An AFM and/or optical microscope is also attached to the beam for in situ imaging capabilities. The position of an indent on a specimen is selected using either an optical microscope or the AFM. The specimens are held on an X–Y–Z table whose position relative to the microscope or the indenter is controlled. The spatial resolution of the position of the table in the X–Y plane is on the order of 100 nm. The three components just described are enclosed in a cabinet to ensure the thermal stability of the samples. The entire apparatus is placed on a vibration-isolation table.

A continuous stiffness measurement (CSM) option (to be described later) can be used to make continuous measurements of the stiffness

Table 5.1 Typical specifications and commonly-used operating parameters in Keysight Nano Indenter G200 (Anonymous 2014)

Standard XP indentation head	
Displacement resolution	<0.01 nm
Total indenter travel	1.5 mm
Maximum indentation depth	>500 µm
Load application	Coil/magnet assembly
Displacement measurement	Capacitance gauge
Loading capability Maximum load (standard) Maximum load with DCM II option Maximum load with High Load option Load resolution Contact Force Load frame stiffness	500 mN 30 mN 10 N 50 nN <1.0 µN $\sim 5 \times 10^6$ N/m
Indentation placement Useable surface area Position control Position accuracy	100 mm × 100 mm Automated remote with mouse 1 µm
Microscope Video screen Objective	25× 10× and 40×
DCM II indentation head option	
Displacement resolution	<1 nm
Range of indenter travel	70 µm
Loading column mass	<150 mg
Load application	Coil/magnet assembly
Displacement measurement	Capacitance gauge
Typical leaf spring stiffness	~100 N/m
Typical damping coefficient	0.02 Ns/m
Typical resonant frequency	120 Hz
Lateral stiffness	80.000 N/m
Loading capability Maximum load Load resolution	30 mN (13 g) 3 nN (0.3 µg)
Express test option	
Time per indentation	Standard <5.0 s
LFM option	
Maximum lateral force	>250 mN
Lateral resolution	<2 µN
Maximum scratch distance	>100 mm
Scratch speed	100 nm/s up to 2 mm/s
High load option	
Maximum force	10 N
Load resolution	≤1 mN

(continued)

Table 5.1 (continued)

Maximum indentation depth	≥ 500 μm
Displacement resolution	0.01 nm
Frame stiffness	≥ 5 × 10^6 N/m
NanoVision option	
X-Y scan range	100 μm × 100 μm
Z scan range	Indentation head dependent
Positioning accuracy	≤ 20 nm
Resonant frequency	>120 Hz

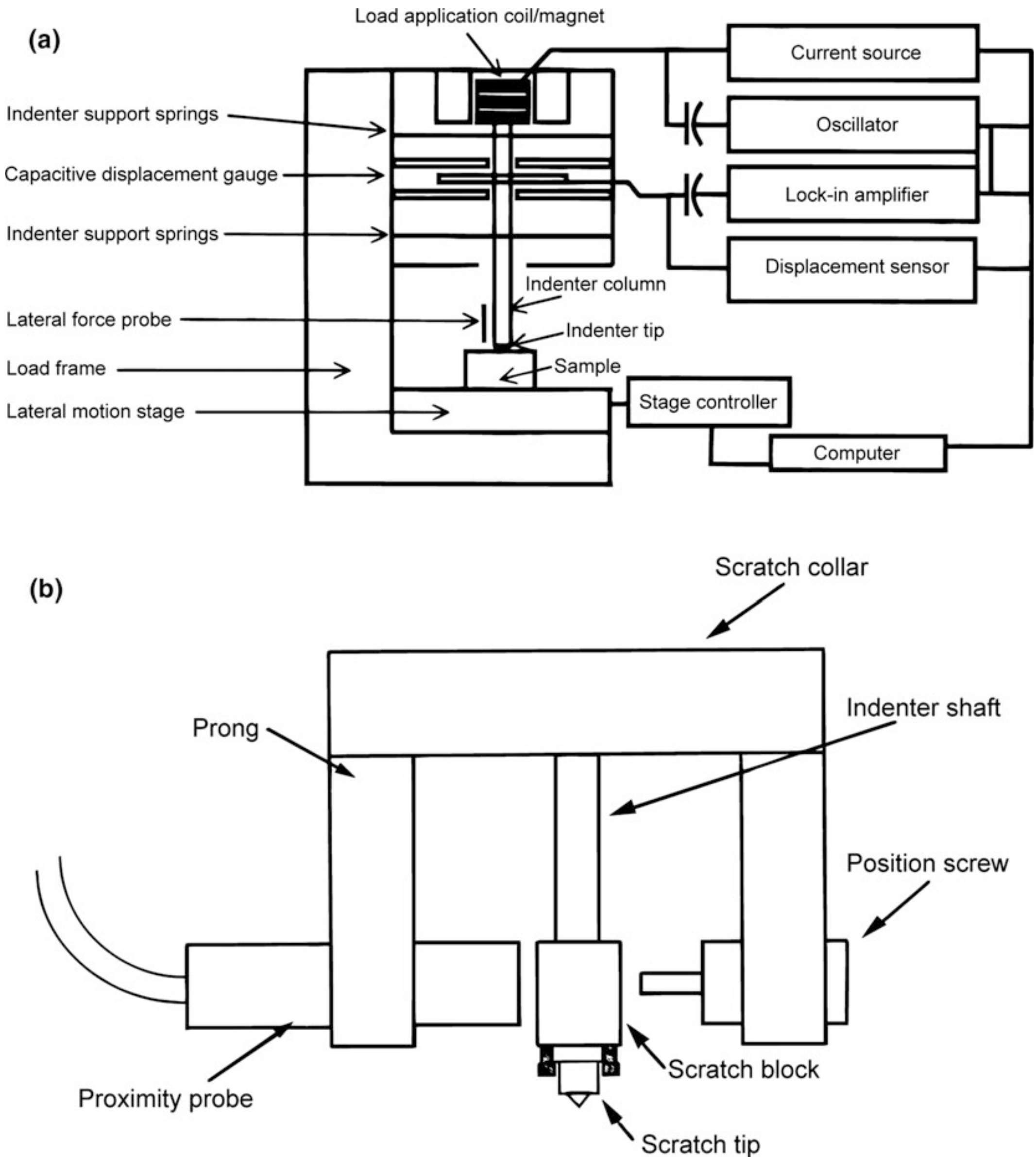

Fig. 5.2 Schematics of an Keysight nanoindenter design **a** showing the major components: the indenter head, a X–Y–Z motorized precision table, and tangential force option, and **b** detailed schematic of the tangential force option hardware (not to scale) (adapted from Keysight brochures)

of a sample, which allows the elastic modulus to be calculated as a function of time (or indentation depth) (Pethica and Oliver 1989; Li and Bhushan 2002a). Because of the relatively small time constant of the measurements, the device is particularly useful in studies of time-dependent properties of materials.

Hysitron Nanoindenter

For nanometer-scale indentation depths, in situ capabilities of imaging of the indents at extremely high magnifications is desirable. AFMs are ideal for in situ imaging of surfaces before and after indentation. They have been used for indentation studies with nanometer-scale depths (Bhushan and Koinkar 1994; Bhushan et al. 1995). However, load-displacement curves cannot be obtained with high accuracy for the following reasons. First, to obtain the indentation depth, the sample displacement needs to be subtracted from the tip displacement, requiring subtraction of two large numbers. Second, piezoelectric transducers (PZTs) generally are used for sample motion, which exhibit nonlinearity, hysteresis, and creep. Nonlinearity can be corrected; however, hysteresis and creep can result in displacements on the order of the indentation depths of interest. Finally, a large, lateral deflection of the cantilever beam may be required to apply high loads, which changes the indentation location during loading.

An indentation system with a three-plate transducer with electrostatic actuation for loading/unloading applications and capacitive sensor for displacement measurements was developed by Hysitron Inc. The system can apply loads ranging from 1 μN or less to 10 mN directly, and make load-displacement measurements with subnanometer indentation depth resolution (Bhushan et al. 1996a). When used in conjunction with an AFM, in situ imaging also can be obtained. A schematic of the indentation system using an AFM (such as from Bruker Instruments) as a platform is shown in Fig. 5.3a (Bhushan et al. 1996a). The indentation system consists of a three-plate transducer with electrostatic actuation hardware used for direct application of normal load, and a capacitive sensor used for measurements of vertical displacement (Fig. 5.3b). The AFM head is replaced with this transducer head, and the sample is mounted on the PZT scanner. The transducer has a three-plate (Be–Cu) capacitive structure, which provides high sensitivity, a large dynamic range, and a linear output signal with respect to load or displacement. The tip is connected to the center plate, which is spring mounted to the housing. Four springs are mounted on the top and another four are mounted at the bottom with a total stiffness of about 100 Nm^{-1}. A titanium shank brazed to the diamond indenter tip is glued to a glass-reinforced plastic (Ryton) holder, which, in turn, is screwed into the center plate (Fig. 5.3c).

Vertical displacement of the tip (indentation depth) is measured by measuring the displacement of the center electrode relative to the two outer electrodes using the capacitance technique. During measurements, the sample remains stationary. The load is applied by an electrostatic force generated between the center (pick-up) electrode and drive plate (upper or lower) when a voltage is applied to the drive plate. The applied load is proportional to the square of the voltage. The load resolution is 100 nN or better, and the displacement resolution is 0.1 nm. A load range of 1 μN–10 mN typically is used. Loading rates can be varied, changing the load–unload period typically from 180 to 950 s. The AFM functions as a platform for the indenter system and also provides in situ imaging before and after indentation with a lateral resolution of about 10 nm and a vertical resolution of about 0.2 nm. Load-displacement data during loading and unloading are obtained as contact depth as low as 5–10 nm. A continuous stiffness option is also available. The instrument also can be used for scratching, wear, and adhesion studies (Palacio and Bhushan 2010; Kumar and Bhushan 2015; Cho and Bhushan 2016).

This instrument also can be installed inside an SEM or TEM to allow in situ imaging of the indentation process.

5.2.1.2 The Indenters

The indenter should have a high elastic modulus, virtually no plastic deformation, low friction, smooth surface, and a well-defined geometry that

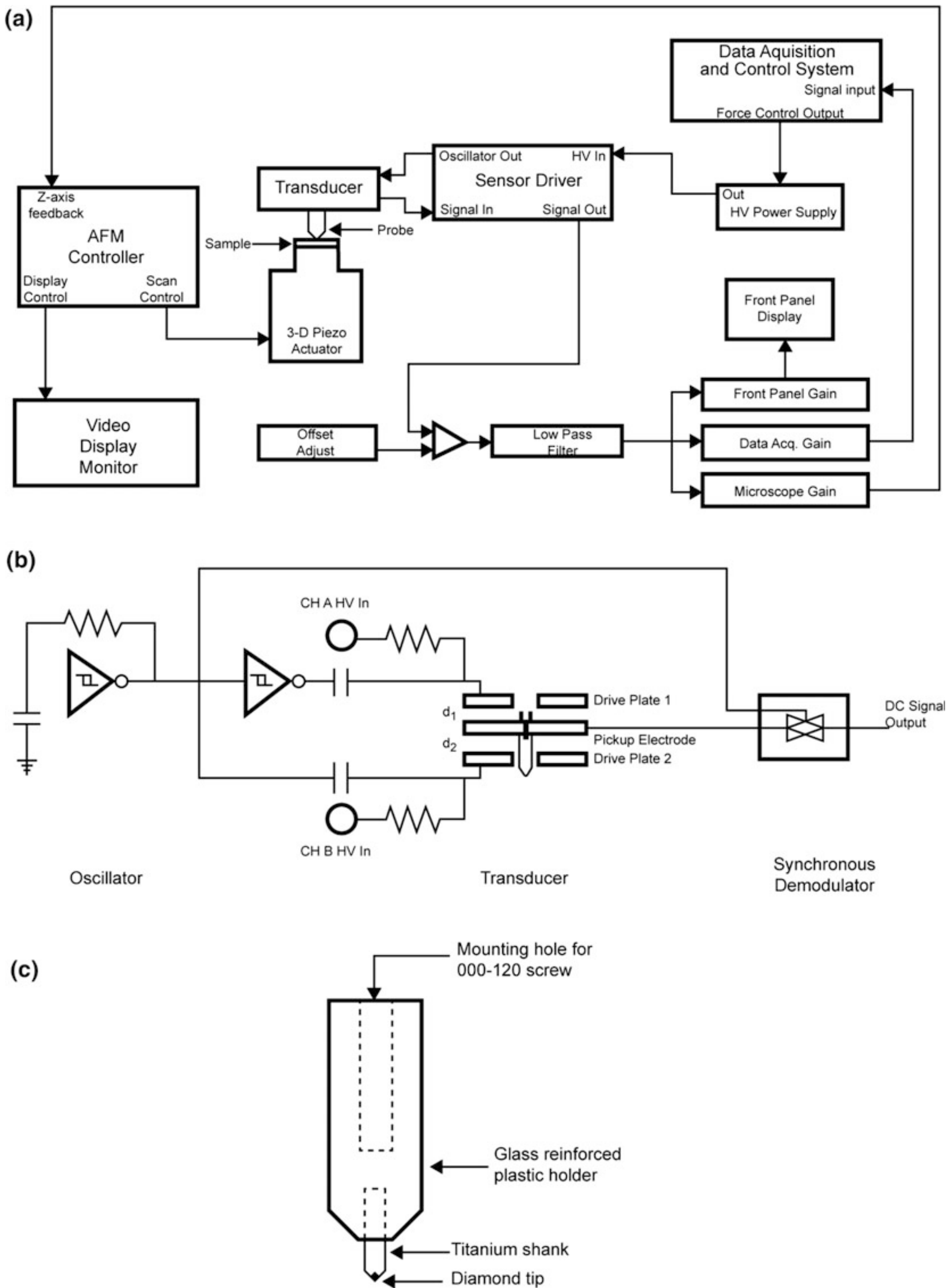

Fig. 5.3 Schematic of the Hysitron nanoindenter system **a** showing the major components, **b** the three-plate transducer with electrostatic actuation hardware and capacitance sensor, and **c** tip-holder mount assembly (adapted from Bhushan et al. 1996a)

is capable of making a well-defined indentation impression. The first four requirements are satisfied by choosing natural diamond material for the tip. A well-defined perfect tip shape is difficult to achieve. Berkovich is a three-sided pyramid and provides a sharply pointed tip compared with the Vickers or Knoop indenters, which are four-sided pyramids and have a slight offset (0.5–1 μm) (Tabor 1970; Bhushan 1999a; Bhushan and Li 2003). Because any three nonparallel planes intersect at a single point, it is relatively easy to grind a sharp tip on an indenter if Berkovich geometry is used. However, an indenter with a sharp tip suffers from a finite, but an exceptionally difficult-to-measure, tip bluntness. In addition, pointed indenters produce a virtually-constant plastic strain impression, and there is the additional problem of assessing the elastic modulus from the continuously-varying unloading slope. Spherical indentation overcomes many of the problems associated with pointed indenters. With a spherical indenter, one is able to follow the transition from elastic to plastic behavior and thereby define the yield stress (Bell et al. 1992). However, a sharper tip is desirable, especially for extremely thin films requiring shallow indentation. Therefore, a Berkovich indenter is used most commonly for measurements of nanomechanical properties. Experimental procedures have been developed to correct for the tip shape, to be described later.

The Berkovich indenter, directly brazed to a 304 stainless steel holder, is a three-sided (triangular-based) pyramidal diamond, with a nominal angle of 65.3° between the (side) face and the normal to the base at apex, an angle of 76.9° between edge and normal, and with a radius of the tip less than 0.1 μm (Fig. 5.4) (Berkovich 1951). The typical indenter is shaped to be used for a minimum indentation (penetration) depth of 10–20 nm. The indentations appear as equilateral triangles (Fig. 5.4c) and the height of triangular indent ℓ is related to the depth h as

$$\frac{h}{\ell} = \left(\frac{1}{2}\right) \cot 76.9 = \frac{1}{8.59} \tag{5.1a}$$

The relationship $h(\ell)$ is dependent on the shape of the indenter. The height of the triangular indent, ℓ, is related to the length of one side of the triangle, a, as

$$\ell = 0.866 \text{ a} \tag{5.1b}$$

and

$$\frac{h}{a} = \frac{1}{7.407} \tag{5.1c}$$

The projected contact area (A) for the assumed geometry is given as

$$A = 0.433a^2 = 23.76h^2 \tag{5.2}$$

Another three-sided pyramidal indenter, the cube corner indenter, can displace more than three times the volume of the Berkovich indenter at the same load, thereby producing much higher stresses and strains in the vicinity of the contact and reducing the cracking threshold. This makes this indenter ideal for the estimation of indentation fracture toughness at relatively small scales indentation (Li et al. 1997). The spherical indenter initiates elastic contact and then causes elastic-plastic contact at higher loads. This indenter is well-suited for examinations of yielding and work hardening. However, it is very difficult to obtain a precise sphere with a diameter of less than 100 μm made of diamond. This fact limits its application in nanoindentation testing.

The exact shape of the indenter tip needs to be measured for determination of hardness and elastic modulus. Since the indenter is quite blunt, direct imaging of indentations of small size in the SEM is difficult. Determination of tip area function will be discussed later.

5.2.1.3 Indentation Procedure

The hardness and elastic modulus are measured in compliance with ISO 14577. An indentation test involves moving the indenter to the surface of the material and measuring the forces and displacements associated during indentation. The surface is located for each indentation by

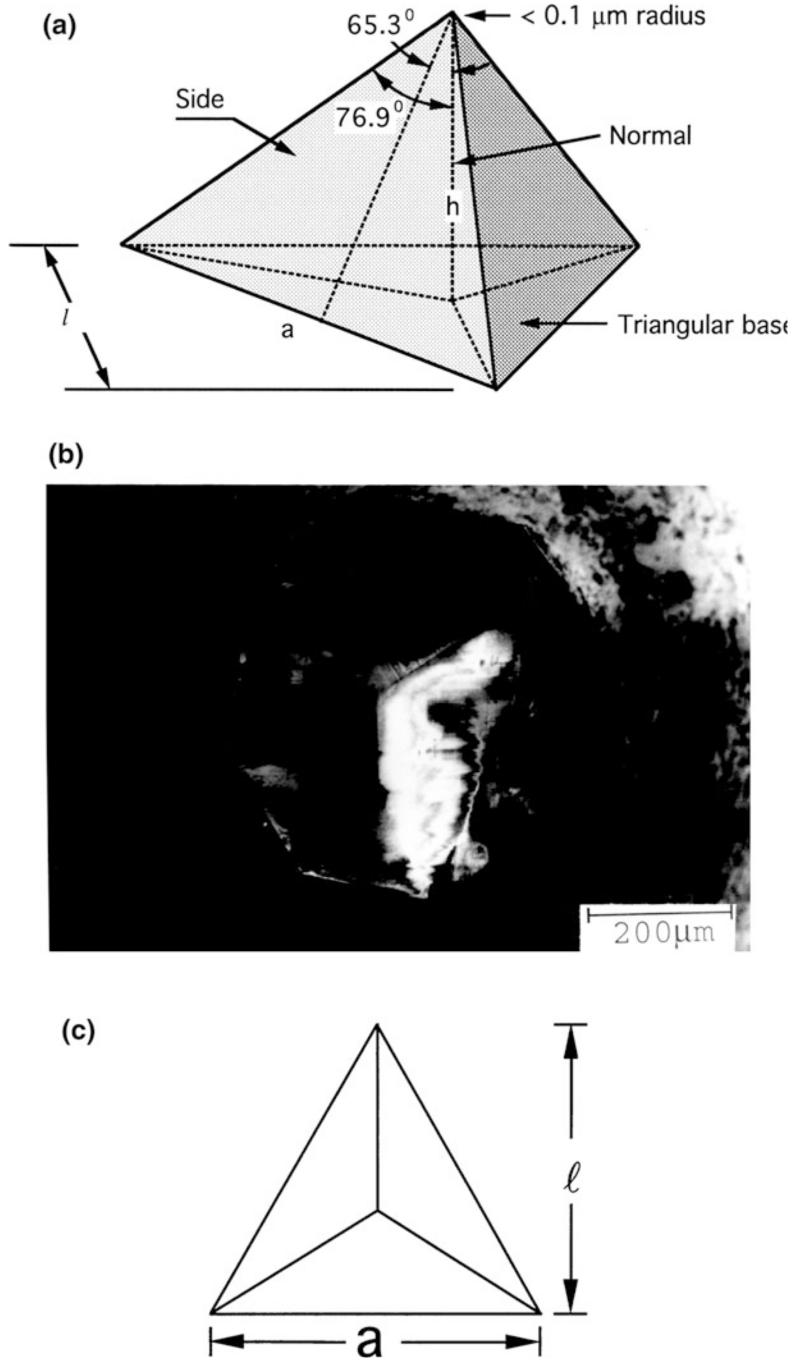

Fig. 5.4 **a** Schematic and **b** photograph of the shape of a Berkovich indenter, and **c** indent impression

lowering the indenter at a constant loading rate against the suspending springs and detecting a change in velocity on contact with the surface. In the testing mode, the load is incremented in order to maintain a constant loading rate or constant displacement rate. The load and indentation depths are measured during indentation both in the loading and unloading cycles. The force contribution of the suspending springs and the displacements associated with the measured

compliance of the instrument are removed (Bhushan 1999a; Bhushan and Li 2003).

Typically, a Berkovich tip with a radius of about 50 nm is used. Multiple loading and unloading steps are performed to examine the reversibility of the deformation, ensuring that the unloading data used for analysis purposes are mostly elastic. A typical indentation experiment consists of a combination of several segments, e.g., approach, load, hold, and unload. Either constant loading or constant displacement experiments can be performed (Oliver and Pharr 1992; Bhushan 1999a). A typical constant loading indentation experiment consists of eight steps: approaching the surface at 10 nm/s; loading to peak load at a constant loading rate (10% of peak load/s); unloading 90% of peak load at a constant unloading rate (10% of peak load/s); reloading to peak load; holding the indenter at peak load for 10 s; unloading 90% of peak load, holding the indenter after 90% unloading; finally unloading completely. The first hold step is included to incorporate the corrections due to thermal drift. Figure 5.5 shows a representative load-displacement curve of an indentation made at 15 mN peak indentation load for Si(100) during a loading/unloading sequence in a constant loading experiment (Bhushan and Li 2003).

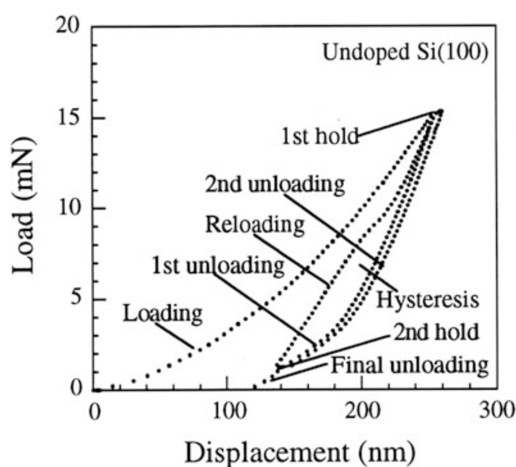

Fig. 5.5 Representative load-displacement curve during a loading/unloading sequence in a constant loading experiment (adapted from Bhushan and Li 2003)

5.2.1.4 Acoustic Emission Measurements During Indentation

Acoustic emission (AE) measurement is a very sensitive technique to monitor cracking of the surfaces and subsurfaces (Bhushan 1999a; Bhushan and Li 2003). The nucleation and growth of cracks result in a sudden release of energy within a solid, then some of the energy is dissipated in the form of elastic waves. These waves are generated by sudden changes in stress and displacement that accompany the deformation. If the release of energy is sufficiently large and rapid, then elastic waves in the ultrasonic frequency regime (AE) will be generated, and these can be detected using PZTs via expansion and compression of the PZT crystals (Scruby 1987; Bhushan 1996).

An AE sensor is used to detect cracking during indentation tests in the nanoindenter. It can be mounted underneath the sample. The energy dissipated during crack growth can be estimated by the rise time of the AE signal. The transducer converts the AE signal into voltage and is used for continuous display of the AE signal. Any correlation between the AE signal and local changes the load-displacement curves can be observed (Bhushan 1999a; Bhushan and Li 2003).

5.2.1.5 Nanoscratch and Lateral Force Measurements

There are several commercially available micro- and nanoscratch testers, such as the Taber shear/scratch tester (Taber Industries, North Tonawanda, New York) for thick films; Revetest Xpress scratch tester (CSM Instruments, Neuchatel, Switzerland) for thin films (Perry 1981, 1983; Sekler et al. 1988), and nanoindenter with scratch and lateral force measurement (LFM) options for ultrathin films (Wu 1991; Bhushan et al. 1995; Bhushan and Gupta 1995; Gupta and Bhushan 1995a, b; Bhushan 1999a; Bhushan and Li 2003). AFMs with a sharp diamond tip also are used for nanoscratch, nanowear, and lateral force measurements (Bhushan 1999b; Sundararajan and Bhushan 2001).

Here, the nanoscratch and LFM option in a commercial Keysight nanoindenter is described.

Scratches of various lengths at programmable loads can be made (Bhushan 1999a; Bhushan and Li 2003). Lateral (friction) forces and/or AE signal can also be measured simultaneously. The lateral force option includes a set of proximity (capacitance) probes for measurement of lateral displacement or force in the two lateral directions along X and Y, and a special "scratch collar," which mounts around the indenter shaft with hardness indenter, Fig. 5.2b. A scratch block is mounted on the end of the indenter shaft, in line with the proximity probes and the positioning screws. The scratch tip is attached to the scratch block with two Allen head screws. The scratch tip can be a Berkovich indenter or a conventional conical diamond tip with a tip radius of about 1–5 µm and an included angle of 60°–90° (typically 1 µm of tip radius with 60° of included angle; Bhushan et al. 1995; Palacio and Bhushan 2010; Kumar and Bhushan 2015; Cho and Bhushan 2016). A larger included angle of 90° may be desirable for a more durable tip. The tip radius should not be very small as it will blunt readily.

During scratching, a load is applied up to a specified indentation load or up to a specified indentation depth, and the lateral motion of the sample is measured. During scratching, load and indentation depth are monitored. Scratches can be made either with a constant load or at ramp-up load. Measurement of lateral force allows the calculations of the coefficient of friction during scratching. The resolution of the proximity probe provides resolution of lateral force on the order of 2 µN; therefore, a minimum load of about 20 µN can be measured. Consequently, a minimum normal load of about 0.2 mN typically is used for a sample with a coefficient of friction of about 0.1. Microscopy of the scratch produced at ramp-up load allows measurement of the critical load required to break the film (if any), scratch width, and general observations of scratch morphology. Typically, draw acceleration (µm/s^2) and draw velocity (µm/s) are 10 µm/s^2 and 5 µm/s, respectively. The data not only provide measures of scratch resistance or wear resistance, but also provide insight into ductile/brittle fracture modes (Bhushan and Gupta 1995).

5.2.2 Analysis of Indentation Data

Load, W, as a function of displacement (or indentation depth or penetration depth), h, is monitored continuously and recorded during the loading and unloading process, and is referred to as an indentation curve or load-displacement curve (Bhushan 1999a; Bhushan and Li 2003). Figure 5.6 shows stress-strain curves, typical indentation curves, the deformed surfaces after tip removal, and residual impressions of indentation for ideal elastic, rigid-perfectly plastic, elastic-perfectly plastic, and real elastic-plastic solids (Bhushan 1999a). For an elastic solid, the sample deforms elastically according to elastic modulus, and the deformation is recovered during unloading. As a result, there is no impression of the indentation after unloading. For a rigid-perfectly plastic solid, no deformation occurs until yield stress is reached, when plastic flow takes place. There is no recovery during unloading and the impression remains unchanged. In the case of elastic-plastic solid, it deforms elastically according to elastic modulus and then it deforms plastically. The elastic deformation is recovered during unloading. In the case of an elastic-perfectly plastic solid, there is no work hardening.

Most engineering surfaces follow real elastic-plastic deformation behavior with work hardening (Johnson 1985; Bhushan 2013a, b). Figure 5.7a schematically shows the deformation pattern of a real elastic-plastic sample during and after indentation (Oliver and Pharr 1992; Hainsworth et al. 1996; Oliver 2001). The contact depth (h_c) is defined as the depth of indenter in contact with the sample under load. The depth measured during the indentation (h) includes the depression of the sample around the indentation, in addition to the contact depth. The depression of the sample around the indentation ($h_s = h - h_c$) is caused by elastic displacements and must be subtracted from the data to obtain the actual depth of indentation or actual hardness. At peak load, the load and displacement are W_{max} and h_{max}, respectively, and the radius of the contact circle is a. Upon unloading, the elastic displacements in the contact region are recovered

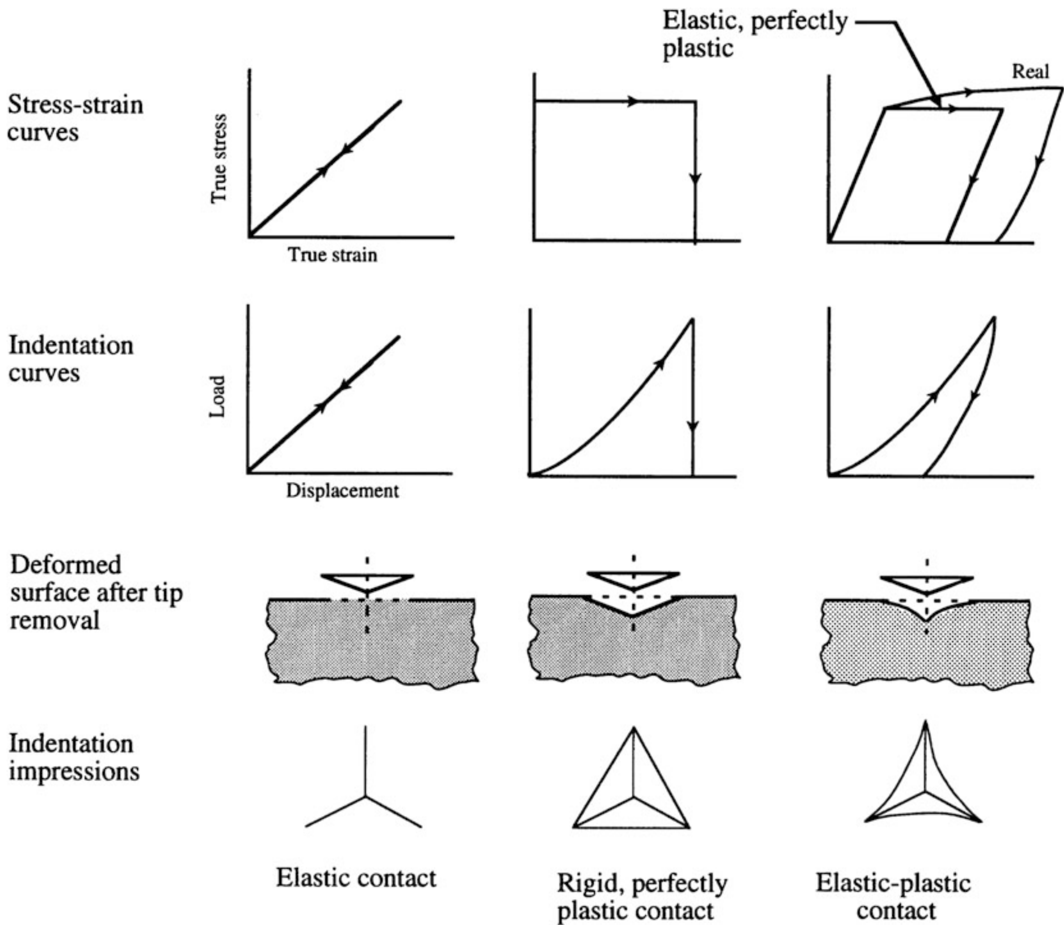

Fig. 5.6 Schematics of stress-strain curves, typical indentation curves, deformed surfaces after tip removal, and residual impressions of indentation, for ideal elastic, rigid-perfectly plastic, elastic-perfectly plastic (ideal) and real elastic-plastic solids

and when the indenter is fully withdrawn, the final depth of the residual hardness impression is h_f. A schematic of a load-displacement curve is shown in Fig. 5.7b.

In order to predict the deflection of the surface at the contact perimeter for a conical indenter and a paraboloid of revolution, Oliver and Pharr (1992) developed an expression, based on the work of Sneddon (1965), for h_c at the maximum load (required for hardness calculation) from h_{max},

$$h_c = h_{max} - \varepsilon W_{max}/S_{max} \tag{5.3a}$$

where ε = 0.72 for the conical indenter, ε = 0.75 for the paraboloid of revolution, and ε = 1 for the flat punch; and S_{max} is the stiffness (=1/compliance) equal to the slope of unloading curve (dW/dh) at the maximum load. (Hay et al. (1999) have proposed corrections to Sneddon's equations.) Oliver and Pharr (1992) assumed that behavior of the Berkovich indenter is similar to that of the conical indenter, since cross-sectional areas of both types of indenters varies as the square of the contact depth and their geometries are singular at the tip. Therefore, for a Berkovich indenter, ε ∼ 0.72. Thus, h_c is slightly larger than plastic indentation depth (h_p), which is given by

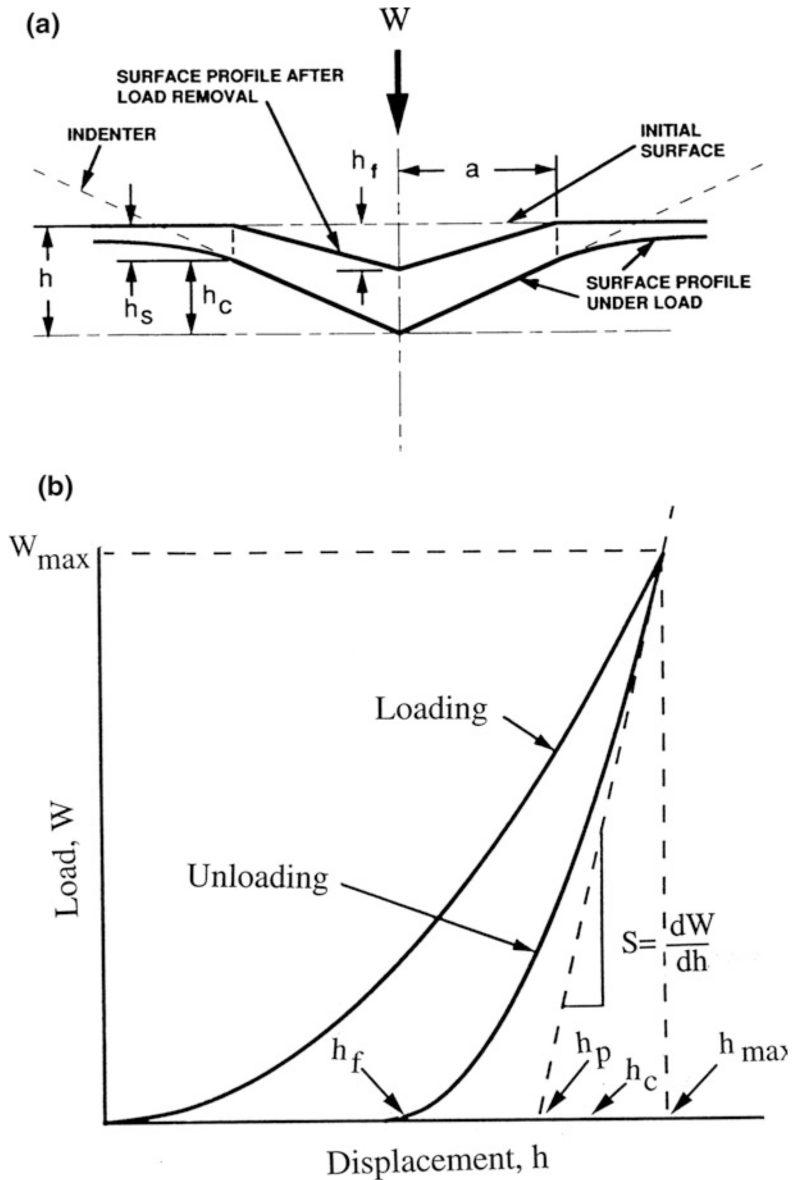

Fig. 5.7 **a** Schematic representation of the indenting process illustrating the depression of the sample around the indentation and the decrease in indentation depth upon unloading (adapted from Oliver and Pharr 1992), and **b** schematic of load-displacement curve

$$h_p = h_{max} - W_{max}/S_{max} \tag{5.3b}$$

Based on the finite element analysis of the indentation process, Laursen and Simo (1992) showed that h_c cannot be assumed equal to h_p for indenters that do not have a flat-punch geometry.

Projected contact-area-to-depth relationship for a Vickers indenter with ideal pyramidal geometry (ideally sharp tip) is given as (Doerner and Nix 1986; Bhushan 1999a; Swadener et al. 2002)

$$A = 24.5h_c^2 \tag{5.4a}$$

Since the area to depth relationship is equivalent for both typical Berkovich and Vickers pyramids, Eq. 5.4a holds for the Berkovich indenter as well. Although a slightly different

expression for A(h) is presented in Eq. 5.2 for the assumed Berkovich indenter geometry, this relationship is used most commonly in the analysis of the indentation hardness data.

As shown in Fig. 5.8a, the indenter tip generally is rounded so that ideal geometry is not maintained near the tip. To study the effect of tip radius on the elastic-plastic deformation (load vs. displacement curve), Shih et al. (1991) modeled the blunt-tip geometry by a spherical tip of various radii. They derived a geometric relationship (assuming no elastic recovery) between the projected contact area of the indenter to the actual contact depth. Figure 5.8b shows the measured contact area vs. indentation depth data by Pethica et al. (1983) for nickel and by Doerner and Nix (1986) for annealed α-brass. From this figure, it seems that a tip radius of 1 μm fits the data best. If there is elastic recovery, the experimental data are smaller than what they should be, and then the tip radius would be even larger than 1 μm. Shih et al. (1991) used the finite element method to simulate an indentation test. They showed that load-indentation depth data obtained using nanoindenter for nickel by Pethica et al. (1983) can be fitted with a simulated profile for a tip radius of about 1 μm, Fig. 5.8c.

Figure 5.8 shows that the actual indentation depth, h_c, produces a larger contact area than would be expected for an indenter with an ideal shape. For the real indenter used in the measurements, the nominal shape is characterized by an area function $F(h_c)$, which relates projected contact area of the indenter to the contact depth (Eq. 5.4a),

$$A^{1/2} = F(h_c) \tag{5.4b}$$

The functional form must be established experimentally prior to the analysis (to be described later).

5.2.2.1 Hardness

Berkovich hardness HB (or H_B) is defined as the load divided by the projected contact area of the indentation. It is the mean pressure that a material will support under load. From the indentation curve, we can obtain hardness at the maximum load as

$$HB = W_{max}/A \tag{5.5}$$

where W_{max} is the maximum indentation load, and A is the projected contact area at the peak load. The contact area at the peak load is determined by the geometry of the indenter and the corresponding contact depth h_c using Eqs. 5.3a and 5.4b. A plot of hardness as a function of indentation depth for polished single-crystal Si (111), with and without tip-shape calibration, is shown in Fig. 5.9. We note that, for this example, tip-shape calibration is necessary. For these measurements, the hardness is independent of corrected depth.

Note that hardness measured using this definition may be different from that obtained from the more conventional definition in which the area is determined by direct measurement of the size of the residual hardness impression. The reason for the difference is that, in some materials, a small portion of the contact area under load is not plastically deformed, and, as a result, the contact area measured by observation of the residual hardness impression may be less than that at peak load. However, for most materials, measurements using two techniques give similar results.

5.2.2.2 Modulus of Elasticity

The initial unloading is an elastic event, though during loading a sample undergoes elastic-plastic deformation. Therefore, elastic modulus of the specimen can be inferred from the initial slope of the unloading curve (*dW/dh*) called stiffness (1/compliance) (at the maximum load) (Fig. 5.7 b). It should be noted that the contact stiffness is measured only at the maximum load, and no restrictions are placed on the unloading data being linear during any portion of the unloading (Bhushan 1999a; Bhushan and Li 2003).

An approximate elastic solution is obtained by analyzing a flat punch whose area in contact with the specimen is equal to the projected area of the actual punch, assuming that the area in contact remains constant during initial unloading. Based on the analysis of indentation of an elastic half space by a flat cylindrical punch by Sneddon

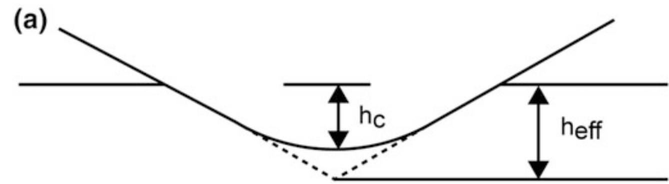

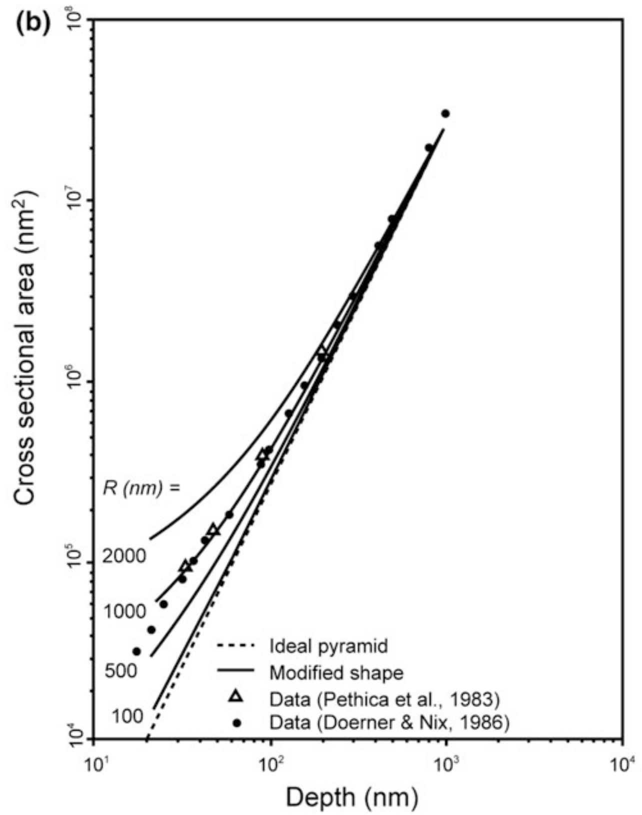

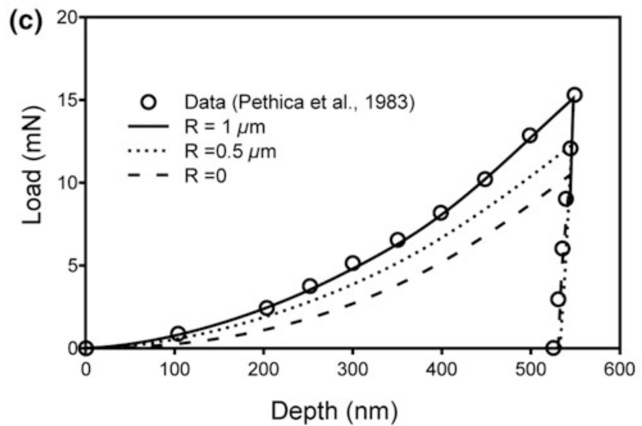

Fig. 5.8 **a** Schematic of an indenter tip with a nonideal shape. The contact depth and the effective depth are also shown, **b** predicted projected contact area as a function of indentation depth curves for various tip radii and measured data for nickel (adapted from Pethica et al. 1983), and for annealed α-brass (adapted from Doerner and Nix 1986), and **c** predicted load as a function of indentation depth curves for various tip radii and measured data for nickel (adapted from Shih et al. 1991)

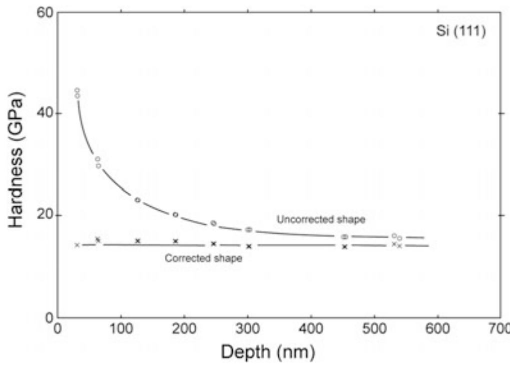

Fig. 5.9 Hardness as a function of indentation depth for polished single-crystal Si(111) calculated from the area function with and without tip shape calibration (adapted from Doerner and Nix 1986)

(1965), Loubet et al. (1984) calculated the elastic deformation of an isotropic elastic material with a flat-ended cylindrical punch. They obtained an approximate relationship for compliance (*dh/dW*) for the Vickers (square) indenter. King (1987) solved the problem of flat-ended cylindrical, quadrilateral (Vickers and Knoop), and triangular (Berkovich) punches indenting an elastic half-space. He found that the compliance for the indenter is approximately *independent of the shape* (with a variation of at most 3%) if the projected area is fixed. Pharr et al. (1992) also verified that compliance of a paraboloid of revolution of a smooth function is the same as that of a spherical or a flat-ended cylindrical punch. The relationship for the compliance C (inverse of stiffness S) for an (Vickers, Knoop, and Berkovich) indenter is given as

$$C = \frac{1}{S} = \frac{dh}{dW} \sim \frac{1}{2E_r}\left(\frac{\pi}{A}\right)^{1/2} \quad (5.6)$$

where

$$\frac{1}{E_r} = \frac{1 - \nu_s^2}{E_s} + \frac{1 - \nu_i^2}{E_i}$$

dW/dh is the slope of the unloading curve at the maximum load (Fig. 5.7b), E_r, E_s, and E_i are the reduced modulus and elastic moduli of the specimen and the indenter, and ν_s and ν_i are the Poisson's ratios of the specimen and indenter. C (or S) is the experimentally measured compliance (or stiffness) at the maximum load during unloading, and A is the projected contact area at the maximum load.

The contact depth h_c is related to the projected area of the indentation A for a real indenter by Eq. 5.4b. With a plot of the measured compliance (*dh/dW*) the reciprocal of the corrected indentation depth obtained from various indentation curves (one data point at maximum load for each curve) should yield a straight line with slope proportional to $1/E_r$ (Fig. 5.10) (Doerner and Nix 1986). E_s can then be calculated, provided Poisson's ratio with great precision is known to obtain a good value of the modulus. For a diamond indenter, $E_i =$ 1140 GPa and $\nu_i = 0.07$ are taken (Bhushan 1999a; Bhushan and Li 2003). In addition, the y-intercept of the compliance vs. the reciprocal indentation depth plot should give any additional compliance that is independent of the contact area. The compliance of the loading column is generally removed from the load-displacement curve, whose measurement techniques will be described later.

To measure initial unloading stiffness (S), Doerner and Nix (1986) fitted a straight line to the

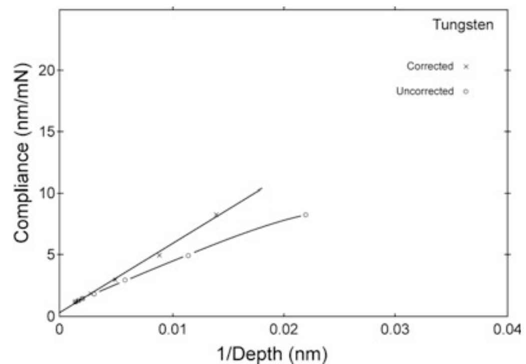

Fig. 5.10 Compliance as a function of the inverse of indentation depth for tungsten with and without tip shape calibration. A constant modulus with 1/depth would be indicated by the straight line. The slope of the corrected curve is 480 GPa, which compares reasonably well to the known modulus of tungsten (420 GPa). The small y-intercept of about 0.3 nm/mN is attributed to load frame compliance, not removed (adapted from Doerner and Nix 1986)

upper about one third portion of the unloading curve. The problem with this is that for nonlinear loading data, the measured stiffness depends on how much of the data is used in the fit. Oliver and Pharr (1992) proposed a new procedure. They found that the entire unloading data are well described by a simple power law relation

$$W = B\left(h - h_f\right)^m \tag{5.7}$$

where the constants B and m are determined by a least-square fit. The initial unloading slope is then found analytically, differentiating this expression and evaluating the derivative at the maximum load and maximum depth. As we have pointed out earlier, unloading data used for the calculations should be obtained after several loading/unloading cycles and with peak hold periods.

This analysis is based on an elastic solution, which only accounts for sink-in (the indented material around the indenter below its original surface). However, in the more realistic case of elastic-plastic contact, sink-in or pile-up (the indented material around the indenter above its original surface) can occur depending on the specific mechanical properties of the material. For pile-up situations, the just-described Oliver-Pharr method would underestimate the true contact area by as much as 50%. This in turn leads to overestimation of the hardness and elastic modulus. Based on some modeling, pile-up is significant only when $h_f/h_{max} > 0.7$ and the material does not appreciably work harden. Note that h_f/h_{max} equal to zero corresponds to fully elastic deformation and a value of 1 corresponds to rigid-plastic behavior. Compressive residual stresses result in pile-up, whereas tensile stresses result in sink-in. Although some correction procedures have been proposed (Pharr 1998; Tsui and Pharr 1999), the real contact area measurement requires imaging of indentation impressions.

5.2.2.3 Determination of Load Frame Compliance and Indenter Area Function

As stated earlier, measured displacements are the sum of the indentation depths in the specimen and the displacements of suspending springs and the displacements associated with the measuring instruments, referred to as load frame compliance. Therefore, to determine accurately the specimen depth, load frame compliance must be known (Bhushan 1999a; Bhushan and Li 2003). This is especially important for large indentations made with high modulus for which the load frame displacement can be a significant fraction of the total displacement. The exact shape of the diamond indenter tip needs to be measured because hardness and elastic modulus depend on the contact areas derived from measured depths. The tip gets blunt (Fig. 5.8a) and its shape significantly affects the prediction of mechanical properties (Figs. 5.9 and 5.10).

Oliver and Pharr (1992) proposed a method for determining area functions. Their method is based only on one assumption: that elastic modulus is independent of indentation depth. They also proposed a method to determine load frame compliance. We first describe the methods for determining of load frame compliance followed by the method for area function.

They modeled the load frame and the specimen as two springs in series; thus,

$$C = C_s + C_f \tag{5.8}$$

where C, C_s, and C_f are the total measured compliance, specimen compliance and load frame compliance, respectively. From Eqs. 5.6 and 5.8, we get

$$C = C_f + \frac{1}{2E_r}\left(\frac{\pi}{A}\right)^{1/2} \tag{5.9}$$

From Eq. 5.9, we note that if the modulus of elasticity is constant, a plot of C as a function of $A^{-1/2}$ is linear and the vertical intercept gives C_f. It is obvious that the most accurate values of C_f are obtained when the specimen compliance is small; i.e., for large indentations.

To determine the area function and the load frame compliance, relatively large indentations in aluminum are made because of its low hardness (Bhushan 1999a; Bhushan and Li 2003). In addition, for the larger aluminum indentations (typically 700–4000 nm deep), the area function

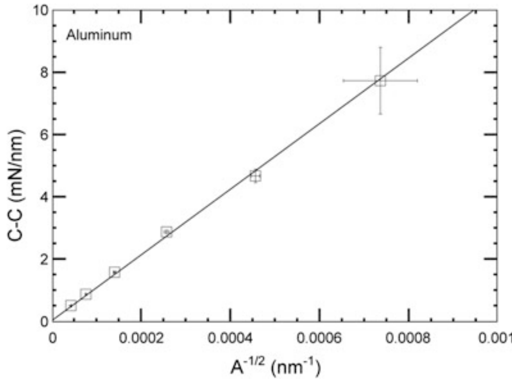

Fig. 5.11 Plot of (C-C_f) as a function $A^{-1/2}$ for aluminum. The error bars are two standard deviations in length (adapted from Oliver and Pharr 1992)

for a perfect Berkovich indenter (Eq. 5.4a) can be used to provide a first estimate of the contact. Values of C_f and E_r are thus obtained by plotting C as a function of $A^{-1/2}$ for the large indentations, Fig. 5.11.

Contact areas for indentations are made using the measured C_f value at shallow depths on the aluminum with measured E_r and/or on a harder fused silica surface with published values of E_r, by rewriting Eq. 5.9 as

$$A = \frac{\pi}{4}\frac{1}{E_r^2}\frac{1}{\left(C - C_f\right)^2} \tag{5.10}$$

from which an initial guess at the area function is made by fitting A as a function h_c data to an eighth-order polynomial

$$A = 24.5h_c^2 + C_1h_c + C_2h_c^{1/2} + C_3h_c^{1/4} + \cdots + C_8h_c^{1/128} \tag{5.11}$$

where C_1 through C_8 are constants. The first term describes the perfect shape of the indenter; the others describe deviations from the Berkovich geometry due to blunting of the tip. A convenient fitting routine is that contained in the Kaleidagraph software. A weighted procedure can be used to assure that data points with small and large magnitudes are of equal importance. An iterative approach can be used to refine the values of C_f and E_r further.

For calculations of load frame compliance and indenter area function, a series of indents are made in two standard materials—aluminum and fused quartz. It is assumed that both these materials are elastically isotropic, their moduli are well known, and their moduli are independent of indentation depth (Oliver and Pharr 1992). The first step is to determine the load frame compliance precisely by indenting a well-annealed, high-purity aluminum, typically at indentation depths from 700 to 4000 nm. As an example, the following load time history can be used. (1) Approach and contact surface, (2) load to peak load, (3) unload to 90% of peak load and hold for 100 s, (4) reload to peak load and hold for 10 s, and (5) unload completely. The lower hold is used to establish thermal drift and the upper hold to minimize time-dependent plastic effects. The final unloading data are used to determine the unloading compliances using the power law fitting procedure described earlier. The load frame compliance is determined from the aluminum data by plotting the measured compliance as a function of area calculated, assuming the ideal Berkovich indenter. Calculated E_r is checked with known elastic constants for aluminum, E = 70.4 GPa and ν = 0.347.

The problem with using aluminum to extend the area function to small depths is that because of its low hardness, small indentations in aluminum require very small loads, and a limit is set by the force resolution of the indentation system (Bhushan 1999a; Bhushan and Li 2003). This problem can be avoided by making the small indentations in fused quartz, a much harder, isotropic material available in optically-finished plate form. Typically, measurements are made at six or so peak loads at depths ranging from about 15 to 700 nm. Above 700 nm of depth, indenter can be assumed to have a perfect shape. The contact areas and contact depths are then determined using Eq. 5.11 and h_c in conjunction with the reduced modulus computed from the elastic constant for fused quartz, E = 72 GPa and ν = 0.170. The machine compliance is known from the aluminum analysis. The area function is only good for the depth range used in the

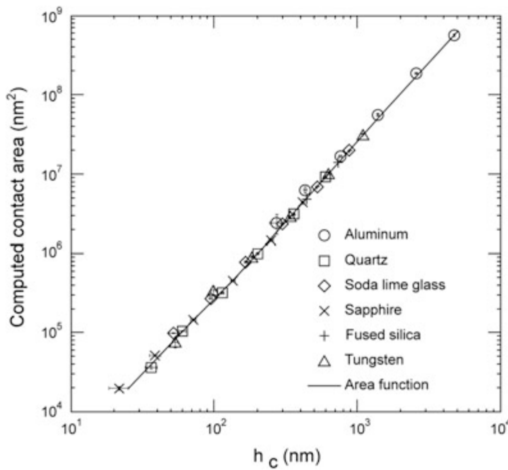

Fig. 5.12 The computed contact areas as a function of contact depths for six materials. The error bars are two standard deviations in length (adapted from Oliver and Pharr 1992)

calculations. Typical data of contact areas as a function of contact depths for six materials is shown in Fig. 5.12.

In situ scanning electron microscope (SEM) and transmission electron microscope (TEM) indentation tests are expected to give an in-depth understanding of elastic/plastic deformation behavior. Some nanoindenter instruments can be operated inside an SEM or TEM.

5.2.2.4 Hardness/Modulus^2 Parameter

Calculations of hardness and modulus described so far require the calculations of the indent's projected contact area from the indentation depth, which are based on the assumption that the test surface be smooth to dimensions much smaller than the projected area (Bhushan 1999a; Bhushan and Li 2003). Therefore, data obtained from rough samples show considerable scatter. Joslin and Oliver (1990) developed an alternative method for data analysis without requiring the calculations of the projected contact area of the indent. This method provides measurement of a parameter hardness/modulus^2, which provides a measure of the resistance of the material to plastic penetration.

Joslin and Oliver (1990) showed that for several types of rigid punches (cone, flat punch, parabola of revolution, and sphere) as long as there is a single contact between the indenter and the specimen,

$$H/E_r^2 = (4/\pi)\left(W/S^2\right) \tag{5.12}$$

where S is the stiffness obtained from the unloading curve. E_r is related to E_s by a factor of $1 - \nu_S^2$ for materials with moduli significantly less than diamond (Eq. 5.6). The H/E_S^2 parameter represents a materials resistance to plastic penetration. We clearly see that calculation of projected contact area and knowledge of area function are not required. However, this method does not give the hardness and modulus values separately.

5.2.2.5 Continuous Stiffness Measurement (CSM)

The continuous stiffness measurement technique allows measurement of sample stiffness during indentation without the need for discrete unloading cycles, and with a time constant that is at least three orders of magnitude smaller than the time constant of the more conventional method of determining stiffness from the slope of an unloading curve (Pethica and Oliver 1989; Li and Bhushan 2002a). Furthermore, the measurements can be made at exceedingly small penetration depths. Thus, this method is ideal for determining the stiffness and, hence, the elastic modulus and hardness of films a few tens of nanometers thick. Furthermore, its small time constant makes it especially useful in measuring the properties of some polymeric materials.

Measurement of continuous stiffness is accomplished by the superposition of a very small AC current of a known relatively high frequency (typically 69.3 Hz) on the loading coil of the indenter, Fig. 5.13. This current, which is much smaller than the DC current that determines the nominal load on the indenter, causes the indenter to vibrate with a frequency related to the stiffness of the sample and to the indenter contact area. A comparison of the phase and amplitude of the indenter vibrations (determined with a lock-in amplifier) with the phase and amplitude of the imposed AC signal allows the stiffness to be calculated either in terms of amplitude or phase.

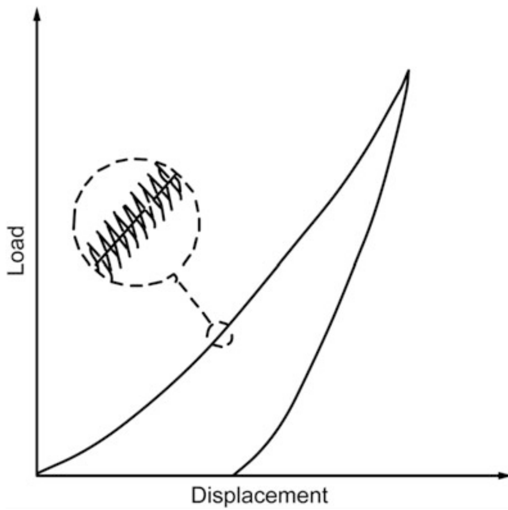

Fig. 5.13 Schematic of loading cycle in the continuous stiffness option

For calculation of stiffness, the dynamic response of the indentation system has to be determined (Li and Bhushan 2002a; Bhushan and Li 2003). The relevant components are the mass m of the indenter, the spring constant K_f of the leaf springs that support the indenter (load frame stiffness), the stiffness of the indenter frame K_s, and the damping constant C_i due to the air in the gaps of the capacitor plate displacement-sensing system. These combine with the sample stiffness, S, and damping constant of the contact zone, C_s, as shown schematically in Fig. 5.14 to produce the overall response. If the imposed driving force is $F(t) = F_0 \exp(i\omega t)$ and the displacement response of the indenter is $z(t) = z_0 \exp(i\omega t - \phi)$, the ratio of amplitudes of the imposed force and the displacement response is given by (Pethica and Oliver 1989)

$$\left|\frac{F_0}{z_0}\right| = \left[\left(K - m\omega^2\right)^2 + \omega^2 C^2\right]^{1/2} \tag{5.13}$$

and the phase angle, ϕ, between the driving force and the response is

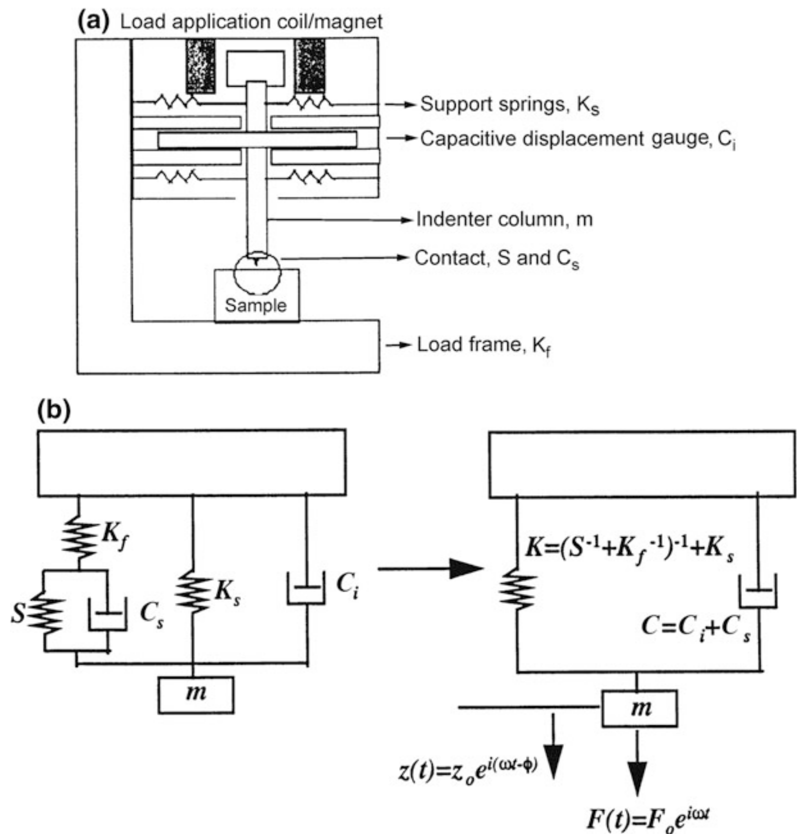

Fig. 5.14 **a** Schematic of a nanoindenter with each component represented in the simple harmonic oscillator models, and **b** the dynamic model of the indentation system (adapted from Bhushan and Li 2003)

$$\tan \phi = \omega C / \left(K - m\omega^2\right) \qquad (5.14)$$

Equations 5.13 and 5.14 may be solved simultaneously for K and C. The stiffness and damping of the contact are given by

$$S = \left[\frac{1}{\frac{F_0}{z_0}\cos\phi - (K_s - m\omega^2)} - \frac{1}{K_f}\right]^{-1} \qquad (5.15a)$$

and

$$C_s\omega = \frac{F_0}{z_0}\sin\phi - C_i\omega \qquad (5.15b)$$

With the exception of S and C_s terms, all the terms in Eqs. 5.15a, 5.15b can be measured independently. The parameters m, K_s, and C_i are determined by analyzing the dynamic response of the system when the indenter is hanging free, which is done in the factory. Details on K_f have been presented earlier. In a CSM experiment, the excitation frequency (ω) is set. The AC input to the force coil is generated with a standard AC signal generator, and any frequency between about 10 and 150 Hz may be selected. The displacement amplitude (z_0) and phase angle (ϕ) (using a lock-in amplifier) are measured. Using Eqs. 5.15a, 5.15b, S and C_sω are calculated.

5.2.2.6 Bending Experiments by Beam Deflection Measurement

Bending and bending fatigue properties of suspended cantilevered and doubled anchored (fixed) beams can be measured using a nanoindenter or an AFM (Sundararajan et al. 2002; Li and Bhushan 2003; Li et al. 2003; Wei et al. 2005; Palacio et al. 2007a, b). The advantage of a nanoindenter is that loads up to about 400 mN higher than those in AFM (up to about 100 μN) can be used for some structures requiring high loads. Figure 5.15 shows a schematic of the beam bending in the normal and lateral direction using a nanoindenter (Palacio et al. 2007a, b). To avoid a sharp tip pushing into the beam specimen, a blunt tip is used.

For bending experiments, load as a function of displacement is measured, and the slope of the curve is obtained. For a cantilever beam with one end clamped, the elastic modulus E is given as (Young et al. 2012),

$$E = \frac{\ell^3}{3I} m \qquad (5.16a)$$

where ℓ is the beam length, I is the area moment of inertia for the beam cross-section, and m is the slope of the linear region of the force displacement curve. For a fixed elastic beam loaded at the center of the span in the normal direction, as shown in Fig. 5.15 (middle), the elastic modulus is expressed as (Young et al. 2012)

$$E = \frac{\ell^3}{192I} m \qquad (5.16b)$$

for a beam with a rectangular cross-section of width w and thickness t, $I = wt^3/12$.

The application of simple beam theory to the load deflection data of beams also enable one to determine the yield strength of the microbeam material. For a homogeneous cantilever beam under load at the end of the beam, the strain in the beam varies linearly through the thickness such that the maximum strain at a given length occurs at the top and at the bottom of the beam. The top of the beam is in tension and the bottom of the beam is in compression. In addition, the maximum stress in the beam is located at the fixed end of the beam where the applied moment is greatest. When this maximum stress reaches the yield strength of the material, the beam begins to deform plastically. The onset of such deformation can be recognized in the plot of load versus deflection by a deviation from linearity. The load that marks this deviation is defined as the yield load W_y, and the yield strength for a rectangular beam is given by (Young et al. 2012),

$$\sigma_y = 6W_y\ell / \left(bt^2\right) \qquad (5.17)$$

Following yielding, the beam continues to bend as more load is applied, and some of the strain in the beam is plastic. Thus, it is unrecoverable during unloading, and the beam eventually fails. The shape of the load versus

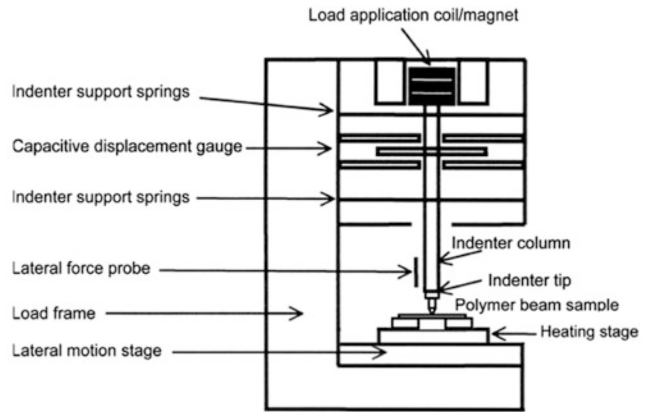

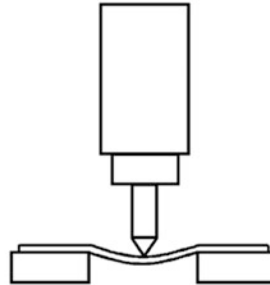

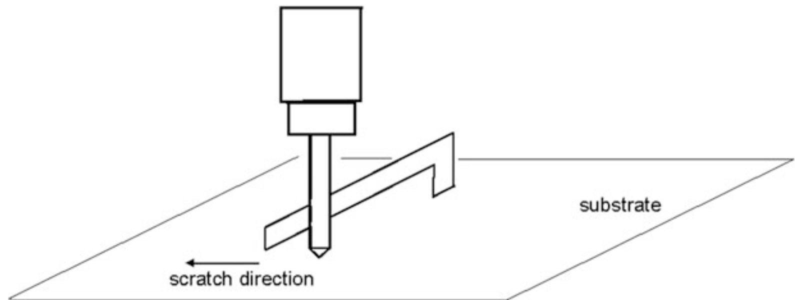

Fig. 5.15 Schematic of cantilever beam bending test in the normal and lateral direction using a nanoindenter (adapted from Palacio et al. 2007b)

deflection curves after yielding and prior to unloading depends on the elastic and plastic properties of the material.

5.2.2.7 Determination of Hardness and Modulus of Elasticity of Thin Films from the Composite Response of Film and Substrate

It is widely accepted that to measure true hardness of films, the indentation depth should not exceed 10% of the film thickness (Tabor 1951) to 30% of the film thickness (Anonymous 1979). Otherwise, measured hardness is affected by the substrate properties. A number of expressions have been derived that relate thin-film hardness to substrate hardness, composite hardness (measured on the coated substrate), and film thickness. These analyses allow the calculation of the thin-film hardness from the measured composite hardness data (Buckle 1973; Doerner and Nix 1986; Sargent 1986; Burnett and Rickerby 1987b; King 1987; Bhattacharya and Nix 1988a, b; Bull and Rickerby 1990; Vinci and Vlassak 1996; Korsunsky et al. 1998; McGurk and Page 1999; Tsui and Pharr 1999). Here we discuss two models based on the volume law of mixtures (volume fraction model) (Sargent 1986) and numberical analysis (King 1987; Bhattacharya and Nix 1988a, b; Bhushan and Venkatesan 2005; Bhushan 2013a, b).

The hardness of a film/substrate composite generally is believed to be a weighted average of the volume of plastically-deformed material in the film (V_f) and that in the substrate (V_s) (Sargent 1986),

$$H = H_f \frac{V_f}{V} + H_s \frac{V_s}{V} \tag{5.18}$$

where $V = V_f + V_s$. The deformed volumes of film and substrate can be calculated using expanding spherical cavity model (Johnson 1985).

Bhattacharya and Nix (1988a, b) modeled the indentation process using the finite-element method to study the elastic-plastic response of materials. Bhattacharya and Nix (1988b) calculated elastic and plastic deformation associated with submicron indentation by a conical indenter of thin films on substrates, using the finite-element method. The effects of the elastic and plastic properties of both the film and substrate on the hardness of the film/substrate composite were studied by determining the average pressure under the indenter as a function of the indentation depth. They developed empirical equations for film/substrate combinations for which the substrate is either harder or softer than the film. For the case of a soft film on a harder substrate, the effect of substrate on film hardness can be described as

$$\frac{H}{H_s} = 1 + \left(\frac{H_f}{H_s} - 1\right) exp\left[-\frac{(\sigma_f/\sigma_s)}{(E_f/E_s)}(h_c/t_f)^2\right] \tag{5.19a}$$

where E_f and E_s are the elastic moduli, σ_f and σ_s and are the yield strengths, and H_f and H_s are the hardnesses of the film and substrate, respectively. H is the hardness of the composite, h_c is the contact indentation depth, and t_f is the film thickness. Similarly, for the case of a hard film on a softer substrate, the hardness can be expressed as

$$\frac{H}{H_s} = 1 + \left(\frac{H_f}{H_s} - 1\right) exp\left[-\frac{(H_f/H_s)}{(\sigma_f/\sigma_s)(E_f/E_s)^{1/2}}(h_c/t_f)\right] \tag{5.19b}$$

Composite hardness results were found to depend only very weakly on Poisson's ratio (v). Figure 5.16 presents plots showing the effect of relative elastic moduli of the film and the substrate on the composite hardness as a function of the depth of indentation for a soft film on a hard substrate and a hard film on a soft substrate. For cases in which the film and substrate have different elastic moduli, hardness is observed to be independent of the substrate for indentation depths less than about 30% of the film thickness, after which the hardness slowly increases/decreases because of the presence of the substrate (also see Bhushan and Venkatesan 2005). Thus, the "30% rule" is preferred. They also reported that for cases

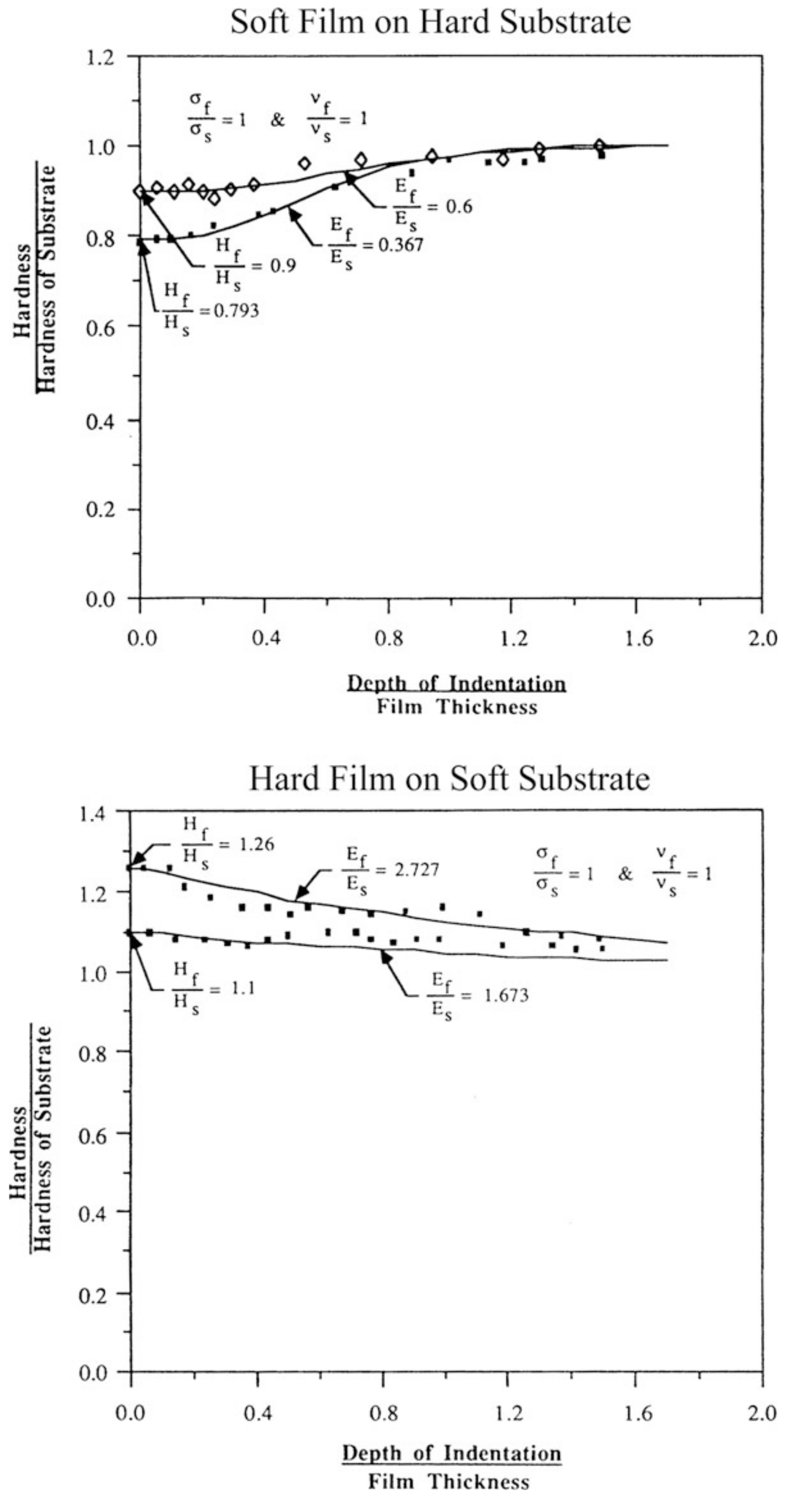

Fig. 5.16 Effect of relative elastic moduli of the film and the substrate (E_f/E_s) on the composite hardness as a function of the depth of indentation for a soft film on a hard substrate and a hard film on a soft substrate. Yield strengths (σ) and Poisson's ratio (ν) are same for both substrates and films (adapted from Bhattacharya and Nix 1988b)

in which the film and substrate have different yield strengths, it is observed that the variation of hardness with depth of indentation in these cases is qualitatively similar to cases in which the film and substrate have different elastic moduli.

Doerner and Nix (1986) modeled the influence of the substrate on the elastic measurement of very thin film empirically in an indentation test using the following expression for the compliance:

$$C = \frac{dh}{dW} = \frac{1}{2}\left(\frac{\pi}{A}\right)^{1/2}\left\{\frac{1-v_f^2}{E_f}\left[1 - exp\left(\frac{-\alpha t_f}{\sqrt{A}}\right)\right] + \frac{1-v_s^2}{E_s} exp\left(\frac{-\alpha t_f}{\sqrt{A}}\right) + \frac{1-v_i^2}{E_i}\right\} + b$$

where the subscripts f, s, and i refer to the film, substrate, and indenter, respectively. The term $\sqrt{A}$ is equal to $(24.5)^{1/2}h_c$ for the Vickers or Berkovich indenter. The film thickness is t_f, and b is the y-intercept for the compliance versus 1/depth plot, obtained for the bulk substrate, which can be neglected in most cases. The weighing factors $\left[1 - exp\left(-\alpha t_f/\sqrt{A}\right)\right]$ and $exp\left(-\alpha t_f/\sqrt{A}\right)$ have been added to account for the changing contributions of the substrate and film to the compliance. The factor α can be determined empirically.

King's analysis (1987) verified that Eq. 5.20 is an excellent functional form for describing the influence of the substrate and theoretically determined the values of α for various indenter shapes. The value of α was found to depend on the indenter shape and size and film thickness, and was found to be independent of E_i/E_s. The values of α as a function of $\sqrt{A}/t_f$ for Berkovich (triangular) indenters are shown in Fig. 5.17. The values of α were found to be similar for square and triangular indenters. Bhattacharya and Nix (1988b) analyzed the deformations of a layered medium in contact with a conical indenter using the finite-element method. Their analysis also verified the relationship given in Eq. 5.20.

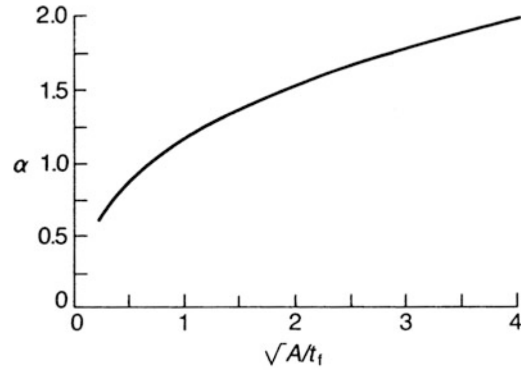

Fig. 5.17 Parameter α as a function of normalized indenter size for Berkovich indenter indenting a layered solid surface (adapted from King 1987)

5.3 Measured Mechanical Properties of Engineering Materials

We present representative mechanical properties data obtained on various materials and coatings (Bhushan 1999a; Bhushan and Li 2003).

5.3.1 Load–Displacement Curves

A variety of mechanical phenomena, such as transition from elastic to plastic deformation, creep deformation, formation of subsurface cracks, and crystallographic phase transition, can be studied by the load-displacement curves obtained at different loading conditions (Pethica et al. 1983; Doerner and Nix 1986; LaFontaine et al. 1990, 1991; Pharr et al. 1990; Page et al. 1992; Oliver and Pharr 1992; Pharr 1992; Whitehead and Page 1992; Gupta et al. 1993, 1994; Gupta and Bhushan 1994, 1995a, b; Bhushan et al. 1995, 1996a, b; Bhushan and Gupta 1995; Bhushan 1999a; Bhushan and Li 2003; Palacio and Bhushan 2010, 2013; Kumar and Bhushan 2015; Cho and Bhushan 2016).

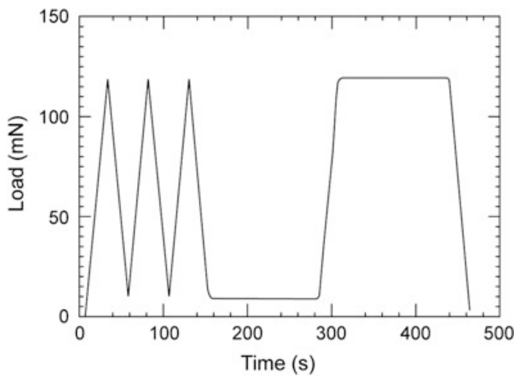

Fig. 5.18 A typical load-time sequence for mechanical property measurements (adapted from Oliver and Pharr 1992)

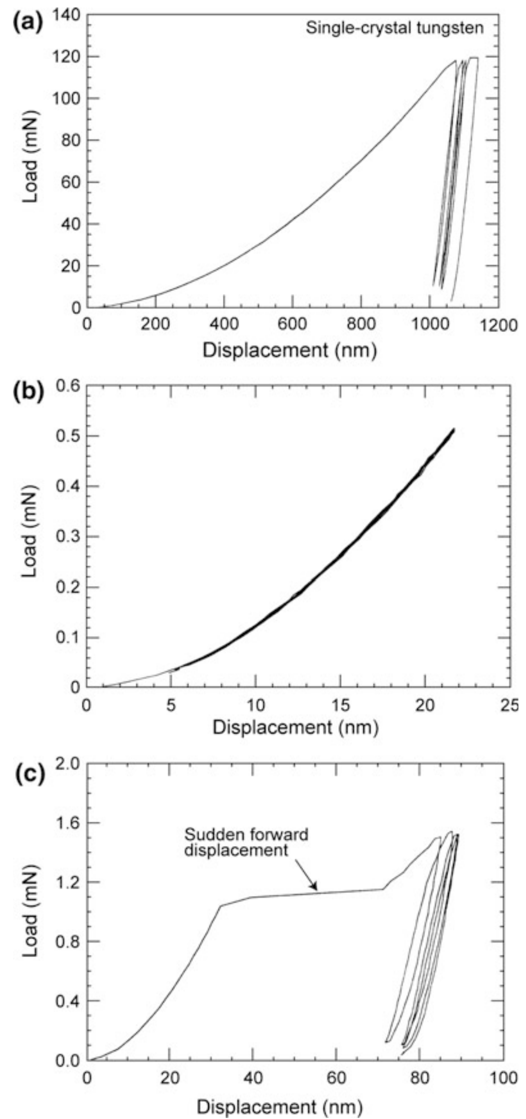

Fig. 5.19 Load-displacement curves for an electro-polished single-crystal tungsten **a** at a peak load of 120 mN, **b** at a peak load of 0.5 mN (elastic contact), and **c** at a peak load of 1.5 mN showing the yield point (adapted from Oliver and Pharr 1992)

Mechanical properties measurements often are made using the following loading sequence: three loading-unloading cycles, hold for 100 s at 10% of the peak load, reload, hold for 100 s, and unload (Fig. 5.18) (Oliver and Pharr 1992). Load-displacement curves for electropolished single-crystal tungsten, fused silica, and single-crystal silicon (110) are shown in Figs. 5.19, 5.20 and 5.21, respectively. Tungsten data are typical of materials in which the hardness is relatively small compared to the modulus, as is observed in most metals; most of the indenter displacement in these metals is accommodated plastically and only a small portion is recovered on unloading. Fused silica and silicon are harder which show larger elastic recovery during unloading, the largest being that for fused silica.

The unloading/reloading behaviors of the various materials are different. For tungsten, Fig. 5.19 shows that the peak load displacements shift to higher values in successive loading/unloading cycles (Oliver and Pharr 1992). In addition, the relatively large displacement just prior to final unloading is due to creep during the 100 s hold period at peak load. Indentation at a very low load of 0.5 mN caused only elastic displacements, Fig. 5.19b. At two higher peak loads, the indentation is elastic and plastic, as shown in Fig. 5.19a, c, respectively. When a threshold load of about 1 mN is reached, a sudden jump in displacement corresponding to the onset of plasticity is observed, and a permanent hardness impression is formed. At mid-load (Fig. 5.19c), a distinct hysteresis loop is observed, as might be expected if there were a small amount of reverse plasticity upon loading. However, the looping degenerates with cycling after three or four cycles, the load-displacement behavior is largely elastic. The

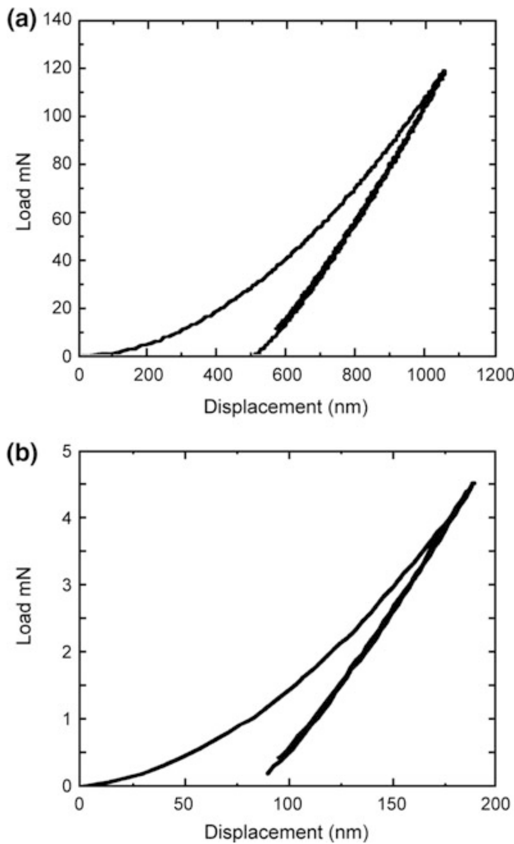

Fig. 5.20 Load-displacement curves for fused silica **a** at a peak load of 120 mN, and **b** at a peak load of 4.5 mN (adapted from Pharr 1992)

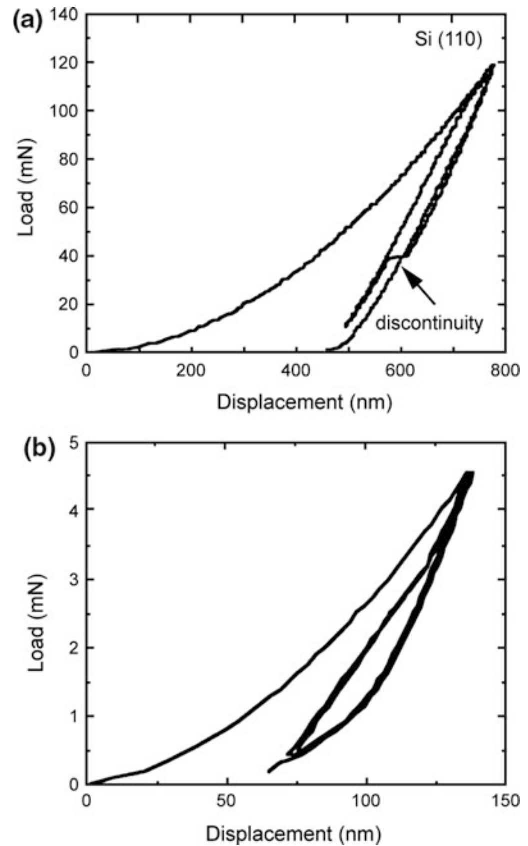

Fig. 5.21 Load-displacement curves for single-crystal Si (110) **a** at a peak load of 120 mN, and **b** at a peak load of 4.5 mN (adapted from Pharr 1992)

unloading/reloading curves for fused silica are nearly the same, Fig. 5.20 (Pharr 1992). The near-perfect reversibility suggests that at peak loads of 120 and 4.5 mN, deformation after initial unloading is almost entirely elastic.

The loading/unloading behavior of silicon shown in Fig. 5.21, is in sharp contrast to other materials (Figs. 5.19 and 5.20) (Pharr et al. 1989, 1990; Page et al. 1992; Pharr 1992). The data presented in Fig. 5.21 were taken over two cycles of loading and unloading. At high peak loads, the initial unloading curve for silicon is not at all smooth, but exhibits a discontinuity, Fig. 5.21a. At lower peak loads, the behavior changes, and below some critical value the discontinuity is no longer observed, Fig. 5.21b. However, at this load the load-displacement behavior shows another anomalous feature—a large hysteresis, which shows no sign of degeneration through several cycles of deformation. The fact that the curves are highly hysteretic implies that deformation is not entirely elastic. The discontinuity at high loads and the nondegenerative hysteresis at low loads are quite unique to silicon and are observed in each of the (100), (110), and (111) orientations. The load below which the discontinuity disappears and the hysteresis becomes apparent is generally in the range 5–20 mN. Pharr (1992) concluded that larger hysteresis observed in the unloading curve at low loads is due to a pressure-induced phase transformation from its normal diamond cubic form to a β-tin metal phase. At some point in the transformation, an amorphous phase is formed,

whose evidence is reported by Callahan and Morris (1992). The discontinuity in displacement observed during unloading at peak loads of greater than about 15 mN are believed to be due to formation of lateral cracks which form at the base of the median crack which results in the surface of the specimen being thrust upward, schematically shown in Fig. 5.22 (Pharr 1992). Lateral cracking is aided by the phase transformations.

AE signal collected during the indentation process allows understanding of the deformation process. The load-displacement curve for Si(100) with a 120 mN load is shown in Fig. 5.23a, and the first AE signal that was recorded for this test is shown in Fig. 5.23b (Weihs et al. 1992). The AE signals correlated with small jumps in tip displacement. After testing, radial cracks were visible at the corners of indentation. AE events such as the one shown in Fig. 5.23b were

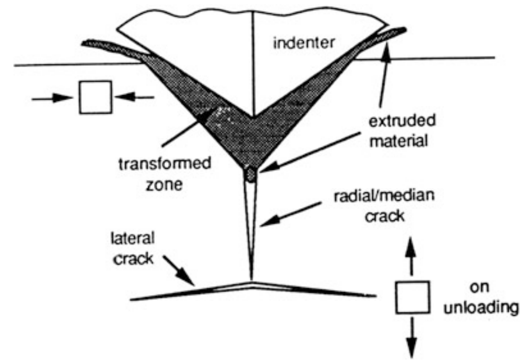

Fig. 5.22 A schematic illustration of the coupling of the phase transformation and cracking during indentation of single-crystal silicon (adapted from Pharr 1992)

recorded at applied load as low as 48 mN on loading. In the final stages of unloading, small AE signals that had an inverted shape compared to Fig. 5.23b were detected occasionally. Goken and Kempf (2001) reported that the

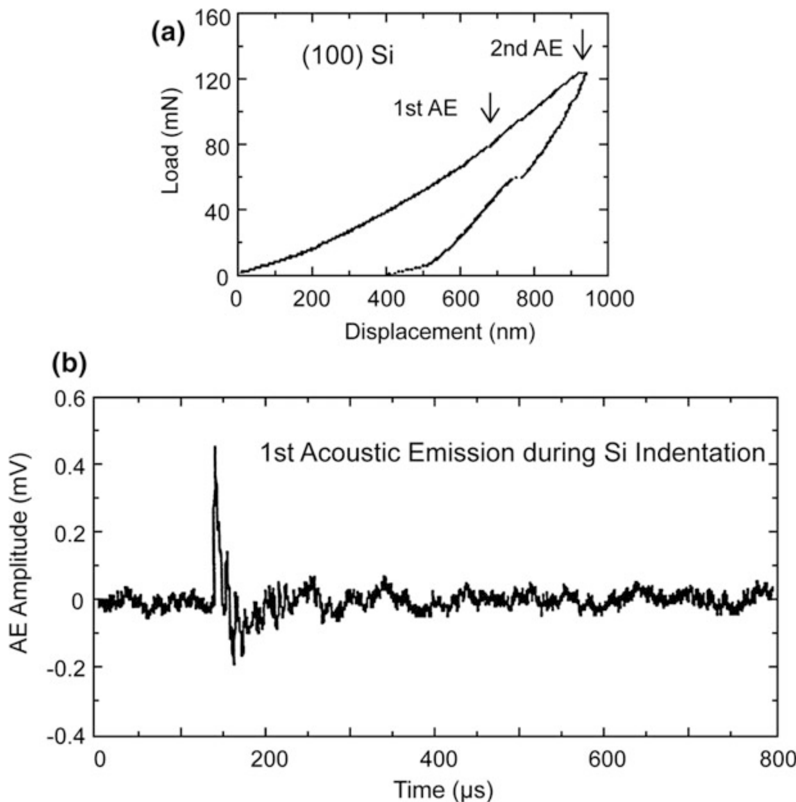

Fig. 5.23 **a** Load-displacement curves for single-crystal Si(100), and **b** AE amplitude as a function of time during loading (adapted from Weihs et al. 1992)

load-displacement curves obtained by nanoindentations on most metallic and intermetallic materials show discontinuities or pop-ins during the initial part of loading. These pop-ins mark a sharp transition from pure elastic loading to a plastic deformation of the specimen surface, thus correspond to an initial yield point. On smooth surfaces pop-ins are observed frequently, but not on surfaces with a high roughness. Step edges on the surface are believed to act as dislocation sources for the initial yield events. It should be noted that the pop-in load determines a minimum load necessary to generate plastic indentation.

Gupta et al. (1993, 1994) and Gupta and Bhushan (1994) reported that hysteresis in cyclic indentation and discontinuity kinks in the unloading curve are considerably reduced by ion implantation of compound forming species O^+ and N^+ into single-crystal silicon. They further reported that amorphous silicon films did not exhibit either hysteresis in the cyclic indentation or a discontinuity kink in the indentation loads ranging from 1 to 90 mN. This suggests that for a perfect amorphous structure, hysteresis does not occur because of the absence of crystallographic pressure-induced phase transition during cyclic loading and unloading. In addition, the disordered structure does not allow the nucleation and propagation of the lateral cracks beneath the indentation.

The load-displacement curve for indented Ni films on a glass substrate is shown in Fig. 5.24a (Weihs et al. 1992). The Ni films debonded from their substrates at forces ranging between 130 and 250 mN. The debonding events were marked by the indenter tip jumping downward as "chunks" of the Ni film buckled away from the underneath. The indenter tip jumped a distance equal to the film thickness as it initially debonded. Figure 5.24b also shows the corresponding

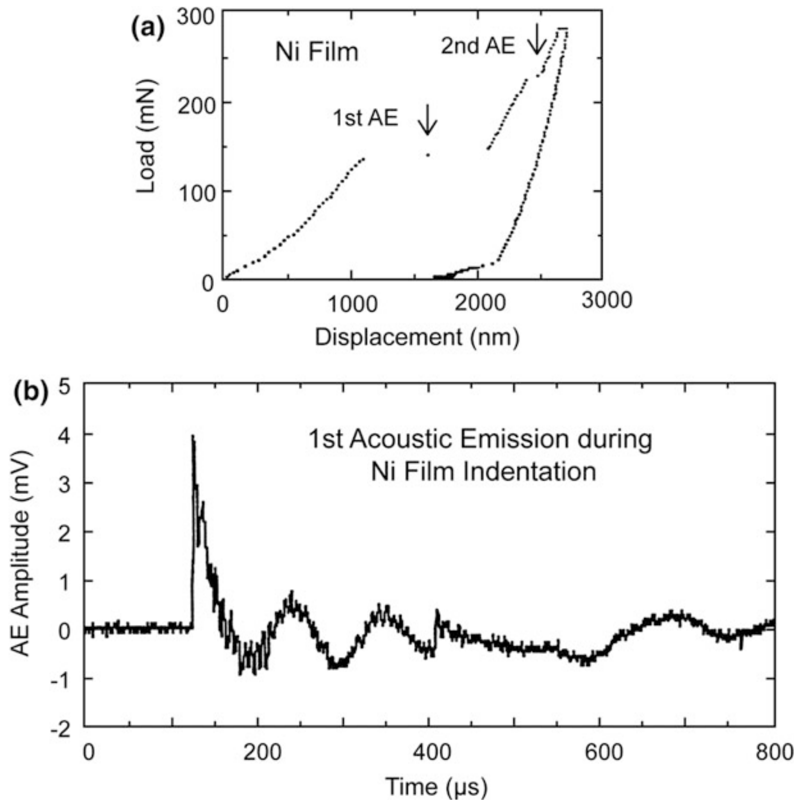

Fig. 5.24 **a** Load-displacement curves for Ni film on glass substrate, and **b** AE amplitude as a function of time during loading (adapted from Weihs et al. 1992)

AE trace with a rise time of 1.8 µs. In this particular test, debonding continued at higher forces and a second AE event was recorded. After each test, optical microscopy confirmed the delamination of the film from underneath the indenter.

Li and Bhushan (1999c) measured mechanical properties of 100-nm thick DLC coatings deposited on a silicon substrate at a peak load of 0.2 mN using a Keysight-type nanoindenter by four different deposition techniques: filtered cathodic arc (FCA); ion beam (IB); electron cyclotron resonance-chemical vapor deposition (ECR-CVD); and sputtered (SP). Kulkarni and Bhushan (1997) measured mechanical properties of a 20-nm thick DLC coating deposited by FCA at a peak load of 100 µN using a Hysitron nanoindenter, Fig. 5.25. The data for Si(100) also is shown for comparison. The indentation depths at the peak load ranged from 6 to 8 nm, smaller than the coating thickness. Indentation depth of the coating at the peak load was slightly lower than that of the Si substrate, exhibiting less plastic deformation, which suggests higher hardness.

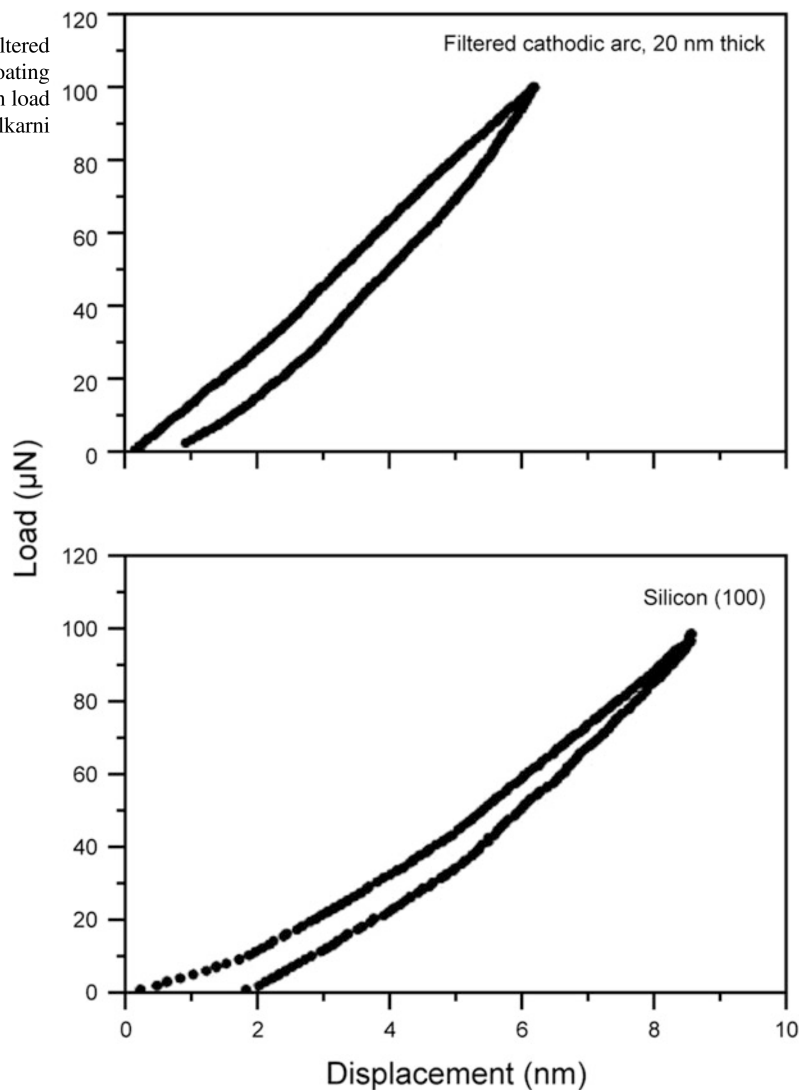

Fig. 5.25 Load-displacement curves for a 20 nm thick filtered cathodic arc deposited DLC coating and Si(100) at peak indentation load of 100 µN (adapted from Kulkarni and Bhushan 1997)

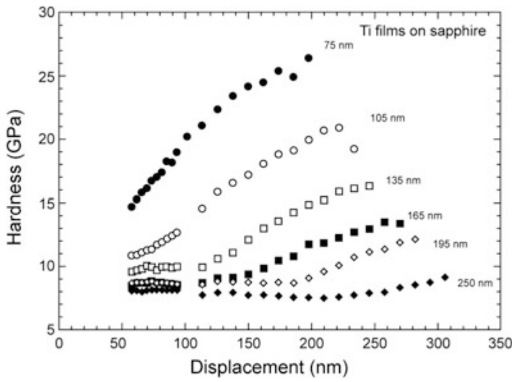

Fig. 5.26 Indentation hardness as a function of displacement for Ti films on sapphire substrates. Numbers next to each set of data correspond to the coating thickness (adapted from Fabes et al. 1992)

5.3.2 Hardness and Elastic Modulus Measurements

It has been reported earlier that true hardness of the films can be obtained if the indentation depth does not exceed about 30% of the film thickness. At higher indentation depths, the composite hardness changes with the indentation depth. Measured hardness values of soft, Ti films on a hard, sapphire substrate are presented in Fig. 5.26. We note that hardness increases with a decrease in the film thickness or increase in the indentation depth, as expected. The film hardness is the steady-state hardness (left portion), independent of the indentation depth.

Fig. 5.27 Hardness and elastic modulus as a function of load for six bulk materials —mechanically polished single-crystal aluminum, electro-polished single-crystal tungsten, soda-lime glass, fused silica, (001) single-crystal sapphire, and (001) single-crystal quartz (adapted from Oliver and Pharr 1992)

Hardness and elastic moduli for six bulk materials are shown in Fig. 5.27. The data show that there is a very small indentation size effect in several materials on the hardness values. The moduli remains more or less constant over the entire range of load. The hardness and modulus values at the two highest loads are comparable with the literature values (Oliver and Pharr 1992). Measured values of various magnetic disk substrates and single-crystal crystal, as a reference, are shown in Fig. 5.28. A summary of measured nanoscale values and published micro/macroscale data are shown in Table 5.2. Scale effects are observed. Fracture toughness data will be discussed later.

5.3.3 Scale Effects on Nanomechanical Properties

In order to study the effect of contact depth, including shallow depths on the order of 5–10 nm, an AFM-based, Hysitron-type indenter is used frequently (Bhushan et al. 1996a). Figure 5.29a shows the load-displacement data for Si(100) and GaAs(100) at displacements as low as 2 nm (Bhushan et al. 1996a). Note that the loading and unloading curves are not smooth, but exhibit sharp discontinuities, particularly at high loads, shown by arrows. Discontinuities in the loading parts of the curve result from slip. Pharr et al. (1990) and Pharr (1992) reported the evidence of discontinuities in the unloading curves, and hypothesized that a sharp discontinuity is due to the formation of a lateral crack, which forms at the base of median crack, causing the surface of the specimen to be thrust upwards.

Figure 5.29b shows the load-displacement curves during three loading and unloading cycles for single-crystal Si(100) (Bhushan et al. 1996a). The unloading and reloading curves show a large “hysteresis,” which shows no sign of degeneration through three cycles of deformation, and the peak load displacements shift to higher values in successive loading–unloading cycles. Pharr et al. (1989, 1990), and Pharr (1992) also have observed hysteresis behavior in silicon at similar loads using a nanoindenter. The fact that the curves are highly hysteric implies that deformation is not entirely elastic. It is believed that large hysteresis is due to a pressure-induced phase transformation from its normal diamond cubic form to a β-tin metal phase (Bhushan 1999a).

The nanohardness values for single-crystal Si (100) as a function of residual depth are plotted in Fig. 5.30 (Bhushan et al. 1996a). It is clear that the hardness of silicon increases with a decrease in the load and corresponding indentation depth. A nanoindentation hardness value was about 11.5 GPa at a peak indentation depth of 750 nm, which is slightly higher than the bulk hardness value of silicon of 9–10 GPa (Anonymous 1988). The data shows that the hardness exhibits size effect. At smaller volumes, there is a lower probability of encountering material defects. Furthermore, at small volumes, there is an increase in the stress necessary to operate dislocation sources (Gane and Cox 1970; Sargent 1986). According to the strain gradient plasticity theory advanced by Fleck et al. (1994), large strain gradients inherent in small indentations lead to accumulation of geometrically necessary dislocations that cause enhanced hardening. In addition, an increase in hardness at lower indentation depths may result from contributions of the surface films. These are some of the plausible explanations for the increase in hardness at smaller volumes.

Kulkarni and Bhushan (1996a, b) measured the effect of contact depth on mechanical properties for single-crystal Al(100). Figure 5.31a shows the load-displacement curves at six different peak indentation loads of 15, 25, 50, 100, 300, and 500 μN. For the case of 15 μN peak load, the residual depth is about 3 nm. The peak depth at 500 μN load is almost 200 nm. The indenter displacement results in plastic deformation with very little elastic recovery (Bhushan et al. 1996a; Kulkarni and Bhushan 1996a, b). The arrow marks in the loading portion of the curve indicate discontinuities (forward jump) in displacement at higher loads. As indicated earlier,

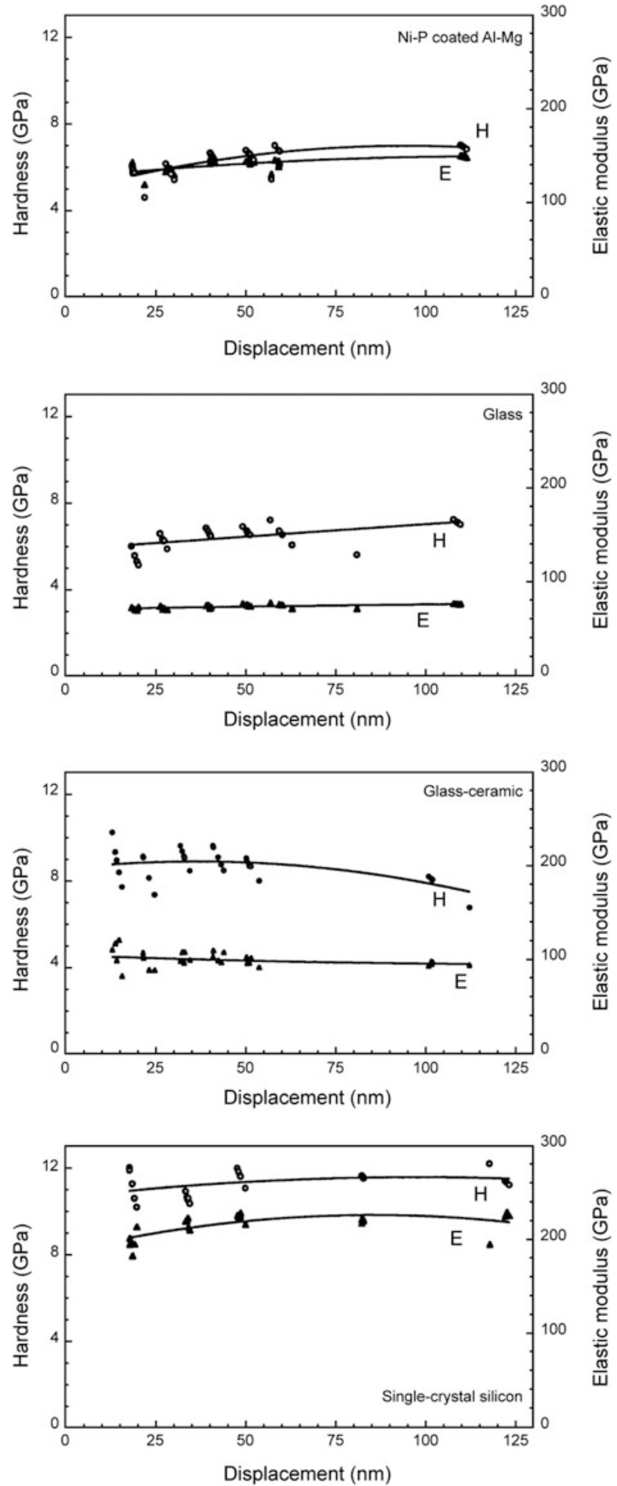

Fig. 5.28 Hardness and elastic modulus as a function of displacement (load ranging from 0.1 to 2.5 mN) for mechanically-polished 10-μm thick electroless Ni–P film on Al–Mg alloy 5086, chemically-strengthened alkali-aluminosilicate glass, chain silicate glass-ceramic (polycrystalline) (canasite by corning), and single-crystal Si (111) (adapted from Bhushan and Gupta 1995)

Table 5.2 RMS roughness values measured by an atomic force microscope, hardness and elastic modulus values measured by using a nanoindenter (at an indentation depth of about 20 nm), and fracture toughness measured by using a Vickers microindenter (Bhushan and Gupta 1995)

Material	RMS roughness (nm)	Hardness[a] (GPa)	Elastic modulus[b] (GPa)	Crack length, c (μm)	Fracture toughness[c] (MPa $m^{1/2}$)
Ni–P/Al–Mg	3.6	6.0 (5.5)	130 (200)	No cracks	–
Chemically-strengthened glass	1.1	6.0 (5.8)	85 (73)	Significant cracking	(0.9)
Glass-ceramic	6.1	8.5 (5.5)	100 (83)	59.4	0.65 (4.0)
Single-crystal Si(111)	0.95	11.0 (9–10)	200 (180)		

[a]Values in parentheses are the reported values measured by conventional Vickers indentation method
[b]Values in parentheses are the reported values measured by conventional tensile pull test method
[c]Values in parentheses are the reported values measured by the chevron-notched short-bar method

discontinuities probably result from slip of the tip (arising because of stick-slip friction effects) and/or because of lateral cracks developed at the corners of indentation (Weihs et al. 1992).

Figure 5.31b shows the load displacement curves during three loading and unloading cycles. A hysteresis was observed after cyclic loading and unloading at peak indentation load of 100 μN. The peak load displacement shifts to higher values in successive cycles with no sign of degeneration, indicating that the deformation is not entirely elastic, even after three cycles (Oliver and Pharr 1992; Bhushan et al. 1996a). The hardness and elastic modulus as a function of load (or indentation depth) are shown in Fig. 5.32. The elastic modulus remains almost constant for all values of loads owing to the constant modulus assumption. Hardness decreases with increasing load. These results are consistent with earlier data on Si(100). As compared to single-crystal Si(100), aluminum has a higher dislocation density. Thus, the probability of the tip encountering defects is high. In addition, surface films may play a role in the higher hardness value observed at lower loads.

5.3.4 Time-Dependent Viscoelastic/Plastic Properties

Viscoelastic solids such as polymers creep at temperatures as low as room temperature. Most materials, including ceramics and even diamond, creep some at temperatures well below half their melting points. Indentation creep, load relaxation, and strain-rate sensitivity tests are used for measurement of the time-dependent flow of materials. These three tests provide the measure of viscoelastic/viscoplastic properties, and any of them can be used (Bhushan 1999a; Bhushan and Li 2003).

In the indentation creep test, the hardness indenter maintains its load over a period of time under well-controlled conditions, and changes in indentation size are monitored (Wesbrook, 1957; Mulhearn and Tabor 1960; Walker 1973; Bhushan et al. 1996a; Kulkarni and Bhushan 1996b, 1997; Li et al. 2001). The analysis of creep is more complex than that of creep data obtained using a conventional technique because of the shape of the tip. Indentation stress acting on the sample decreases with time as the contact area increases.

In the indentation load relaxation test, the indenter first is pushed into the sample at a fixed displacement rate until a predetermined load or displacement is achieved and the position of the indenter then is fixed (Bhushan 1999a; Bhushan and Li 2003). The material below the indenter is elastically supported and will continue to deform in a non-elastic manner, thereby tending to push the indenter farther into the sample. Load relaxation is achieved by conversion of elastic strain in the sample into inelastic strain in the sample. During the test, the load and position of the

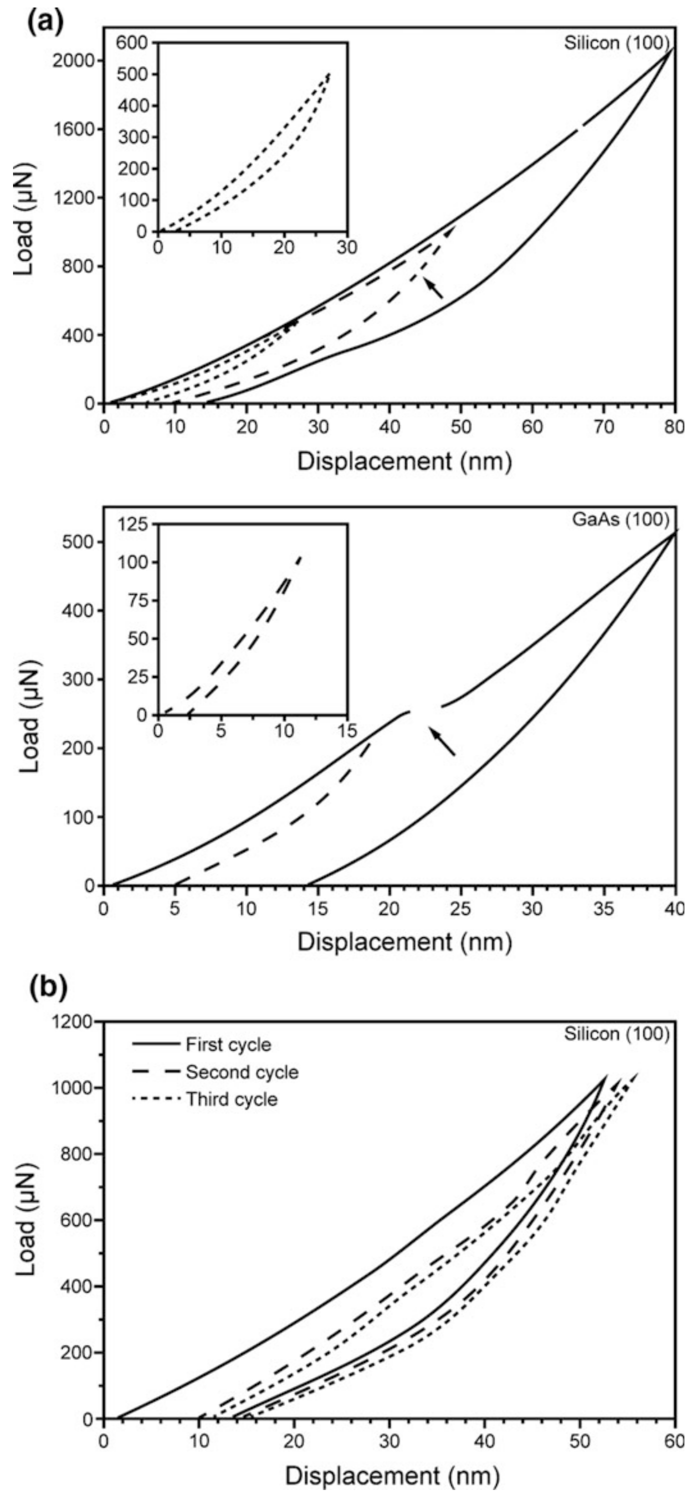

Fig. 5.29 Load-displacement curves **a** at various peak loads for Si(100) and GaAs (100), and **b** during repeated loading-unloading cycles for Si(100). Sharp discontinuities in (**a**) are shown by *arrows* (adapted from Bhushan et al. 1996a)

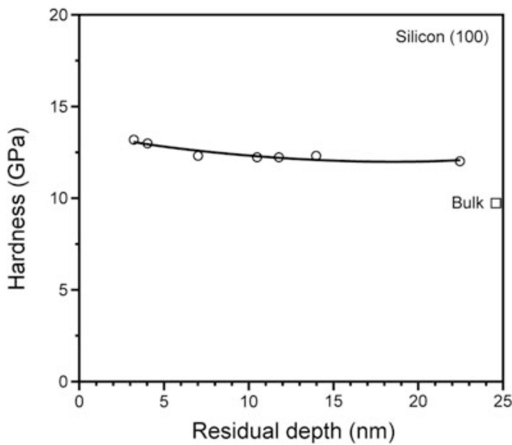

Fig. 5.30 Indentation hardness as a function of residual indentation depth for Si(100). Bulk hardness value is shown for reference (adapted from Bhushan et al. 1996a)

indenter and the specimen are monitored continuously. Typically, the indenter motion is held constant and the changes in the load are monitored as a function of time.

To measure strain rate sensitivity, individual indentations are performed at a prescribed loading rate that is varied from one indentation to another (Mayo and Nix 1988; Bhushan et al. 1996a; Kulkarni and Bhushan 1996b). The values of the indentation pressure and strain rates from tests performed at different loading rates are compared at a common indentation depth.

Li et al. (1991) conducted creep experiments using a nanoindenter on silicon at several hundred μN load. Their data exhibited significant creep only at high temperatures (greater than or equal to 0.25 times the melting point of silicon). The mechanism of dislocation glide plasticity was believed to dominate the indentation creep process. Using a Hysitron nanoindenter, indentation creep and strain rate sensitivity experiments were conducted on single-crystal silicon, single-crystal aluminum, and DLC coatings at low loads on the order of 1 μN or less (Bhushan et al. 1996a; Kulkarni and Bhushan 1996b, 1997). Figure 5.33a shows the load-displacement curves for single crystal Si(100) at various peak loads held at 180 s (Bhushan et al. 1996a). Note that significant creep occurs at room temperature.

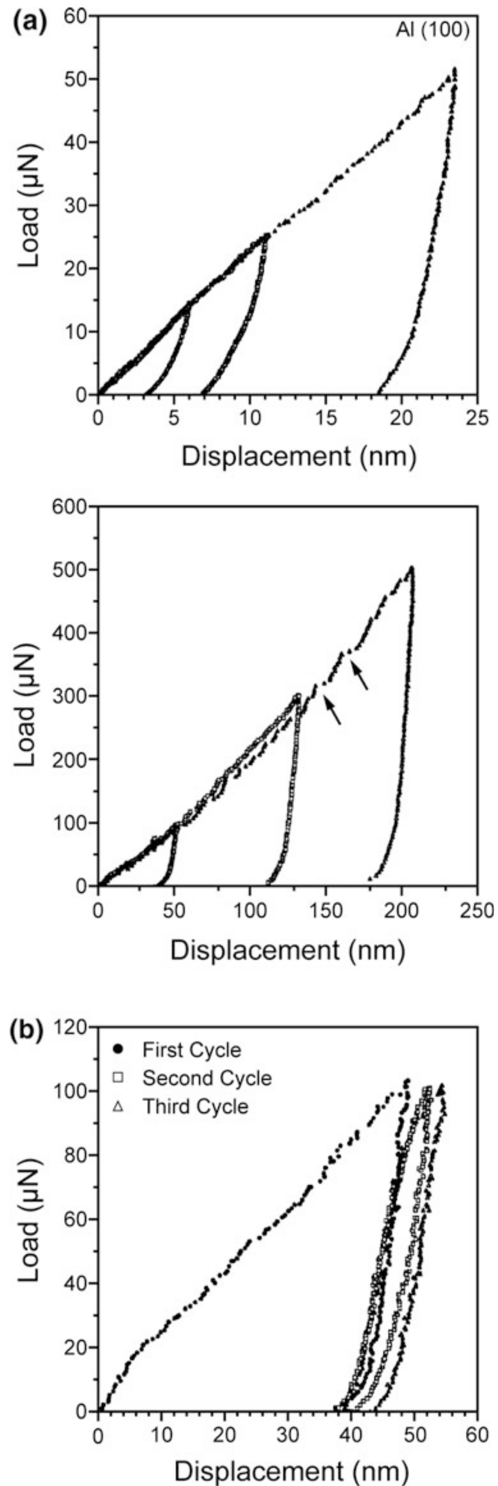

Fig. 5.31 Load-displacement curves for single-crystal Al(100) **a** at peak loads of 15, 25, 50, 100, 300, and 500 μN, and **b** during three successive loading/unloading cycles at a peak load of 100 μN. *Arrows* in (**a**) indicate the forward jump in the displacement (adapted from Kulkarni and Bhushan 1996b)

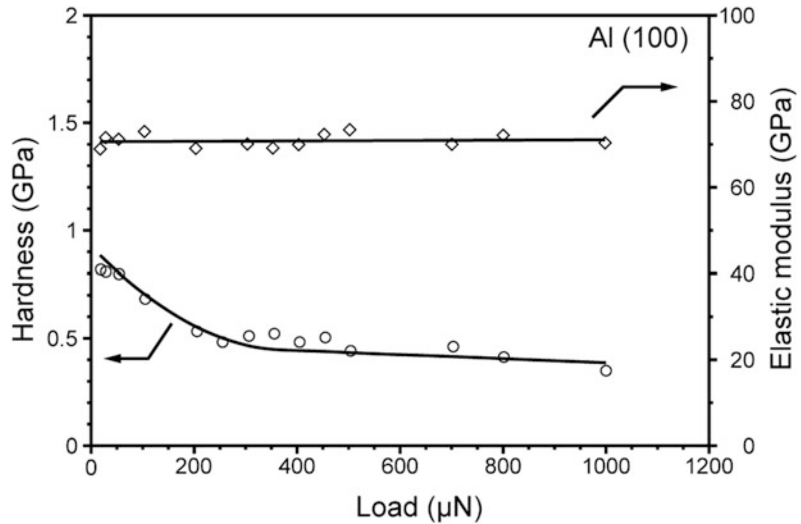

Fig. 5.32 Hardness and elastic modulus of elasticity as a function of load for single-crystal Al(100) (adapted from Kulkarni and Bhushan 1996b)

To demonstrate the creep effects further, the load-displacement curve for the lowest peak load of 500 µN held at 30 s also is shown as an inset, along with the data at no hold (0 s) for comparison. Again, creep is observed even at a hold period of 30 s. In this study, since indentation tests were performed at very low loads in ambient conditions, it is believed that creep of hydrated layers were being measured, rather than that of the bulk silicon. Hydrated layers are expected to exhibit viscoelastic properties. To study strain-rate sensitivity of silicon, experiments were conducted at two different rates of loading (Fig. 5.33b). Note that a change in the loading rate of a factor of about five results in a change in the load-displacement data. Creep effects and strain-rate sensitivity to single-crystal Al(111) and DLC coatings also were reported by Kulkarni and Bhushan (1996b, 1997).

5.3.5 Continuous Stiffness Measurement

Continuous stiffness measurements (CSM) are used for continuous measurement of sample stiffness or compliance (related to elastic modulus) during indentation (Oliver and Pharr 1992; Bhushan 1999a; Li and Bhushan 2002a; Bhushan and Li 2003). A representative continuous stiffness data for single-crystal tungsten for the indentation data in Fig. 5.19b are presented in Fig. 5.34a for fully elastic contact. Comparisons of these data show that the measured contact stiffness and, thus, the contact area does increase and decrease in the way that would be expected based on the loading history. The continuous stiffness data for indentation of single-crystal tungsten at 1.5 mN load (plastic contact, Fig. 5.19c) is shown in Fig. 5.34b for a fully plastic contact. It is seen that for each of the four unloadings, the contact stiffness changes immediately and continuously as the specimen is unloaded. Thus, the contact area, which varies in the same way as the contact stiffness, is not constant during the unloading of the plastic hardness impression, even during the initial stages of unloading.

The CSM method can be used to study graded materials and multilayered structures (Bhushan 1999a; Li and Bhushan 2002a; Bhushan and Li 2003). For a uniform material, from Eqs. 5.4a and 5.6, contact stiffness, S, is linearly proportional to contact depth, h_c. For a non-uniform material, a linear relationship between S and h_c does not exist. Therefore, the CSM technique can be used to study the mechanical properties of graded materials (such as magnetic tapes) and multilayered structures (such as magnetic rigid disks) by monitoring the change in contact stiffness, elastic modulus, and hardness as a function of contact depth (Li and Bhushan 2000a, b,

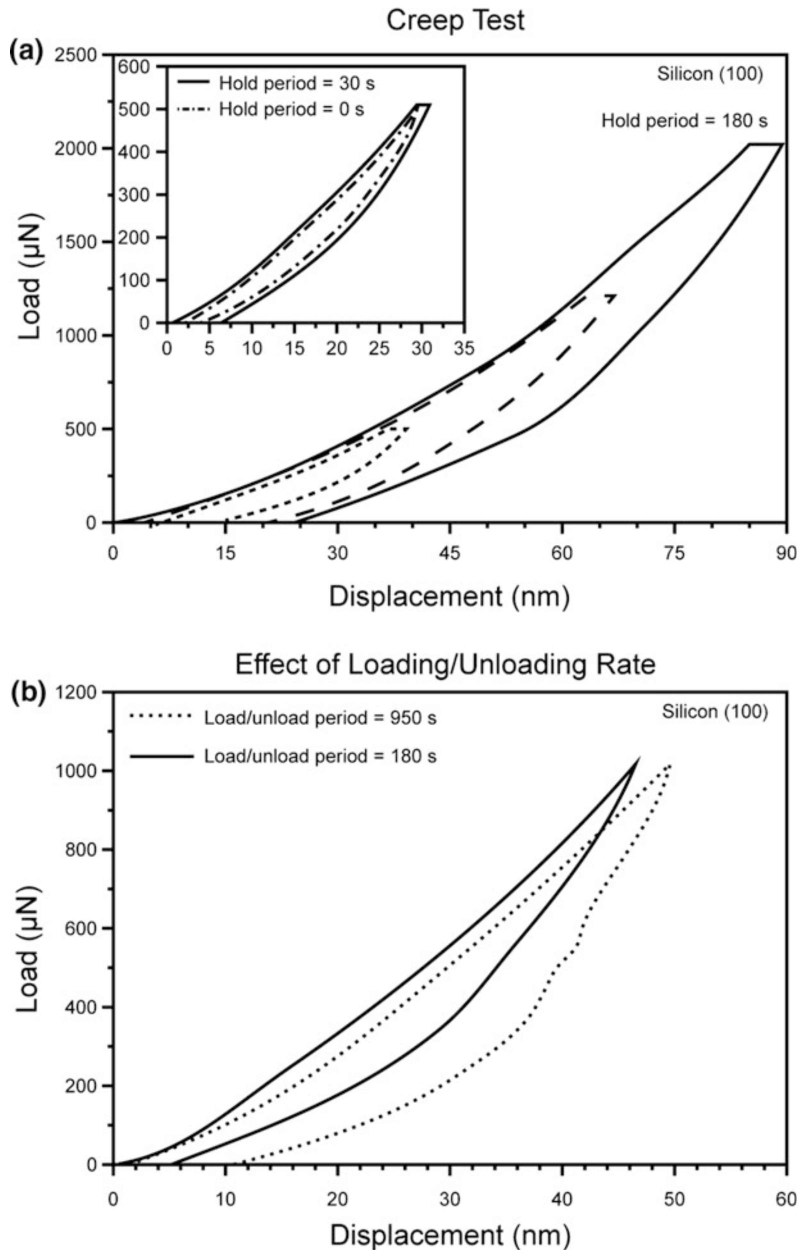

Fig. 5.33 **a** Creep behavior and **b** loading/unloading rate behavior of single-crystal Si (100) (adapted from Bhushan et al. 1996a)

2001a, b, 2002a; Li et al. 2001). The schematics of contact stiffness as a function of contact depth for indentations made on uniform and graded materials are shown in Fig. 5.35. The contact stiffness, elastic modulus, and hardness as a function of contact depth for a magnetic rigid disk and a magnetic tape with multilayered structures are shown in Fig. 5.36a, b, respectively. For the magnetic disk, from the variations in contact stiffness, elastic modulus and hardness, one can distinguish one layer from another easily (Fig. 5.36a). In the case of the magnetic tape, observed continuous decrease in the rate of change of the contact stiffness suggests that the tape coating has graded properties (Fig. 5.36b). The elastic modulus values obtained at a shallow indentation depth were the same as those measured from tensile tests for the tape.

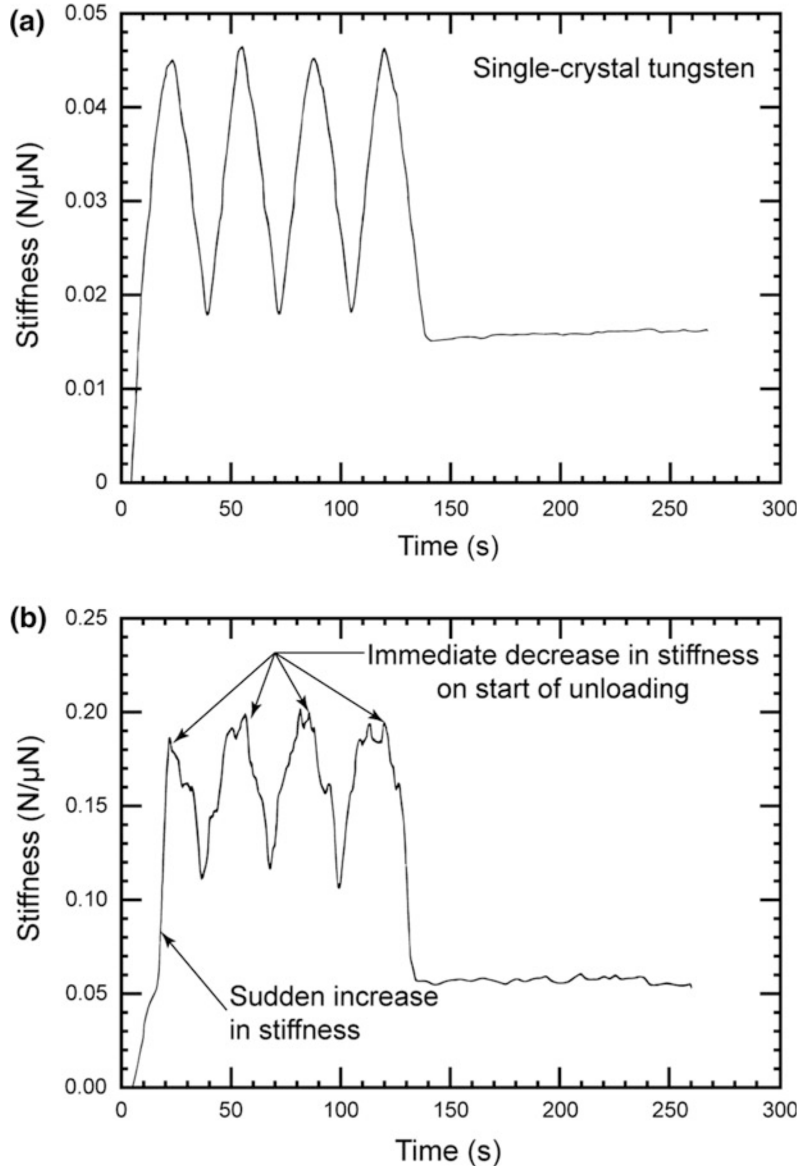

Fig. 5.34 Contact stiffness versus time **a** for a fully elastic contact and **b** for a fully plastic contact on an electropolished single-crystal tungsten measured with the continuous stiffness technique (adapted from Oliver and Pharr 1992)

The CSM technique also has been used to perform nanoscale indentation creep testing (Li and Bhushan 2000b). In an indentation creep test, a constant load is applied to the indenter and the change in indentation depth (displacement) is monitored as a function of time. Compared to conventional tensile creep tests, the CSM indentation creep experiments are particularly useful as they simulate creep resulting from asperity contacts in a sliding contact. The CSM technique has been used to study the creep behavior of bulk materials (Syed Asif and Pethica 1997), graded materials, and multilayered solids (Li and Bhushan 200b, 2001a, b, 2002a; Li et al. 2001). Figure 5.37 shows the CSM indentation creep results for a magnetic tape. The tape exhibits an increase in indentation displacement and a decrease in mean stress with time, indicating that stress relaxation occurred during the hold segment. The contact stiffness remains nearly constant during the 600 s hold segment,

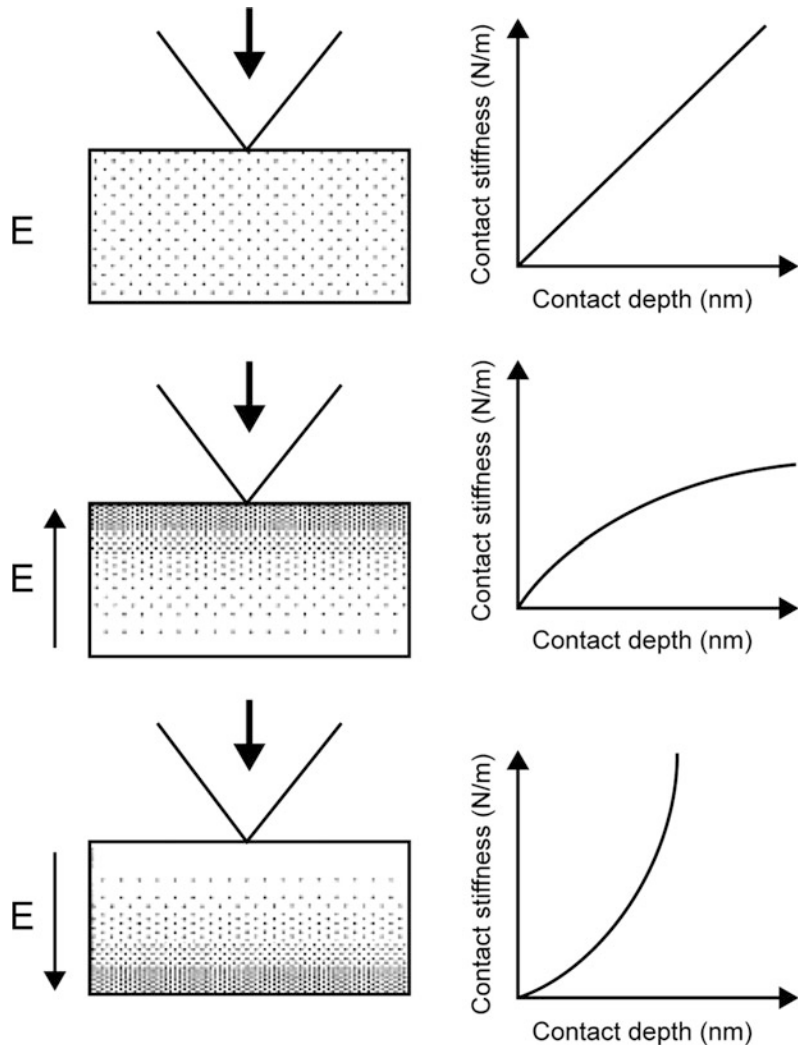

Fig. 5.35 Schematics of contact stiffness as a function of contact depth for indentations made on uniform and graded materials (adapted from Li and Bhushan 2002a)

indicating that the contact between the tip and the tape does not change significantly.

Nanoscale damage caused by fatigue is of critical importance to the reliability of ultra-thin protective overcoats and micro/nanostructures. The cyclic loading used in the CSM makes the technique useful for evaluation of nanofatigue, which will be described later.

5.3.6 Mechanical Properties of Nano-objects

Nano-objects can be described as a single material or composite having at least one dimension that is between 1 and 100 nm (Bhushan et al. 2014; Maharaj and Bhushan 2015). They come in a variety of discrete geometries that include spheres, tubes, rods, wires, and pillars. Compared to their bulk material counterparts, many nano-objects exhibit enhanced mechanical, electrical, magnetic, chemical, and friction, and wear-reducing properties. This makes them attractive for use in many applications on the macro- to nanoscale.

Nano-objects are used in various applications that include drug delivery for cancer treatment, oil detection, contaminant removal, catalysis, and tribology on the macro- to nanoscale. As an example, nano-objects made of various materials

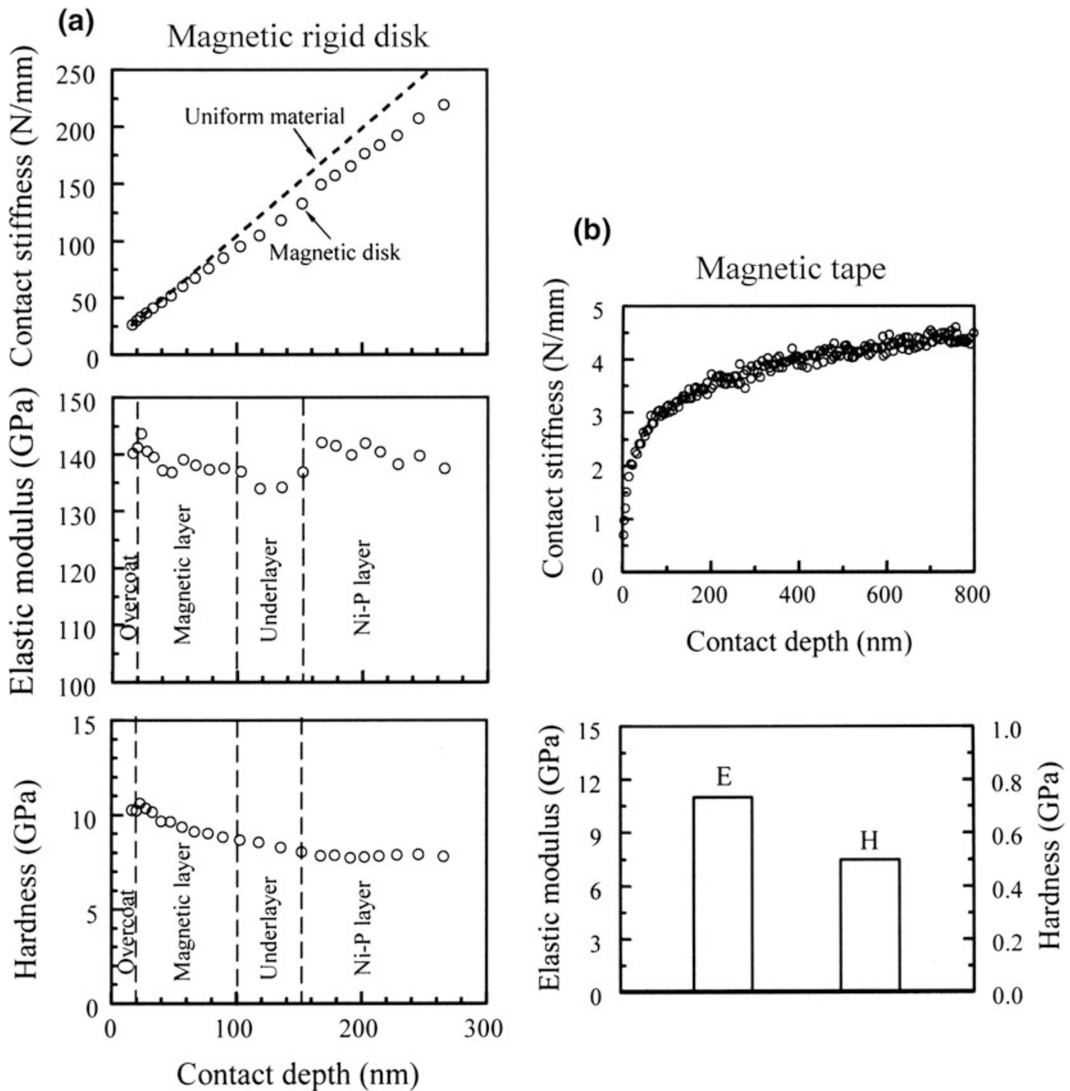

Fig. 5.36 **a** Contact stiffness, elastic modulus and hardness as a function of contact depth for a magnetic rigid disk with a multilayered structure, and **b** contact stiffness as a function of contact depth, elastic modulus, and hardness data at contact depth of 15 nm for magnetic tape (adapted from Li and Bhushan 2002a)

including gold (Au), graphene, iron oxide, polymer, and silica have been studied in targeted drug delivery for cancer treatment (Maharaj and Bhushan 2015; Bhushan 2017).

In tribological applications, nano-objects come into sliding contact with each other and the surfaces in which they are used. Contacts may occur locally on a nano-object or the entire nano-object may be compressed. To simulate local deformation of nano-objects, they may be indented with a sharp indenter. For global deformation, the entire nano-object is compressed (Maharaj and Bhushan 2015).

Mechanical properties of nano-objects can be measured by using either a sharp nanoindenter tip to measure local deformation or a flat punch to measure global deformation (Fig. 5.38). Figure 5.39 shows TEM images of spherical gold nanoparticles (NPs) approximately 50 nm in diameter and gold nanorods (NRs) 50 nm in

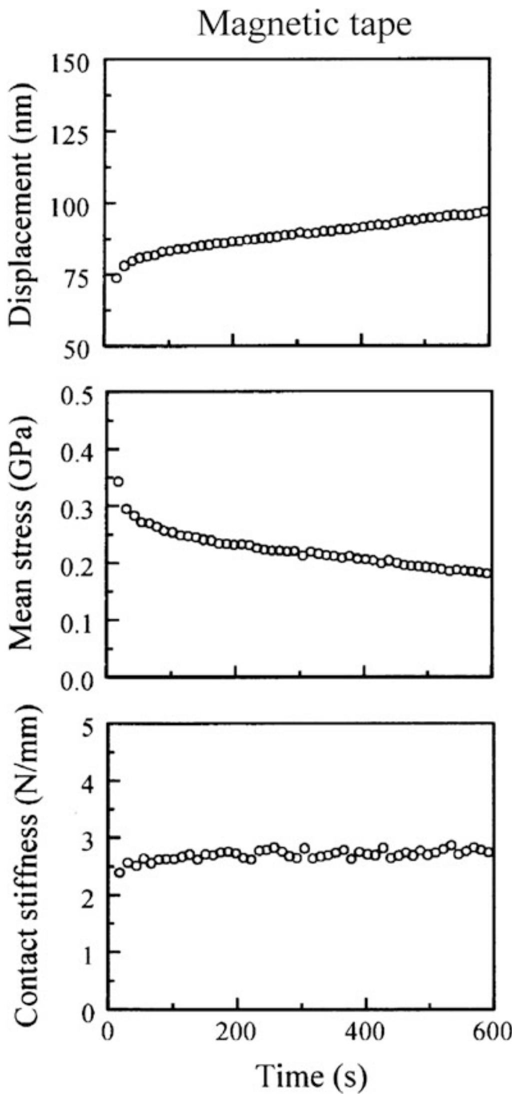

Fig. 5.37 Indentation displacement, mean stress, and contact stiffness as a function of time for magnetic tape (adapted from Li and Bhushan 2002a)

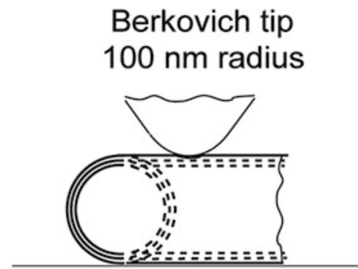

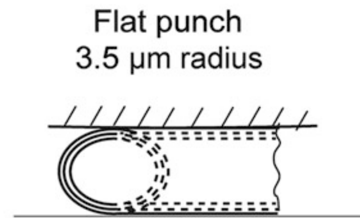

Fig. 5.38 Schematics of nanoindentation using a sharp tip to measure local deformation and compression using a flat punch to measure global deformation of nano-objects (adapted from Maharaj and Bhushan 2015)

diameter and 200 nm in length for which nanoindentation data will be presented next (Maharaj and Bhushan 2015). Figure 5.40a shows a typical load-displacement curve for gold particles with approximately 500 nm in diameter. Pop-in events occur during nanoindentation and are shown by vertical arrows on the load-displacement curves. Pop-in events correspond to generation of new dislocations and multiplication of existing dislocations.

Figure 5.40b shows nanoindentation hardness and elastic modulus as a function of contact depth. Scale effects in nanohardness can be observed.

Figure 5.41a shows typical load-displacement curves at a maximum load of 50 μN with gold NPs and NRs with approximately 50 nm in diameter using a flat punch to study global deformation. To study recovery from deformation after the compression experiments, Fig. 5.41b shows the topography maps and 2-D profiles after 1 and 4 min of compression experiments. Two profiles were examined to observe whether there was recovery from the deformation. These profiles are essentially the same and suggest no recovery.

Micro/nanopillar structures represent a geometry of nanomaterials that can be used as components for various MEMS/NEMS devices (Palacio and Bhushan 2013; Bhushan 2017).

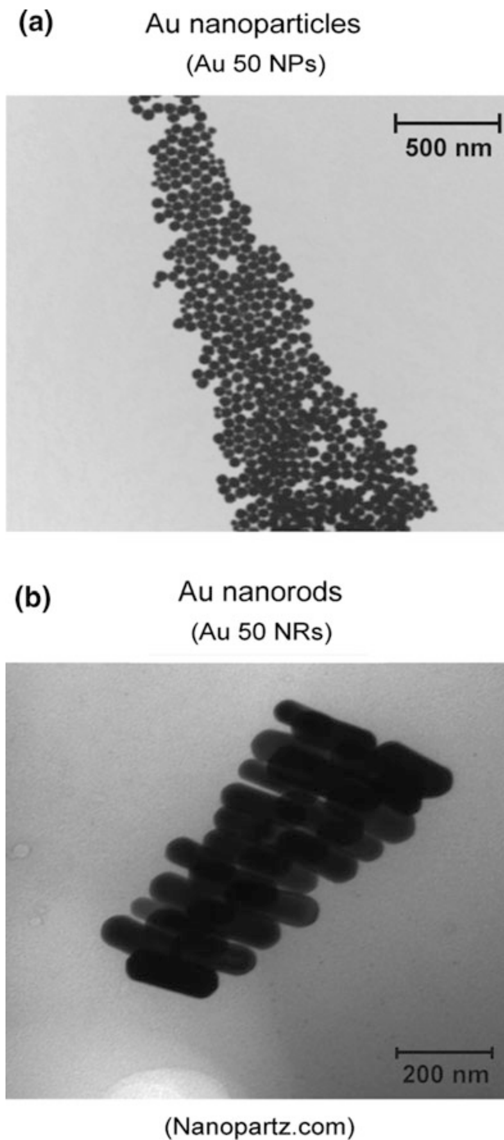

Fig. 5.39 TEM images of **a** spherical Au nanoparticles approximately 50 nm in diameter (Au 50 NPs) **b** Au nanorods 50 nm in diameter and 200 nm in length (Au 50 NRs) (adapted from Maharaj and Bhushan 2015)

Since submicron-sized pillar structures can be produced with well-defined geometries, they are used commonly to study scale effects on mechanical properties. Similar to nanoparticles, these structures have very small material volumes. As a result, the mechanical deformation of micro/nanopillars differs from their bulk counterparts.

These pillars are produced by various fabrication techniques including focused ion beam (FIB) micromachining. For deformation studies, these are loaded generally in compression using a flat punch. As an example, San Juan et al. (2009) performed compression studies on metal superalloy pillars composed of Cu–Al–Ni and with a diameter of 900 nm fabricated by FIB micromachining. Shape memory alloys are of scientific and technological interest as they can transform between the austenite phase and the martensite phase reversibly. The submicron diameter pillar such as the one shown in Fig. 5.42a was subjected to cyclic compression using a diamond sphero-conical tip. Two load-displacement curves taken after ten compression cycles are shown in Fig. 5.42b. At a load of about 95 μN, an abrupt burst in displacement is observed as a result of the stress-induced martensitic transformation. During unloading, the reverse transformation is observed at about 45 μN load, and continues gradually until a load of about 22 μN is attained. The compression is completely elastic, as no residual deformation was observed. In this study, a size effect was observed such that the martensite phase has improved stability relative to its bulk form due to relaxation effects at the free surface. As a consequence, the reverse transformation takes place only when very low values of the stress are attained during the unloading. This is manifested by the large hysteresis seen in the load-displacement curve prior to elastic recovery.

5.4 Nanoscratch Technique for Adhesion Measurement and Nanoscratch/Nanowear Resistance

The nanoscratch technique is used commonly to measure relative adhesion strength of coated surfaces and to measure nanoscratch/nanowear resistance.

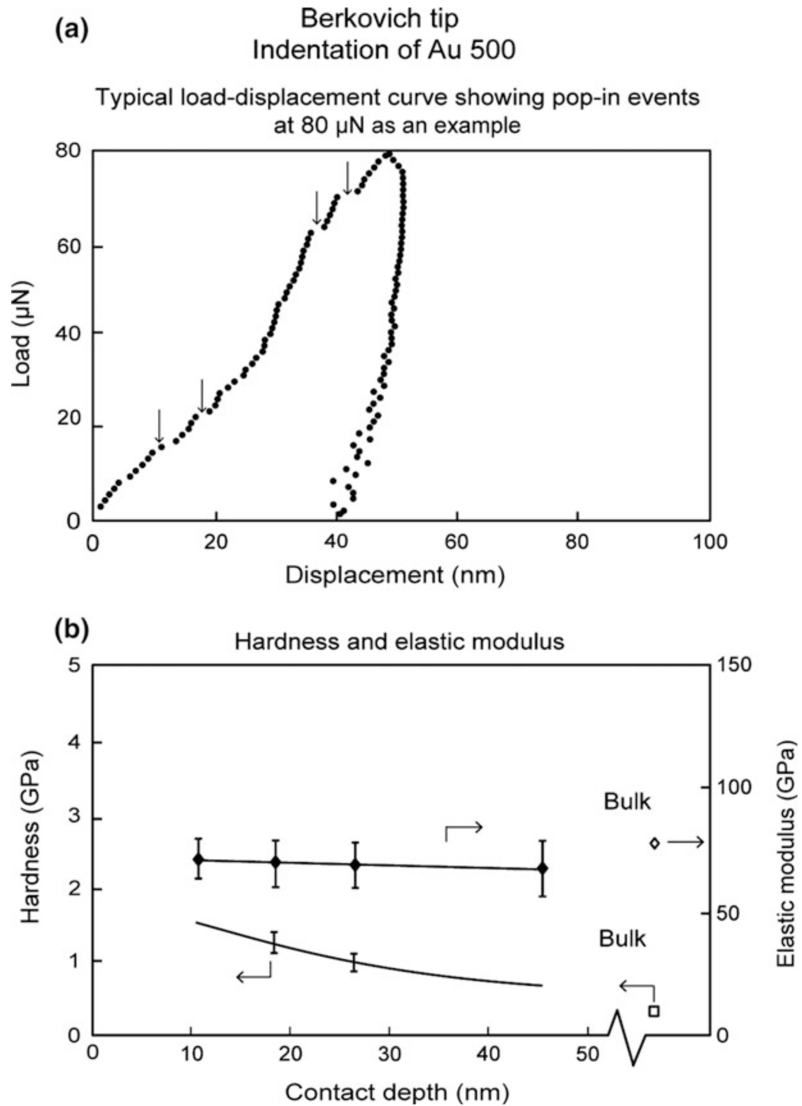

Fig. 5.40 **a** Typical load-displacement indentation curve of nanoparticles with 500 nm in diameter (Au 500 NPs) at a maximum load of 80 μN with *vertical arrows* showing pop-in events, and **b** hardness and elastic modulus of Au 500 NPs as a function of contact depth represented by *bold square* and *diamond datum* points respectively with corresponding *open diamond* and *square datum* points representing bulk data (adapted from Maharaj and Bhushan 2015)

5.4.1 Adhesion Strength

Scratching a surface with a fingernail or a knife is probably one of the oldest methods for determining the adhesion of paints and other coatings. In 1822, Friedrich Mohs used resistance to scratch as a measure of hardness. Scratch tests to measure adhesion of films was introduced first by Heavens in 1950. A smoothly round, chrome-steel stylus with a tungsten carbide or Rockwell C diamond tip (in the form of 120° cone with a hemispherical tip of 200 μm radius) (Perry 1983; Mehrotra and Quinto 1985; Valli 1986) or Vickers pyramidal indenter (Burnett and Rickerby 1987a; Bull and Rickerby 1990; Venkataraman et al. 1992) for macro- and microscratching a conical diamond indenter (with 1 or 5 μm of tip radius and 60° of included angle) for nanoscratching (Wu 1991; Bhushan et al. 1995) is drawn across the coating surface. A normal load is applied to the scratch tip and is gradually increased during scratching until the coating is completely removed. The minimum or critical load at which the coating is detached or completely removed is used as a measure of adhesion (Benjamin and Weaver 1960; Campbell

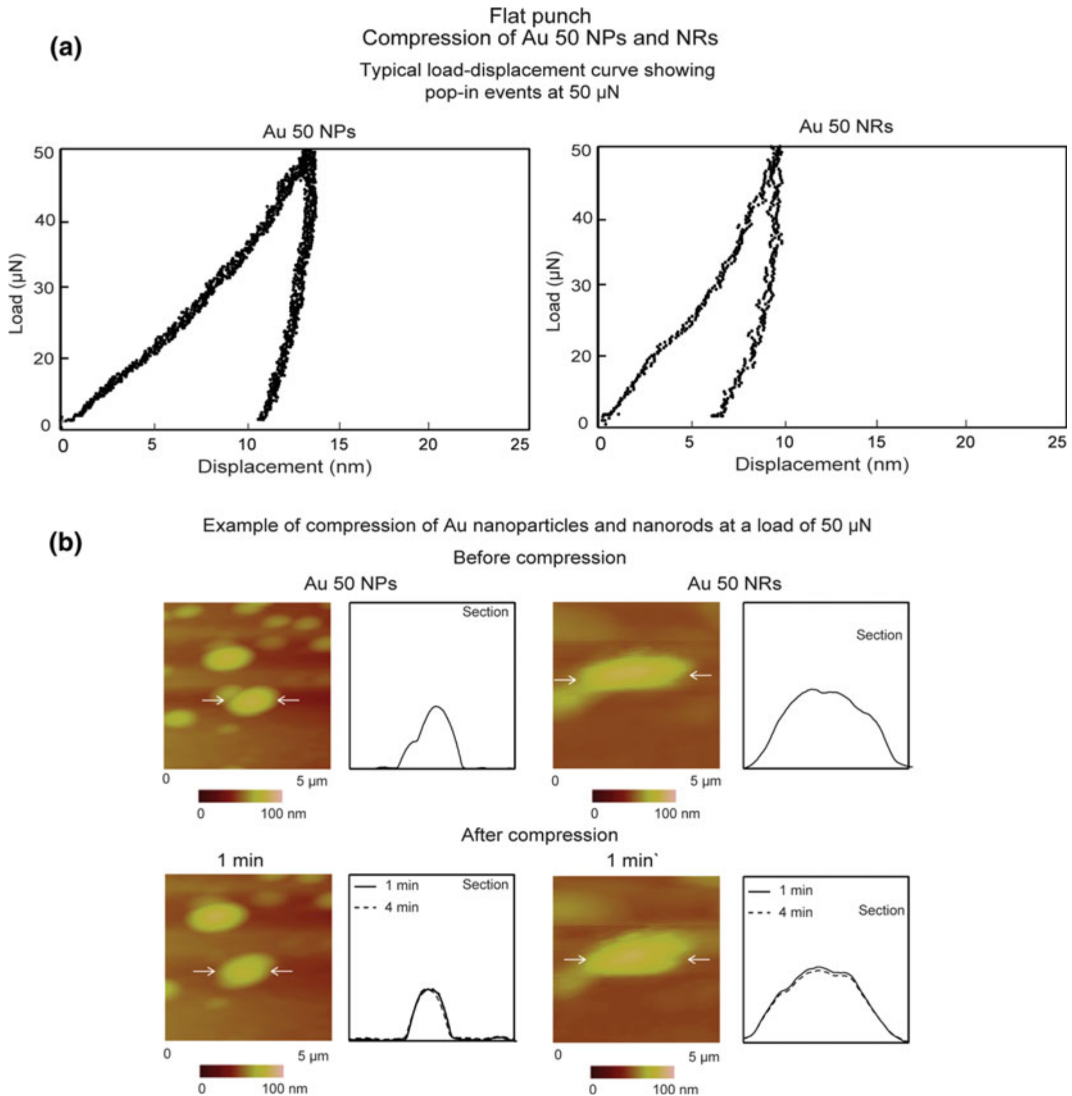

Fig. 5.41 **a** Typical load-displacement curve at a maximum load of 50 μN with Au nanoparticles with 50 nm in diameter (Au 50 NPs) and Au nanorods with 50 nm in diameter (Au 50 NRs) using a flat punch, and **b** topography maps and 2-D profiles at sections shown by the horizontal arrows before compression (*first row*) and after compression (*second row*). The *second row* shows topography maps 1 min. after compression and the *solid lines* and *dashed lines* show the 2-D profiles after 1 and 4 min respectively. The *horizontal white arrows* indicate the nano-objects of interest along with the section on which the profiles were taken (adapted from Maharaj and Bhushan 2015)

1970; Greene et al. 1974; Ahn et al. 1978; Mittal 1978; Laugier 1981; Mehrotra and Quinto 1985; Valli 1986; Burnett and Rickerby 1987a; Sekler et al. 1988; Wu 1991; Bull and Rickerby 1990; Bhushan et al. 1995; Gupta and Bhushan 1995a, b; Patton and Bhushan 1996; Bhushan and Li 1997; Li and Bhushan 1999a, b, c). It is a most commonly used technique to measure adhesion of hard coatings with strong interfacial adhesion (>70 MPa).

For a scratch geometry produced using a stylus with a spherical tip, shown in Fig. 5.43, surface hardness H is given by

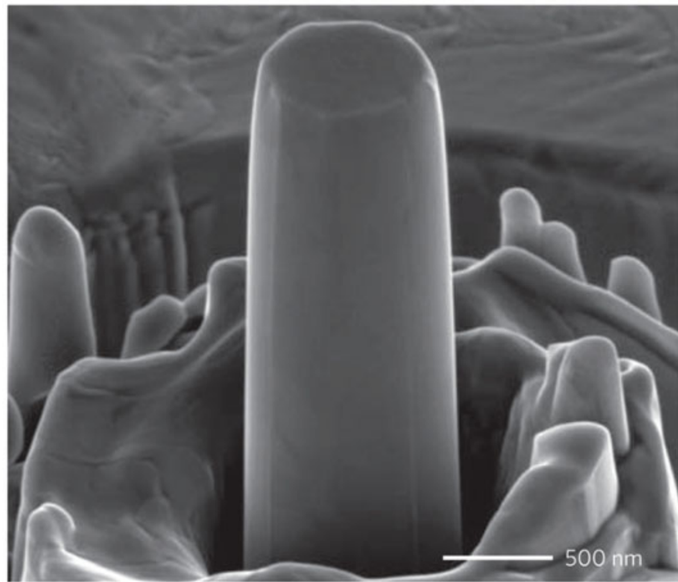

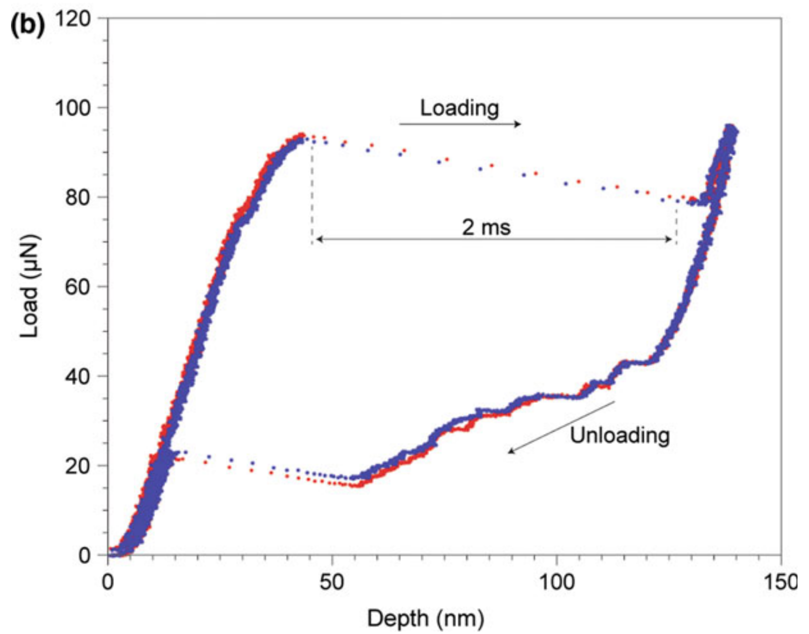

Fig. 5.42 **a** SEM image of a 900-nm diameter pillar composed of Cu–Al–Ni alloy, and **b** load-displacement curves from two consecutive nanocompression experiments (adapted from San Juan et al. 2009)

$$H = \frac{W_{cr}}{\pi a^2} \tag{5.21}$$

and adhesion strength τ is given by (Benjamin and Weaver 1960)

$$\tau = H \tan\theta \tag{5.22a}$$

$$= \frac{W_{cr}}{\pi a^2}\left[\frac{a}{\left(R^2 - a^2\right)^{1/2}}\right]$$

or

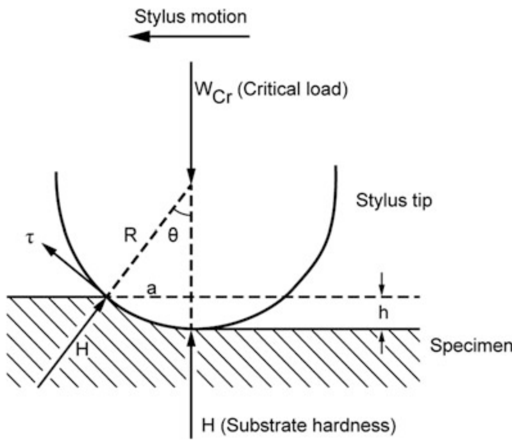

Fig. 5.43 Geometry of a scratch produced using a stylus with a spherical tip

$$\tau = \frac{W_{cr}}{\pi a R} \text{if R} \gg \text{a} \qquad (5.22\text{b})$$

where W_{cr} is the critical normal load, a is the contact radius, and R is the stylus radius.

Burnett and Rickerby (1987a) and Bull and Rickerby (1990) analyzed the scratch test of a coated sample in terms of three contributions: (1) a plowing contribution, which will depend on the indentation stress field and the effective flow stress in the surface region, (2) an adhesive friction contribution due to interactions at the indenter-sample interface, and (3) an internal stress contribution, since any internal stress will oppose the passage of the indenter through the surface, thereby effectively modifying the surface flow stress. They derived a relationship between the critical normal load W_{cr} and the work of adhesion W_{ad}

$$W_{cr} = \frac{\pi a^2}{2}\left(\frac{2EW_{ad}}{t}\right)^{1/2} \qquad (5.23)$$

where E is the elastic modulus and t is the coating thickness. Plotting of W_{cr} as a function of $a^2/t^{1/2}$ should give a straight line of the slope $\pi(2EW_{ad})^{1/2}/2$ from which W_{ad} can be calculated. Bull and Rickerby suggested that either the line slope (interface toughness) or W_{ad} could be used as a measure of adhesion.

An accurate determination of critical load W_{cr} sometimes is difficult. Several techniques have been used to obtain the critical load including (1) microscopic observation (optical or SEM) during the test, (2) chemical analysis of the bottom of the scratch channel (with electron microprobes) and (3) acoustic emission (Perry 1983; Valli 1986; Sekler et al. 1988; Wu 1991). In some instruments, tangential (or friction) force is measured during scratching to obtain the critical load (Jacobson et al. 1983; Valli 1986; Wu 1991; Bhushan et al. 1995, 1997; Bhushan and Li 1997; Gupta and Bhushan 1995a, b; Patton and Bhushan 1996; Li and Bhushan 1998b, 1999a, b, c). The AE and friction force techniques have been reported to be very sensitive in determining critical load. AE and friction force start to increase as soon as cracks begin to form perpendicular to the direction of the moving stylus.

5.4.2 Nanoscratch/Nanowear Resistance

In a nanoscratch test during scratching, normal load applied to the scratch tip is increased gradually until the material is damaged. Friction force generally is measured during the scratch test (Bhushan and Gupta 1995; Bhushan et al. 1996b; Palacio and Bhushan 2010; Kumar and Bhushan 2015; Cho and Bhushan 2016). After the scratch test, the morphology of the scratch region including debris is observed in an SEM. Based on the combination of the changes in the friction force as a function of normal load and SEM observations, the critical load is determined and the deformation mode is identified. Any damage to the material surface as a result of scratching at a critical ramp-up load results in an abrupt or gradual increase in friction.

Deformation modes can be identified by microscopic examination of scratch marks. The material may deform either by plastic deformation or fracture. Ductile materials (all metals) deform primarily by plastic deformation, resulting in significant plowing during scratching. The

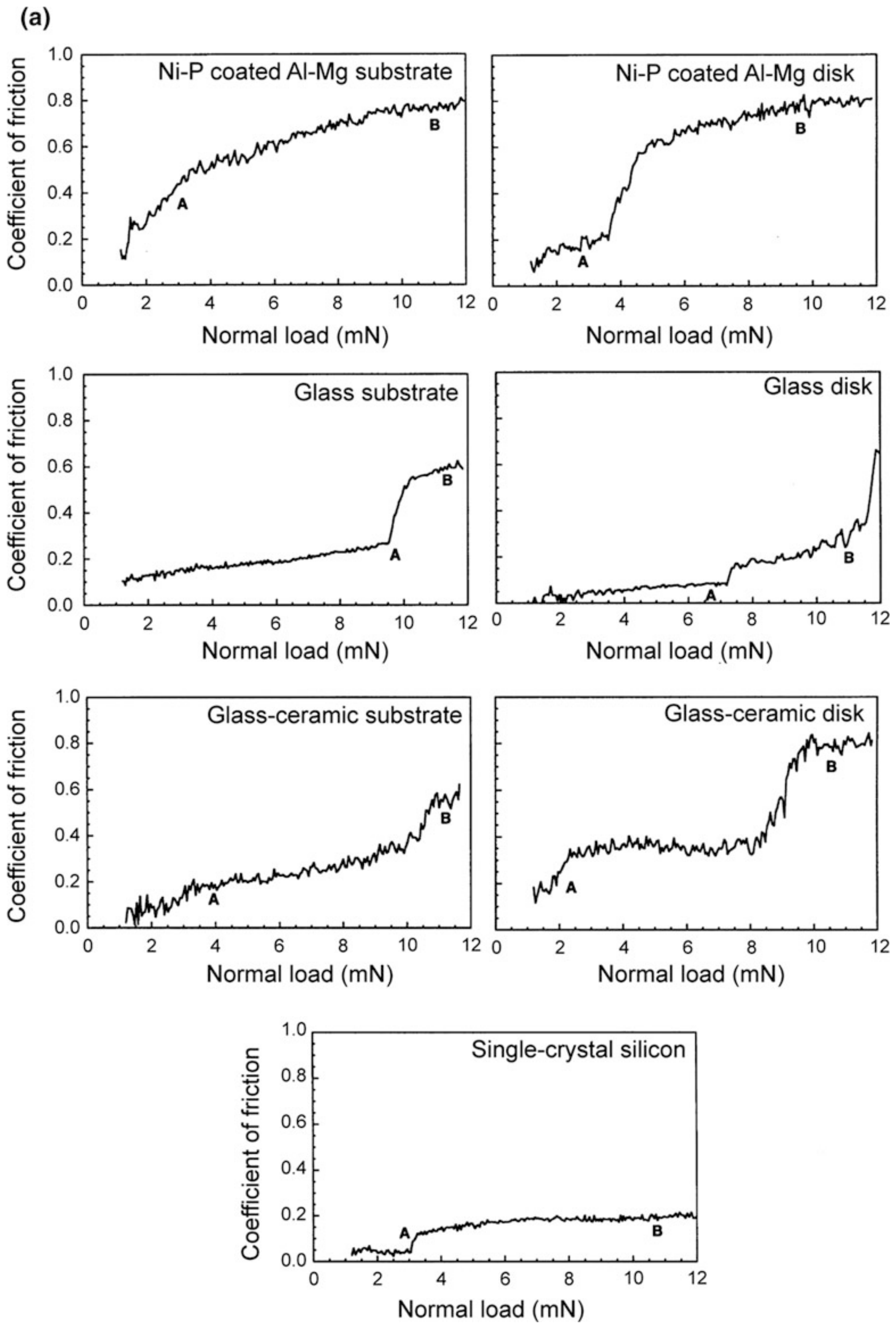
(a)
Ni-P coated Al-Mg substrate
Ni-P coated Al-Mg disk
Glass substrate
Glass disk
Glass-ceramic substrate
Glass-ceramic disk
Single-crystal silicon
Coefficient of friction
Normal load (mN)
A
B
0.0
0.2
0.4
0.6
0.8
1.0
0
2
4
6
8
10
12

Fig. 5.44 **a** Coefficient of friction profiles as a function of normal load for 500-μm long scratches made using a diamond tip with 1-μm tip radius, at a normal load ranging from 1 to 12 mN on Ni–P coated Al–Mg substrate and various ceramic substrates, as well as corresponding magnetic disks, and single-crystal silicon, and **b** SEM images of two regions on 500-μm long scratches made at 1–12 mN load on various ceramic substrates and corresponding magnetic disks and single-crystal silicon. The scratching direction was from *left* to *right*. The *upper images* in the sets of two images for each sample correspond to a location or normal load where the friction increased abruptly and/or damage began to occur. These are the points indicated by 'A.' The *lower images* correspond to a location close to the end of the scratch (~11 mN). These are the points indicated by 'B' (adapted from Bhushan and Gupta 1995)

width and depth of the tracks produced increase with an increase in the normal load. Plowing results in a continuous increase in the coefficient of friction with an increase in the normal load during scratching and produces generally ribbon-like or curly debris. To compare, brittle materials deform primarily by brittle fracture with some plastic deformation. In the brittle fracture mode, the coefficient of friction increases very little until a critical load is reached at which the material fails catastrophically and produces fine debris, which is rounded, and the coefficient of friction increases rapidly above the critical load.

The profiles for the coefficient of friction as a function of normal load for scratches made on Ni–P coated Al–Mg substrate and various ceramic substrates, as well as corresponding magnetic disks (substrates coated with 75-nm-thick sputtered Co–Pt–Ni magnetic film and 20-nm thick sputtered DLC film) are compared in Fig. 5.44a (Bhushan and Gupta 1995). The figure also includes the friction force profile for a single-crystal silicon substrate for comparison. The SEM images of two regions of 500-μm-long scratches made at 1–12 mN normal load on various samples are compared in Fig. 5.44b (Bhushan and Gupta 1995). The upper images in the sets of two images for each sample correspond to a region where friction increased abruptly. These are the points indicated by "A" in Fig. 5.44b. The lower images in each set correspond to the region that is very close to the end of a scratch. These are the points indicated by "B". The extent of a damage in a scratch is estimated by the width and depth of the scratch and by the amount of debris generated toward the end of the scratch.

Single-crystal silicon exhibited the lowest friction with little plowing at a low load and cracking at higher loads. This observation suggests that scratching of the silicon took place primarily by brittle deformation. In the case of the Ni–P-coated Al–Mg substrate, friction increase was continuous from the beginning of the scratching, Fig. 5.44a. SEM images of the Ni–P-coated Al–Mg substrate presented in Fig. 5.44b, show the material removal occurred by plowing with formation of curly ductile chips. It is evident that scratching took place primarily by plastic deformation typical of ductile materials. Plowing is responsible for the continuous increase in the friction for this substrate. Glass and glass-ceramic substrates and corresponding disks and the Ni–P coated Al–Mg disk exhibited relatively low friction with a sudden increase at higher load. The glass substrate exhibited the lowest friction, followed by the glass-ceramic substrate. In the case of the Ni–P coated Al–Mg disk, the load at which friction increased was lower than that of the glass and glass-ceramic substrates. SEM images of these samples exhibit plowing in addition to the formation of fine debris. There is no evidence of cracking of ceramic substrates or the ceramic overcoats used in all disks at magnifications as high as 50,000×. Glass is chemically strengthened in order to produce significant compressive stresses in the glass surface. Glass-ceramic consists of fine-grained polycrystalline material in a glass matrix. The chemical strengthening and the crystals add to the fracture toughness of the material. Thus, both ceramic substrate materials are expected to deform with ductile and brittle deformation modes. Ductile deformation results in plowing, whereas brittle deformation aids in debris generation. Lower values of the coefficient of friction before a sudden increase, as compared to the Ni–P-coated Al–Mg substrate, suggest that brittle fracture contributes to overall deformation.

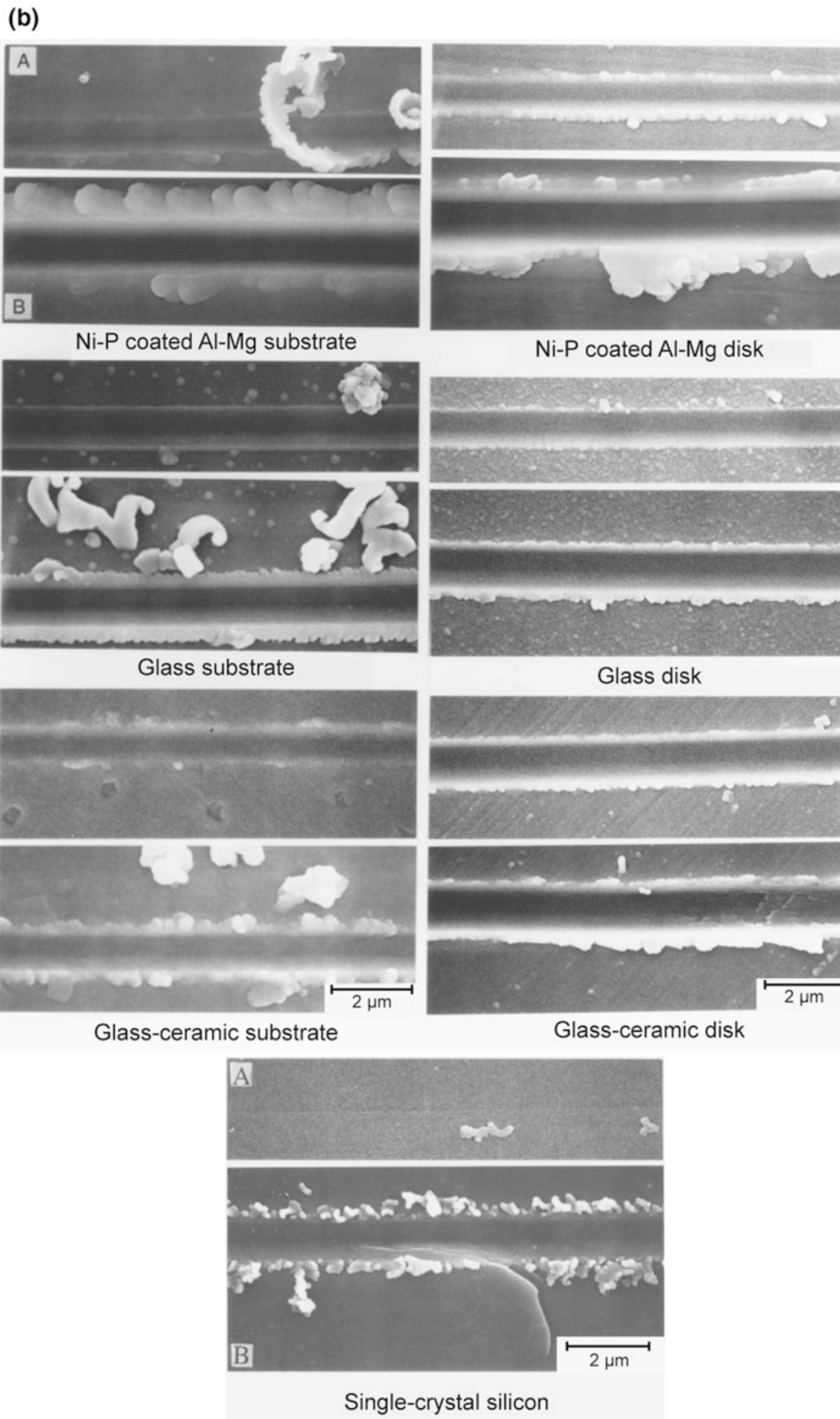

Fig. 5.44 (continued)

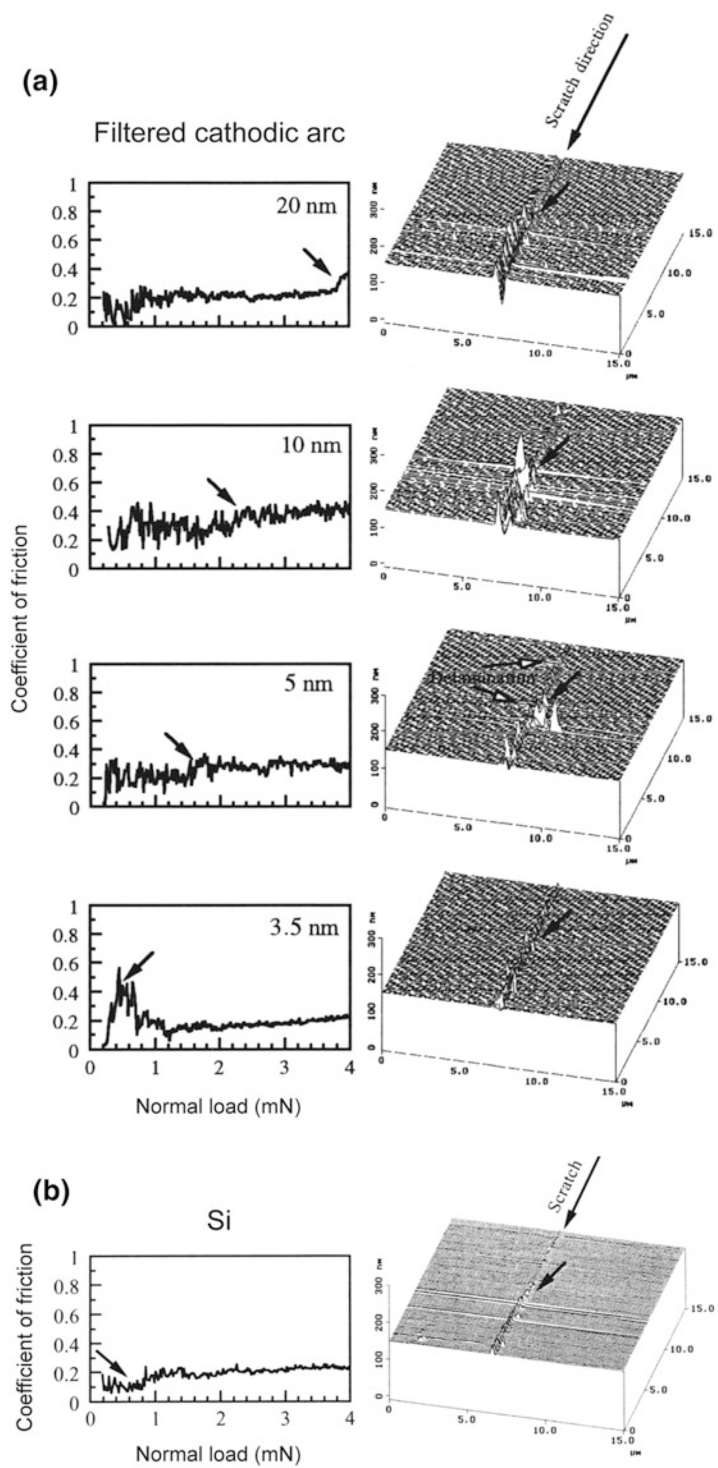

Fig. 5.45 Coefficient of friction profiles as a function of increasing normal load, three dimensional AFM images of regions over scratches at the respective critical loads (indicated by the *arrows* in the friction profiles and AFM images), made on the filtered cathodic arc deposited DLC coating of different thicknesses and an uncoated Si substrate (adapted from Li and Bhushan 1999a)

Hard overcoats generally consist of significant compressive residual stresses. It is these compressive stresses that allow ductile deformation with little cracking. We further note that a sudden increase in the coefficient of friction for ceramic substrates and for all disks at some load results from significant damage to the bulk material or to the coating surface (Fig. 5.44b).

Based on the friction data, the width and depth of scratches, the amount of debris generated, and scratch morphology, glass substrates and corresponding disks exhibit a lower coefficient of friction against a diamond tip and a superior resistance to scratch, followed by glass-ceramic substrates and corresponding disks. This example clearly suggests that deformation modes and critical load to failure can be identified using the scratch technique. The critical load to failure is a measure of scratch/wear resistance and adhesion in the case of coated surfaces.

Bhushan et al. (1995, 1997), Bhushan and Li (1997), Gupta and Bhushan (1995a, b), Patton and Bhushan (1996), and Li and Bhushan (1998b, 1999a, b, c) have used the scratch technique to study adhesion and scratch/wear resistance (a measure of mechanical durability) of various ceramic films. Scratch tests conducted with a sharp diamond tip simulate a sharp asperity contact. Bhushan and coworkers have also conducted accelerated friction and wear (ball-on-coated disk) and functional tests and have found a good correlation between the scratch resistance and wear resistance measured using accelerated tests (Bhushan et al. 1995, 1997; Gupta and Bhushan 1995b; Patton and Bhushan 1996; Li and Bhushan 1998b, 1999a, b) and functional tests (Patton and Bhushan 1996; Bhushan and Patton 1996; Bhushan et al. 1997). Based on this work, scratch tests can be successfully used to screen materials and coatings for wear applications.

Li and Bhushan (1999a) conducted scratch tests on ultrathin DLC coatings of thicknesses ranging from 20 down to 3.5 nm deposited by FCA technique on Si(100) substrates. Figure 5.45 shows the profiles of the coefficient of friction as a function of increasing normal load,

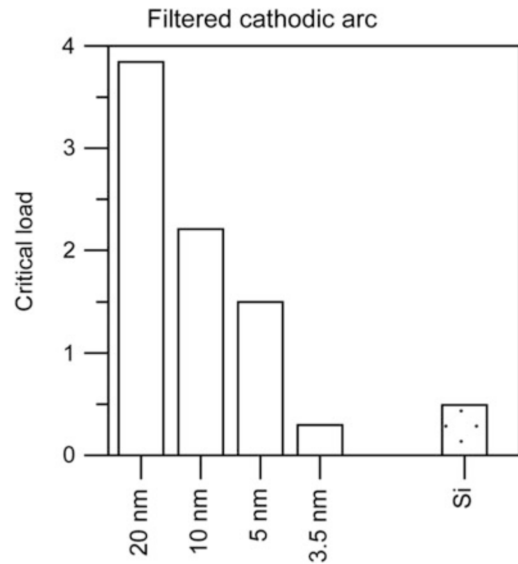

Fig. 5.46 Critical loads estimated from the friction profiles and AFM images for the filtered cathodic arc deposited DLC coatings of different thicknesses and an uncoated Si substrate (adapted from Li and Bhushan 1999a)

three-dimensional line AFM images of regions over scratches at the respective critical loads (indicated by the arrows in the friction profiles and AFM images) made on coatings of different thicknesses, and an uncoated Si substrate. From the AFM images, the debris can be seen easily, and the appearance of the first debris is indicated by the arrows, which correspond to critical loads. A well-defined critical load is observed for each coating. The AFM images clearly show that below the critical loads, the coatings were plowed by the scratch tip, associated with the plastic flow of materials. At and after the critical loads, debris (chips) or buckling were observed on the sides of scratches. Delamination or buckling can be observed around or after the critical loads. This suggests that the damage of these coatings starts from delamination and buckling. For the 3.5 and 5 nm thick FCA coatings before the critical loads, small debris is observed on the sides of scratches. This suggests that the thinner FCA coatings may be more brittle and more easily broken. Also, the 3.5 and 5 nm thick FCA coatings show more delamination and buckling

events than the other coatings. This indicates that the thinner FCA coatings have higher interfacial and residual stresses than the other coatings. The critical loads increase with increasing coating thickness. This indicates that the critical load is determined not only by the adhesive strength to the substrate but also by the coating thickness. It can be seen that the uncoated Si substrate exhibits a lower coefficient of friction of about 0.1 before the critical load. The AFM image shows that the uncoated Si substrate was damaged by plowing, associated with the plastic flow of materials. At and after the critical load, small and uniform debris is observed, and the amount of debris increases with increasing normal load.

The critical loads estimated from the friction profiles and AFM images for coatings of different thicknesses and an uncoated Si substrate are compared in Fig. 5.46. The thicker the coating, the higher the critical load. At 3.5 nm, the critical loads drop to about 0.4 mN, which is about the same critical load of the uncoated Si substrate.

The optical images of wear tracks and debris formed on all samples when slid against a 3-mm diameter sapphire ball after sliding distance of 5 m are compared in Fig. 5.47. The normal load used for the 20 and 10 nm thick coatings was 200 mN and the normal load used for the 5 and 3.5 nm thick coatings and Si substrate was 150 mN. No wear track and debris were found on the 20 nm thick coating. The low wear resistance of the 5 nm thick FCA coating is in good agreement with the low scratch critical load, which may be due to the higher interfacial and residual stresses as well as brittleness of the coating. At 3.5 nm, the FCA coating provides no wear resistance, failing instantly like the uncoated Si substrate. Large block-like debris is observed on the sides of the wear track of the coating. This indicates that large region delamination and buckling occurred during sliding, resulting in large block-like debris.

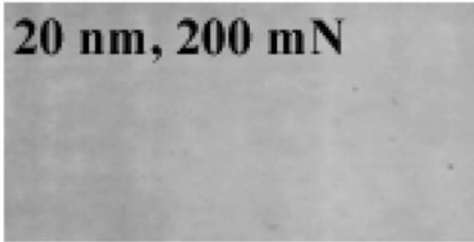

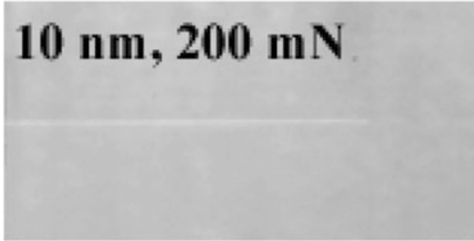

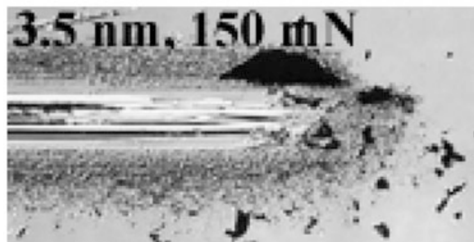

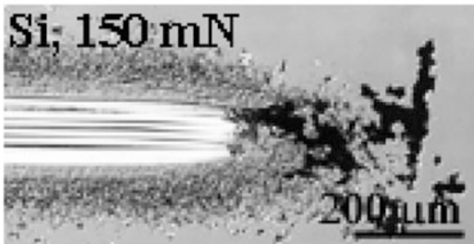

Fig. 5.47 Optical images of wear tracks and debris formed on all filtered cathodic arc deposited coatings of different thicknesses and an uncoated Si substrate when slid against a sapphire ball after sliding distance of 5 m (adapted from Li and Bhushan 1999a)

This example clearly suggests that scratch resistance is a powerful way of screening materials and the data correlates well with the wear performance (Li and Bhushan 1999a).

5.5 Nanoindentation for Adhesion Strength and Residual Stress Measurements of Thin Films

Adhesion describes the sticking together of two materials. Adhesion strength, in a practical sense, is the stress required to remove a coating from a substrate. Indentation and scratch (described earlier) on the micro- and nanoscales are the two commonly-used techniques to measure adhesion of thin hard films with good adhesion to the substrate (>70 MPa) (Campbell 1970; Mittal 1978; Blau and Lawn 1986; Bhushan 1987; Bhushan and Gupta 1997; Bhushan 1999a; Bhushan and Li 2003).

Nearly all coatings, by whatever means they are produced, and surface layers of treated parts are found to be in a state of residual (intrinsic or internal) stress. These are elastic stresses that exist in the absence of external forces and are produced through the differential action of plastic flow, thermal contraction, and/or changes in volume created by phase transformation. Microindentation and nanoindentation techniques are also used to measure residual stresses (Bhushan and Gupta 1997).

In this section, we describe adhesion strength measurements and residual stress measurements using nanoindentation.

5.5.1 Adhesion Strength Measurements

In the indentation test method at low loads, the coating deforms with the substrate. However, if the load is sufficiently high, a lateral crack is initiated and propagated along the coating-substrate interface. The lateral crack length increases with the indention load. The minimum load at which the coating fracture is observed is called the *critical load* and is used as the measure of coating adhesion (Fig. 5.48) (Bhushan 1999a; Bhushan and Li 2003). For relatively thick films, the indentation is generally made using a Brinell hardness tester with a diamond sphere of 20 μm radius (Tangena and Hurkx 1986), Rockwell hardness tester with a Rockwell C 120° cone with a tip radius of 200 μm (Mehrotra and Quinto 1985) or a Vickers pyramidal indenter (Chiang et al. 1981; Lin et al. 1990; Alba et al. 1993). However, for extremely thin films, a Berkovich indenter (Stone et al. 1988) or a conical diamond indenter with a tip radius of 5 μm and 30° of included angle (Bhushan et al. 1995) is used in a nanoindenter.

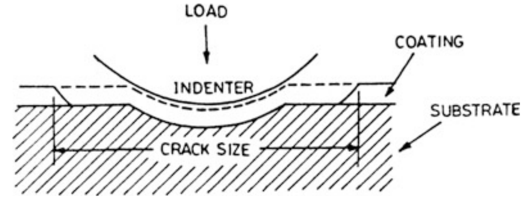

Fig. 5.48 Schematic illustration of the indentation method for adhesion measurement (adapted from Bhushan and Li 2003)

It should be noted that the measured critical load W_{cr} is a function of hardness and fracture toughness, in addition to the adhesion of coatings. Chiang et al. (1981) have related the measured crack length during indentation, the applied load, and the critical load (at which coating fracture is observed) to the fracture toughness of the substrate-coating interface. A semi-analytical relationship derived between the measured crack length c and the applied load W,

$$c = \alpha\left(1 - \frac{W_{cr}}{W}\right)^{1/2} W^{1/4} \tag{5.24}$$

where $\alpha^2 = \frac{\alpha_1 t_c^{3/2} H^{1/2}}{(K_{Ic})_{interface}}$,$\alpha_1$ is a numerical constant, t_c is the coating thickness, H is the mean hardness, and $(K_{\mathrm{Ic}})_{\mathrm{interface}}$ is the fracture toughness of the substrate-coating interface. Mehrotra and Quinto (1985) used this analysis to calculate fracture toughness of the interface.

Bhushan (1987) estimated adhesion of composites by measuring the magnitude of shear

(friction) stresses at fiber/matrix interfaces in composites. Marshall and Oliver (1987) used a Berkovich indenter to push on the end of an individual fiber, and measured the resulting displacement of the surface of the fiber below the matrix surface (due to sliding). The shear stress was calculated from the force-displacement relation obtained by analysis of the frictional sliding. The force and displacement measurements were obtained only at the peak of the load cycle, and the sliding analysis was based on sliding at constant shear resistance at the interface. These experiments provided measurements of average shear stresses at individual fibers.

5.5.2 Residual Stress Measurements

Indentation measurements, similar to those used to determine the hardness and elastic modulus of a film, can be used to measure the residual stresses in it, also (Bhushan 1999a; Bhushan and Li 2003). When a compressive force on a biaxially stressed film during indentation is applied in a direction perpendicular to the film, yielding will occur at a smaller applied compressive force while a film is stressed in biaxial tension as compared with the unstressed film. Thus, the biaxial tension decreases hardness and the biaxial compression increases hardness (Swain et al. 1977; Vitovec 1986). LaFontaine et al. (1991) used the nanoindentation technique to measure the effect of residual stresses on the hardness of thin films. For samples that do not undergo large structural changes, changes in hardness with time reflect a change in residual stress in the film (LaFontaine et al. 1991). Bolshakov et al. (1996) and Tsui et al. (1996) studied the effect of residual stresses on hardness and elastic modulus. Based on indentation measurements and finite element analysis of the indentation process, they reported that, once pile up is accounted for, the residual stresses have little effect on hardness and elastic modulus.

Tsukamoto et al. (1987) measured the deflection at the center of the bent beam (bent as a result of residual stresses in the film) by pressing the beam flat with a nanoindenter. The bent beam is placed on a flat glass surface supported by two fulcrums, and a load-deflection curve is generated (Fig. 5.49). The distance h_a can be estimated from the inflection point in the curve. Because of the limited flatness of most substrates, the film is removed from the substrate, then the initial deflection is measured. The true deflection resulting from residual stresses in the film equal to $h_a - h_b$. The curvature ($1/R$) of the substrate can then be calculated by the geometric relationship,

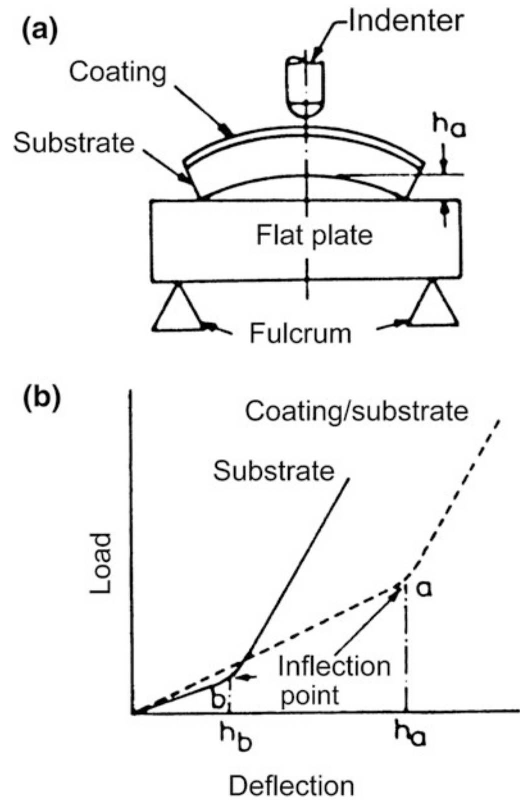

Fig. 5.49 **a** Schematic diagram of the deflection measurement of a bent beam using a nanoindenter, and **b** load-deflection curve for a warped composite-beam substrate

$$R = \frac{L^2}{8(h_a - h_b)} \tag{5.25}$$

where L is the span.

Hong et al. (1990) used another deflection measurement technique. In this technique, a circular section of the substrate is removed from

beneath the film to produce a drumhead-like membrane and the load is applied at its center. The stiffness of the membrane (film) is a sensitive function of the biaxial tension in it. The deflection h is related to load W as

$$h = \frac{Wa^2}{16\pi D} g(k) \tag{5.26}$$

where

$$D = \frac{Et^3}{12(1 - v^2)}$$

where a is the radius of the membrane, t is its thickness, and the function $g(k)$ depends on the membrane and its geometry. If the geometry and elastic constants of the membrane are known, the tension can be accurately evaluated. This technique can only be used to study tensile residual stresses since compressive stresses buckle the membrane when the substrate is removed.

5.6 Nanoindentation Techniques for Nanofracture Toughness and Nanofatuge

Nanoindentation techniques have been used for measurement of nanofracture toughness and nanofatigue (Bhushan 1999a; Bhushan and Li 2003).

5.6.1 Nanofracture Toughness

Fracture toughness, K_{Ic}, of a material is a measure of its resistance to the propagation of cracks and the ratio H/K_{Ic} is an index of brittleness, where H is the hardness (Bhushan 1999a; Bhushan and Li 2003). Resistance to fracture is a strong function of a crack pattern. It is measured typically in a tensile test in which a specimen containing a sharp crack of known length, c, is subjected to an applied stress, σ, which is increased during the test until the sample fractures (Lawn 1993), Fig. 5.50. The magnitude of the stresses near the crack tip are determined by

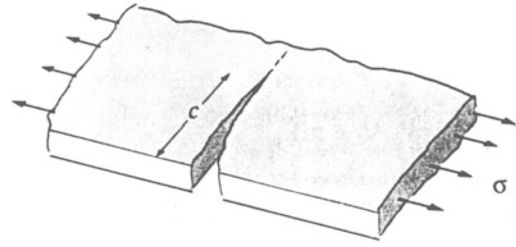

Fig. 5.50 Schematic of a standard specimen containing a sharp crack of known length used for measurement of fracture toughness of materials in tension

the stress intensity factor, K_I, which, in turn, depends on σ, c, and the specimen geometry

$$K_I = A\sigma\sqrt{\pi c} \tag{5.27}$$

The term A provides correction for the thickness-to-width ratio of the material. Units of stress-intensity factor are $MPa\sqrt{m}$. With more intense stress or with deeper cracks, the stress intensity becomes sufficient for the fracture to progress spontaneously. This threshold stress intensity is a property of the material and is called the critical stress intensity factor, K_{Ic}, or the fracture toughness of the material. Ceramics generally have relatively low fracture toughness, typically 1–2 $MPa\sqrt{m}$; consequently, it is an important property to be considered for the selection of ceramics for industrial applications.

Indentation fracture toughness is another technique to determine fracture toughness (Palmquist 1957; Lawn and Wilshaw 1975; Antis et al. 1981; Chiang et al. 1982; Henshall and Brookes 1985; Cook and Pharr 1990; Lawn 1993; Pharr et al. 1993; Bhushan et al. 1996b). The indentation cracking method especially is useful for measurement of fracture toughness of thin films or small volumes. This method is quite different from conventional methods in that no special specimen geometry is required. Rather, the method relies on the fact that when indented with a sharp indenter, most brittle materials form radial cracks (Fig. 5.51b). The lengths of the surface traces of the radial cracks (for definition of crack length, see Fig. 5.51a) have been found to correlate reasonably well with fracture toughness. Then, by using simple empirical

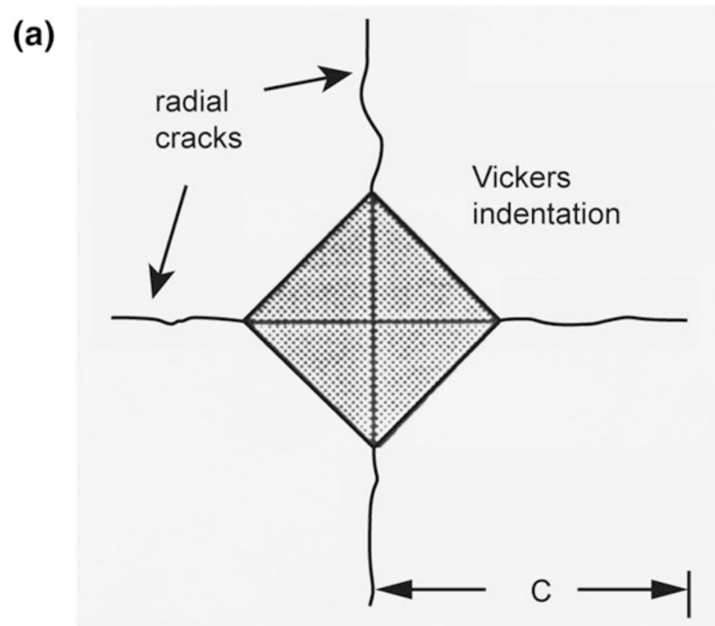

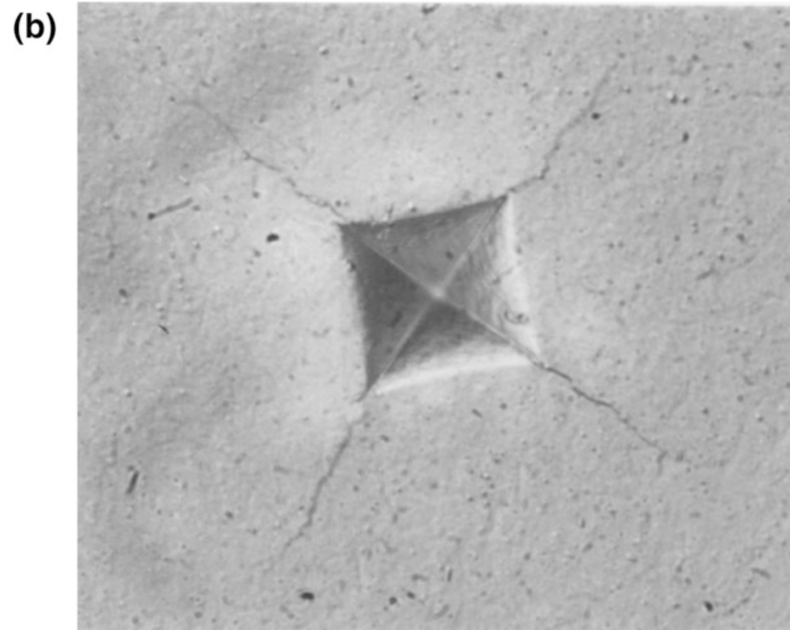

Fig. 5.51 **a** Schematic of Vickers indentation with radial cracks, and **b** optical images of Vickers indentation made on a glass-ceramic substrate at 500 g load (adapted from Bhushan et al. 1996b)

equations, fracture toughness can be determined from simple measurement of crack length. Although this indentation fracture toughness measurement technique has been widely used in practical applications, the stress/strain state is still, to a large extent, unknown. Stress/strain simulation on the indentation fracture with Vickers, Berkovich, and cube corner indenters is

needed for developing indentation fracture models and modifying the existing measurement methodology.

In microindentation, cracks at relatively high indentation loads of several hundred grams are on the order of 100 μm in length and can be measured optically. However, to measure toughness of very thin films or small volumes, much smaller indentations are required. However, a problem exists in extending the method to the nanoindentation regime in that there are well-defined loads, called cracking thresholds, below which indentation cracking does not occur in most brittle materials (Lankford 1981). For a Vickers indenter, cracking thresholds in most ceramics are about 25 g. Pharr et al. (1993), Li et al. (1997), and Li and Bhushan (1998a, 1999d) have found that the Berkovich indenter (a three-sided pyramid) with the same depth-to-area ratio as a Vickers indenter (a four-sided pyramid), has a cracking of the thresholds very similar to that of the Vickers indenter. They showed that cracking thresholds can be reduced substantially by using sharp indenters, i.e., indenters with smaller included tip angles such as a three-sided indenter with the geometry of the corner of a cube. Studies using a three-sided indenter with the geometry of the corner of a cube have revealed that cracking thresholds can be reduced to loads as small as 0.5 g, for which indentations and crack lengths in most materials are submicron in dimension.

Based on fracture mechanics analysis, Lawn et al. (1980) developed a mathematical relationship between fracture toughness and indentation crack length, given as

$$K_{Ic} = B\left(\frac{E}{H}\right)^{1/2}\left(\frac{W}{c^{3/2}}\right) \qquad (5.28)$$

where W is the applied load and B is an empirical constant depending upon the geometry of the indenter (also see Lawn 1993; Pharr et al. 1993). Antis et al. (1981) conducted a study on a number of brittle materials chosen to span a wide range of toughnesses. They indented with a Vickers indenter at several loads and measured crack length optically. They found a value of B = 0.016 to give good correlation between the toughness values measured from the crack length and the ones obtained using more conventional methods. Mehrotra and Quinto (1985) used a Vickers indenter to measure fracture toughness of the coatings. Bhushan et al. (1996b) measured fracture toughness of microcrystalline ceramic material (glass-ceramic) with Vickers indenter. They reported the formation of radial cracks, Fig. 5.51b. Note that cracks propagate in a zigzag manner. The interlocked crystal morphology is responsible for propagation in a zigzag manner. Using Eq. 5.28, the fracture toughness for this material is calculated and presented in Table 5.2.

Pharr et al. (1993) tested several bulk ceramics listed in Table 5.3 using a cube corner indenter. They used an empirical constant, B, of about 0.032 for a cube corner indenter. Indentation cracking thresholds can be reduced significantly by using a cube corner indenter, which is of interest for hard ceramic materials requiring high loads to initiate cracks. Pharr et al. (1993) reported that predominant cracks formed with Vickers or Berkovich indenters were cone cracks, and the predominant cracks with a cube corner indenter were radial cracks, Fig. 5.52. The data for various ceramics are presented in Table 5.3.

Chantikul et al. (1981) developed a relationship between fracture toughness and the indentation fracture strength and the applied load, given as

$$K_{Ic} = c\left(\frac{E}{H}\right)^{1/8}\left(\sigma_f W^{1/3}\right)^{3/4} \qquad (5.29)$$

where σ_f is the fracture strength after indentation at a given load and c is an empirical constant (0.59). The advantage of this analysis is that the measurement of crack length is not required.

For fracture toughness measurement of ultrathin films ranging from 100 nm to few micrometers, because of the shallow indentation depths required in the indentation technique, it is difficult to measure a radial crack length even under

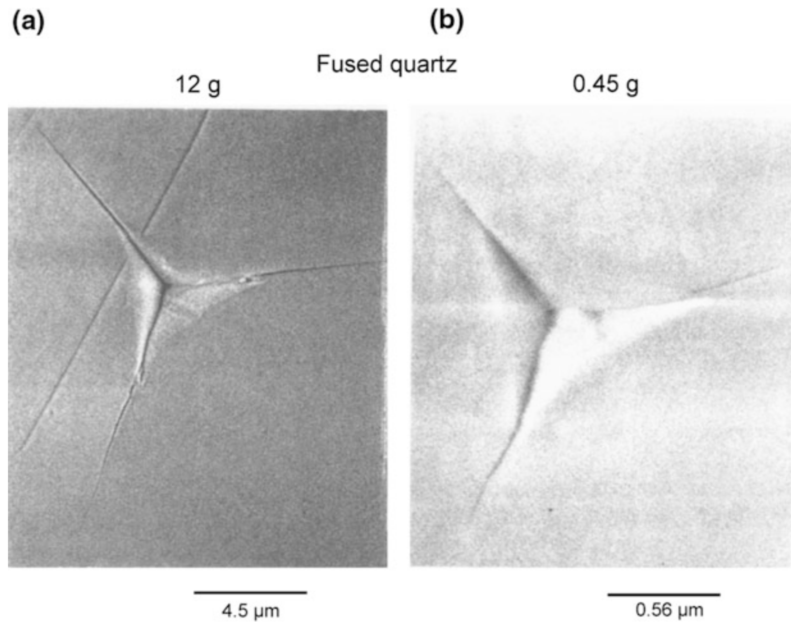

Fig. 5.52 Indentations in fused quartz made with the cube corner indenter showing radial cracking at indentation loads of **a** 12 g and **b** 0.45 g (adapted from Pharr et al. 1993)

Table 5.3 Typical mechanical properties of materials (Pharr et al. 1993)

Material	E (GPa)	H (GPa)	$K_{Ic}(MPa\sqrt{m})$
Soda-lime glass	70	5.5	0.70
Fused quartz	72	8.9	0.58
Si(111)	168	9.3	0.70
Sapphire (111)	403	21.6	2.2
Si_3N_4	300	16.3	4.0

SEM. Li et al. (1997) and Li and Bhushan (1998a, 1999d) developed a novel technique based on nanoindentation in which through-thickness cracking in the coating is detected from a discontinuity observed in the load-displacement curve and energy released during the cracking is obtained from the curve. Based on the energy released, fracture mechanics analysis is then used to calculate fracture toughness. A cube corner is preferred because the through-thickness cracking of hard films can be accomplished at lower loads (Li et al. 1997).

Load-displacement curves of indentations made at 30, 100, and 200 mN peak indentation loads together with the SEM micrographs of indentations on the 400 nm thick FCA carbon coating on silicon are shown in Fig. 5.53 (Li et al. 1997). Steps were found in all loading curves, as shown by arrows in Fig. 5.53a. In the 30-mN SEM micrograph, in addition to several radial cracks, ring-like through-thickness cracking was observed with small lips of material overhanging the edge of indentation. The step at about 23 mN in the loading curves of indentations made at 30 and 100 mN peak indentation loads resulted from the ring-like through thickness cracking. The step at 175 mN in the loading curve of indentation made at 200 mN peak indentation load was caused by spalling.

No steps were observed in the loading curve of indentation made at 20 mN peak indentation load (data not shown here), which suggests that the coating under the indenter was not separated instantaneously from the bulk coating via the ring-like through-thickness cracking but occurred over a period of time. At 30 mN peak indentation load, partial ring-like spalling was observed around the indenter and the other parts of the film

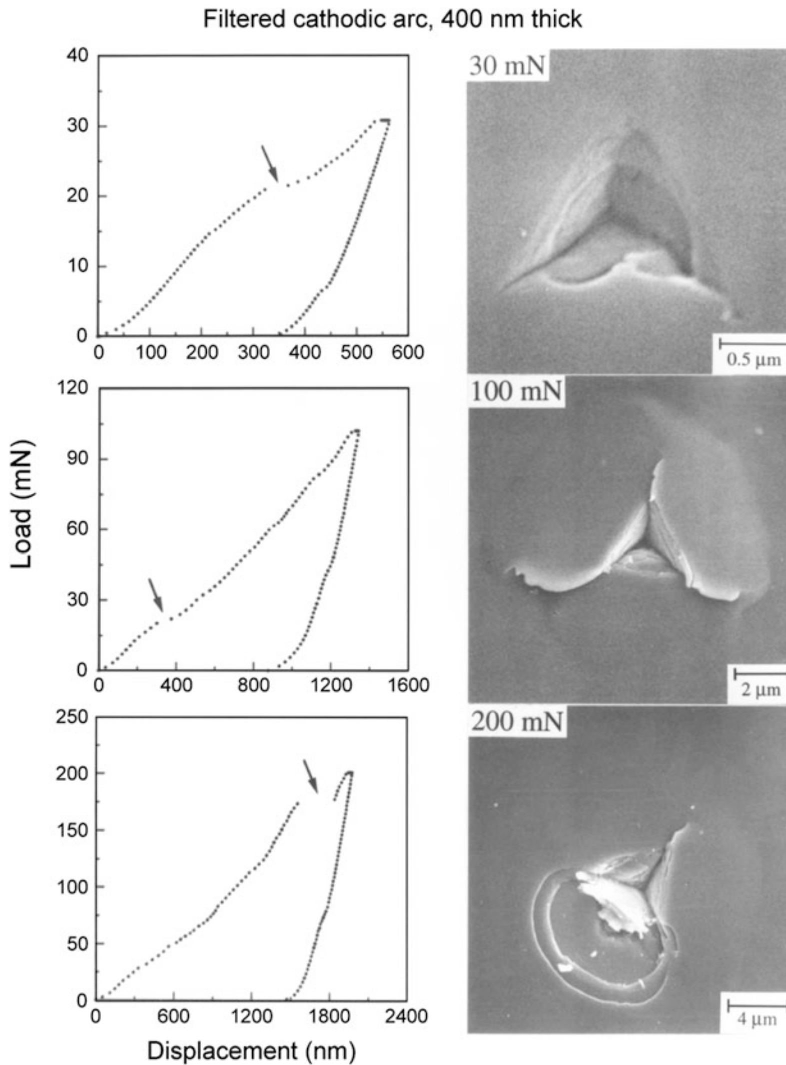

Fig. 5.53 **a** Load-displacement curves of indentations made at 30, 100 and 200 mN peak indentation loads using the cube corner indenter, and **b** the SEM micrographs of indentations on the 400 nm thick DLC coating deposited by filtered cathodic arc on silicon. *Arrows* indicate steps during loading portion of the load-displacement curve (adapted from Li et al. 1997)

bulged upward. This partial ring-like spalling was believed to result in the step in the loading curve. The absence of long steps in the loading curve for uncoated silicon reported, suggesting that the steps in the loading curve on the coating result from the film cracking (Li et al. 1997; Li and Bhushan 1998a). Based on their work, the fracture process progresses in three stages: (1) first ring-like through-thickness cracks form around the indenter by high stresses in the contact area, (2) delamination and buckling occur around the contact area at the film/substrate interface by high lateral pressure, (3) second ring-like through-thickness cracks and spalling are generated by high bending stresses at the edges of the buckled film, see Fig. 5.54a (Li et al. 1997).

In the first stage, if the film under the indenter was separated from the bulk film via the first ring-like through-thickness cracking, a corresponding step will be present in the loading curve. If discontinuous cracks form and the film

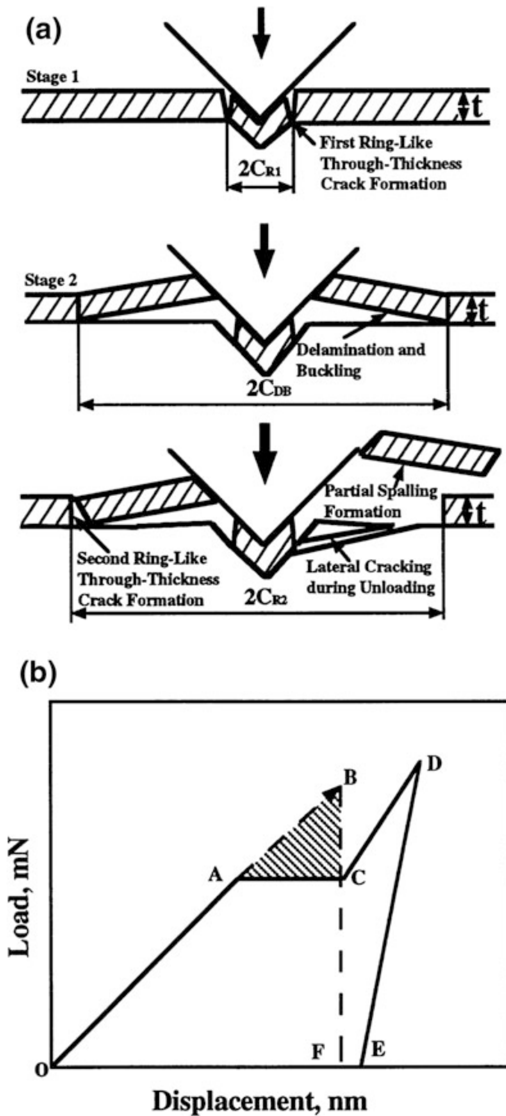

Fig. 5.54 **a** Schematic of various stages in nanoindentation fracture for the film/substrate system, and **b** schematic of a load-displacement curve, showing a step during the loading cycle and associated energy release (adapted from Li et al. 1997)

under the indenter is not separated from the remaining film, no step appeared in the loading curve because the film still supports the indenter and the indenter cannot suddenly advance into the material. In the second stage, the advance of the indenter during the radial cracking, delamination, and buckling was not big enough to form steps in the loading curve because the film around the indenter still supported the indenter, but generated discontinuities that changed the slope of the loading curve with increasing indentation loads. In the third stage, the stress concentration at the end of the interfacial crack could not be relaxed by the propagation of the interfacial crack. With an increase in indentation depth, the height of the bulged film increased. When the height reached a critical value, the bending stresses caused by the bulged film around the indenter resulted in the second ring-like through-thickness crack formation and spalling at the edge of the buckled film, as shown in Fig. 5.54a, which leads to a step in the loading curve (Li et al. 1997). This was a single event and resulted in the separation of the part of the film around the indenter from the bulk film via cracking through films. The step in the loading curve was completely from the film cracking and not from the interfacial cracking or the substrate cracking.

The area under the load-displacement curve is the work performed by the indenter during elastic-plastic deformation of the film/substrate system. The strain energy release in the first/second ring-like cracking and spalling was calculated from the corresponding steps in the loading curve. Figure 5.54b shows a modeled load-displacement curve (Li et al. 1997). OACD is the loading curve. DE is the unloading. Since the first ring-like through-thickness cracking does not always lead to a step in the loading curve in some films, the second ring-like through-thickness crack should be considered. It should be emphasized that the edge of the buckled film is far from the indenter. Therefore, it does not matter if the indentation depth exceeds the film thickness or if deformation of the substrate occurs around the indenter when we measure fracture toughness of the film from the released energy during the second ring-like through-thickness cracking (spalling). Suppose that the second ring-like through-thickness cracking occurs at AC. Now, let us consider the loading curve OAC. If the second ring-like through-thickness crack does not occur, it can be understood that OA will be extended to OB to reach the same displacement as OC. This means

Table 5.4 Mechanical properties for the FCA, IB, ECR-CVD, and SP coatings

Coating	Hardness (Li and Bhushan 1999a) (GPa)	Elastic modulus (Li and Bhushan 1999a) (GPa)	Fracture toughness (Li and Bhushan 1999d) (MPa $m^{1/2}$)	Fatigue Life, N_f^a (Li and Bhushan 2002b) ($\times 10^4$)	Critical load during scratch (Li and Bhushan 1999a) (mN)
FCA	24	280	11.8	2.0	3.8
IB	19	140	4.3	0.8	2.3
ECR-CVD	22	180	6.4	1.2	5.3
SP	15	140	2.8	0.2	1.1
Single-crystal Silicon	11	220	0.75		0.6

Hardness, elastic modulus and fracture toughness were measured on 100-nm think coatings. Fatigue life and critical load during scratch were measured on 20-nm thick coatings

[a] N_f was obtained at a mean load of 10 μN and a load amplitude of 8 μN

that the crack formation changes the loading curve OAB into OAC. For point B, the elastic-plastic energy stored in the film/substrate system should be OBF. For point C, the elastic-plastic energy stored in the film/substrate system should be OACF. Therefore, the energy difference before and after the crack generation is the area of ABC; i.e., this energy stored in ABC will be released as strain energy to create the ring-like through-thickness crack. According to the theoretical analysis by Li et al. (1997), the fracture toughness of thin films can be written as

$$K_{Ic} = \left[\left(\frac{E}{(1-v^2)2\pi C_R}\right)\left(\frac{U}{t}\right)\right]^{1/2} \quad (5.30)$$

where E is the elastic modulus, v is the Poisson's ratio, $2\pi C_R$ is the crack length in the film plane, U the strain energy difference before and after cracking, and t is the film thickness.

Using Eq. 5.30, the fracture toughness of the 0.4 μm thick FCA carbon coating was calculated. The strain energy difference, U, of 7.1 nNm was assessed from the steps in Fig. 5.53a at the peak indentation loads of 200 mN (Li et al. 1997). The loading curve was extrapolated along the tangential direction of the loading curve from the starting point of the step up to reach the same displacement as the step. The area between the extrapolated line and the step was the estimated strain energy difference before and after cracking. C_R of 7.0 μm is measured from the SEM micrograph in Fig. 5.53b. The second ring-like crack is where the spalling occurs. For E of about 300 GPa measured using nanoindentation (Table 5.4) and an assumed value of 0.25 for v, fracture toughness values was calculated as about 11.8 $MPa\sqrt{m}$.

5.6.2 Nanofatigue

Fatigue failure progresses through a material via changes within the material at the tip of a crack, where there is a high stress intensity (Bhushan 1999a; Bhushan and Li 2003). Cyclic fatigue results from cyclic loading of machine components; e.g., the stresses cycle from tension and compression occurs in a loaded rotating shaft. Fatigue also can occur with fluctuating stresses of the same sign, similar to that in a leaf spring or in a dividing board. In a low-flying slider in a head-disk interface, isolated asperity contacts occur during use and the fatigue failure occurs in the multilayered thin-film structure of the magnetic disk (Bhushan 1996).

Li and Chu (1979) developed an indentation fatigue test, called impression fatigue. In this test, a cylindrical indenter with a flat end was pressed onto the surface of the test material with a cyclic load and the rate of plastic zone propagation was measured.

Li and Bhushan (2002b, c) used a depth-sensing nanoindenter using a harmonic

force and a conical diamond indenter typically with a nominal 1 µm radius tip. The CSM technique provides load cycles of a sinusoidal shape at high frequencies that can be used to perform nanoscale fatigue tests. The fatigue behavior of coatings can be studied by monitoring the change in contact stiffness since the contact stiffness is sensitive to damage formation. To obtain deformation and damage during fatigue loading, large amplitude oscillations were used. The numbers of cycles were determined from the elapsed time. Figure 5.55 shows the schematic of a fatigue test on a coating/substrate system using the CSM technique (Li and Bhushan 2002b). Load cycles are applied to the coating, resulting in a cyclic stress; P is the cyclic load, P_{mean} is the mean load, P_o is the oscillation load amplitude, and ω is the oscillation frequency.

The following results can be obtained: (1) endurance limit; i.e., the maximum load below which there is no coating failure for a preset number of cycles; (2) number of cycles at which the coating failure occurs; and (3) changes in contact stiffness measured using the unloading slope of each cycle, which can be used to monitor the propagation of the interfacial cracks during cyclic fatigue process.

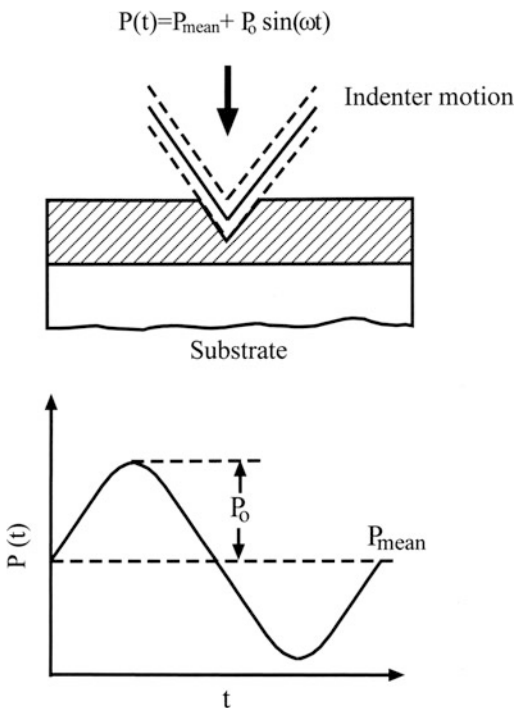

Fig. 5.55 Schematic of a fatigue test on a coating/substrate system using the CSM technique (adapted from Li and Bhushan 2002b)

Figure 5.56a shows the contact stiffness as a function of the number of cycles for 20 nm thick FCA coatings cyclically deformed by various oscillation load amplitudes with a mean load of 10 µN at a frequency of 45 Hz (Li and Bhushan 2002b). At 4 µN load amplitude, no change in contact stiffness was found for all coatings. This indicates that 4 µN load amplitude is not high enough to damage the coatings. At 6 µN load amplitude, an abrupt decrease in contact stiffness was found at a certain number of cycles for each coating, indicating that fatigue damage had occurred. With increasing load amplitude, the number of cycles to failure, N_f, decreased for all coatings. Load amplitude versus N_f, a so-called S-N curve, is plotted in Fig. 5.56b. The critical load amplitude, below which no fatigue damage occurs (an endurance limit), was identified for each coating. This critical load amplitude together with mean load is of critical importance to the design of head-disk interfaces or MEMS/NEMS device interfaces (Bhushan 1996, 2017).

Figure 5.57a shows the high magnification SEM images of 20 nm thick FCA coatings before, at, and after N_f (Li and Bhushan 2002b). In the SEM images, the net-like structure is the gold film coated on the DLC coating, which should be ignored in analyzing the indentation fatigue damage. Before the N_f, no delamination or buckling was found except the residual indentation mark at magnifications up to 1,200,000× using SEM. This suggests that only plastic deformation occurred before the N_f. At the N_f, the coating around the indenter bulged upwards, indicating delamination and buckling. Therefore, it is believed that the decrease in contact stiffness at the N_f results from the delamination and buckling of the coating from the substrate. After the N_f, the buckled coating was broken down around the edge of the buckled area, forming a ring-like crack. The remaining coating overhung at the edge of the buckled area.

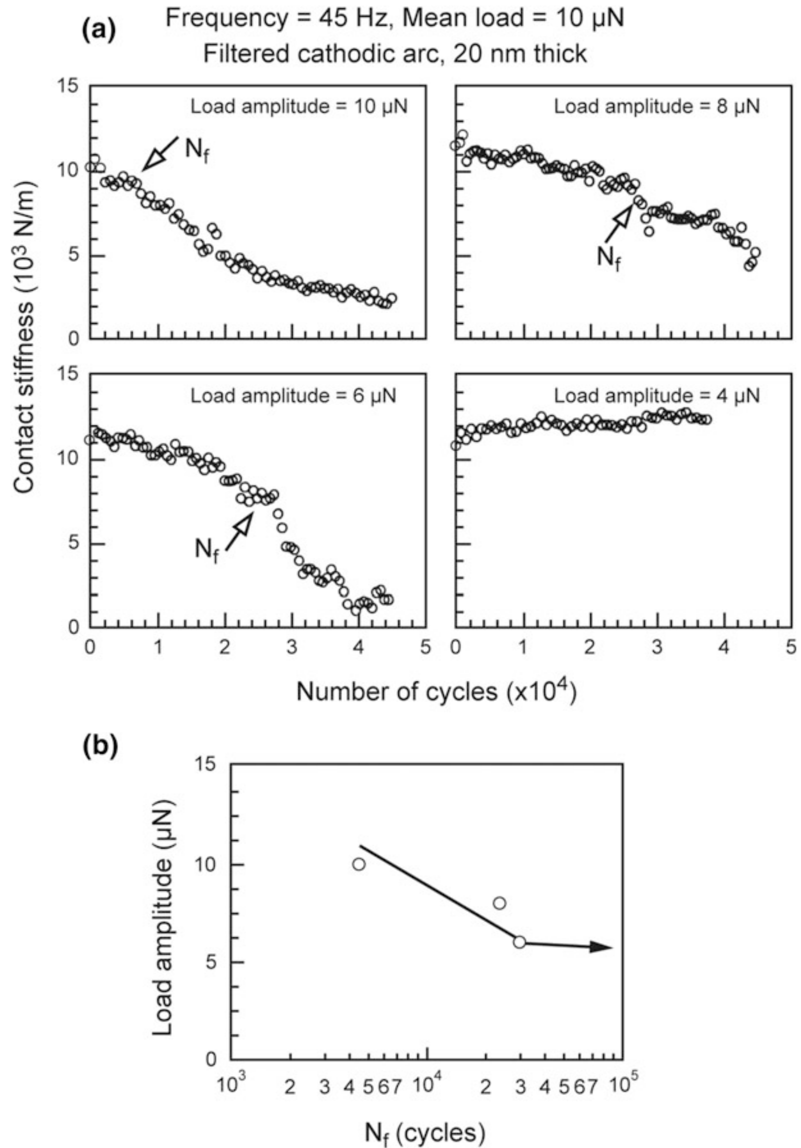

Fig. 5.56 **a** Contact stiffness as a function of the number of cycles for 20-nm thick filtered cathodic arc coatings cyclically deformed by various oscillation load amplitudes with a mean load of 10 μN at a frequency of 45 Hz; and **b** plot of load amplitude versus N_f (adapted from Li and Bhushan 2002b)

It is noted that the indentation size increases with increasing number of cycles. This indicates that deformation, delamination and buckling, and ring-like crack formation occurred over a period of time.

The schematic in Fig. 5.57b shows various stages in the indentation fatigue damage for a coating/substrate system (Li and Bhushan 2002b). Based on this study, three stages in the indentation fatigue damage appear to exist: (1) indentation induced compression; (2) delamination and buckling; (3) ring-like crack formation at the edge of the buckled coating. Residual stresses are often induced in coatings by the deposition process. The model shown in Fig. 5.57b considers a coating with a uniform biaxial residual compression σ_r. In the first stage, indentation induces elastic/plastic deformation, exerting an outward acting pressure on the coating around the indenter. Interfacial defects like voids and impurities act as original cracks. These cracks propagate and link up as the

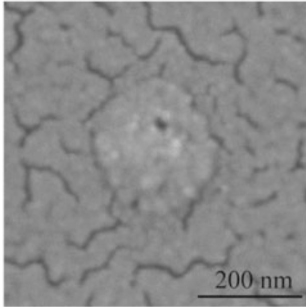

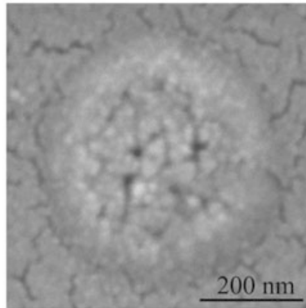

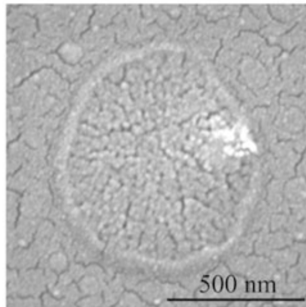

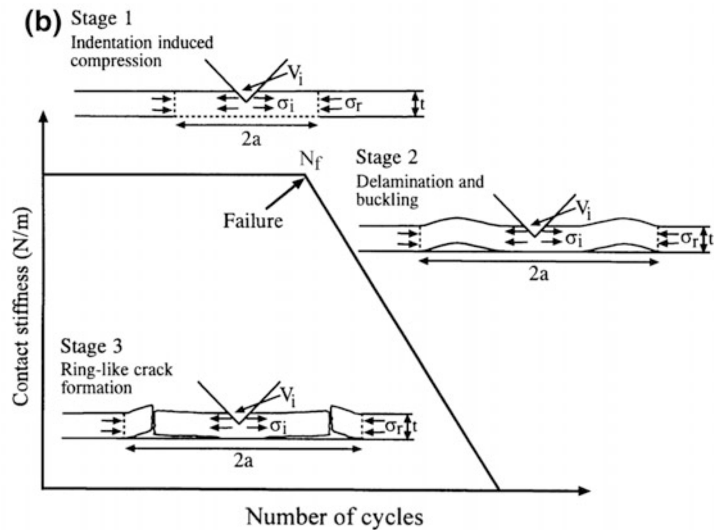

Fig. 5.57 **a** High magnification SEM images of a coatings before, at, and after N_f for 20-nm thick filtered cathodic arc coatings, and **b** schematic of various stages in the indentation fatigue damage for a coating/substrate system (adapted from Li and Bhushan 2002b)

indentation compressive stress increases. At this stage, the coating, which is under the indenter and above the interfacial crack (with a crack length of 2*a*), still maintains a solid contact with the substrate; the substrate still fully supports the coating. Therefore, this interfacial crack does not lead to an abrupt decrease in contact stiffness, but gives a rise to a slight decrease in contact stiffness as shown in Fig. 5.56. The coating above the interfacial crack is treated as a rigidly clamped disk. We assume that the crack radius, *a*, is large compared with the coating thickness *t*. Since the coating thickness ranges from 20 to 5 nm, this assumption is satisfied easily in this

study [radius of the delaminated and buckled area, shown in Fig. 5.57a, is on the order of 100 nm (Li and Bhushan 2002b)]. The compressive stress caused by indentation is given as (Marshall and Evans 1984)

$$\sigma_i = \frac{EV_i}{2\pi t a^2 (1 - v)} \tag{5.31}$$

where v and E are the Poisson's ratio and elastic modulus of the coating, V_i is the indentation volume, t is the coating thickness, and a is the crack radius. With increasing number of cycles, the indentation volume V_i increases. Therefore, the indentation compressive stress σ_i increases accordingly. In the second stage, buckling occurs during the unloading segment of fatigue testing cycle when the sum of indentation compressive stress σ_i and the residual stress σ_r exceed the critical buckling stress σ_b for the delaminated circular section as given by (Evans and Hutchinson 1984)

$$\sigma_b = \frac{\mu^2 E}{12(1 - v^2)} \left(\frac{t}{a}\right)^2 \tag{5.32}$$

where the constant μ equals 42.67 for a circular clamped plate with a constrained center point and 14.68 when the center is unconstrained. The buckled coating acts as a cantilever. In this case, the indenter indents a cantilever rather than a coating/substrate system. This ultrathin coating cantilever has much less contact stiffness than the coating/substrate system. Therefore, the contact stiffness shows an abrupt decrease at the N_f. In the third stage, with an increased number of cycles, the delaminated and buckled size increases, resulting in a further decrease in contact stiffness since the cantilever beam length increases. On the other hand, a high bending stress acts at the edge of the buckled coating. The larger is the buckled size, the higher is the bending stress. The cyclically-bending stress causes fatigue damage at the end of the buckled coating, forming a ring-like crack. The coating under the indenter is separated from the bulk coating (caused by the ring-like crack at the edge of the buckled coating) and the substrate (caused by the delamination and buckling in the second stage). Therefore, the coating under the indenter is not constrained, but is free to move with the indenter during fatigue testing. At this point, the sharp nature of the indenter is lost because the coating under the indenter gets stuck on the indenter. The indentation fatigue experiment results in the contact of a relatively huge, blunt tip with the substrate. This results in a low contact stiffness value.

Compressive residual stresses assist in delamination and buckling. A coating with higher adhesion strength and a less compressive residual stress is required for a higher fatigue life. Interfacial defects should be avoided in the coating deposition process. We know that the ring-like crack formation occurs in the coating. Formation of fatigue cracks in the coating depends upon the hardness and fracture toughness. Cracks are more difficult to form and propagate in the coating with higher strength and fracture toughness.

It is now accepted that long fatigue life in a coating/substrate almost always involves 'living with cracks,' that the threshold or limit condition is associated with the non-propagation of existing cracks or defects, even though these cracks may be undetectable (Suresh 1991). For all coatings studied, at 4 μN, contact stiffness does not change much. This indicates that delamination and buckling did not occur within the number of cycles tested in this study. This is probably because the indentation induced compressive stress was not high enough to allow the cracks to propagate and link up under the indenter or the sum of indentation compressive stress σ_i and the residual stress σ_r did not exceed the critical buckling stress σ_b.

Figure 5.58 and Table 5.4 summarize the hardness, elastic modulus, fracture toughness, fatigue life, and critical load during scratch of the DLC coatings deposited by four deposition techniques—FCA, IB, ECR-CVD, and SP and single-crystal silicon substrate (Li and Bhushan 2002b). A good correlation exists between fatigue life and other mechanical properties. Higher mechanical properties result in a longer fatigue life. The mechanical properties of DLC coatings

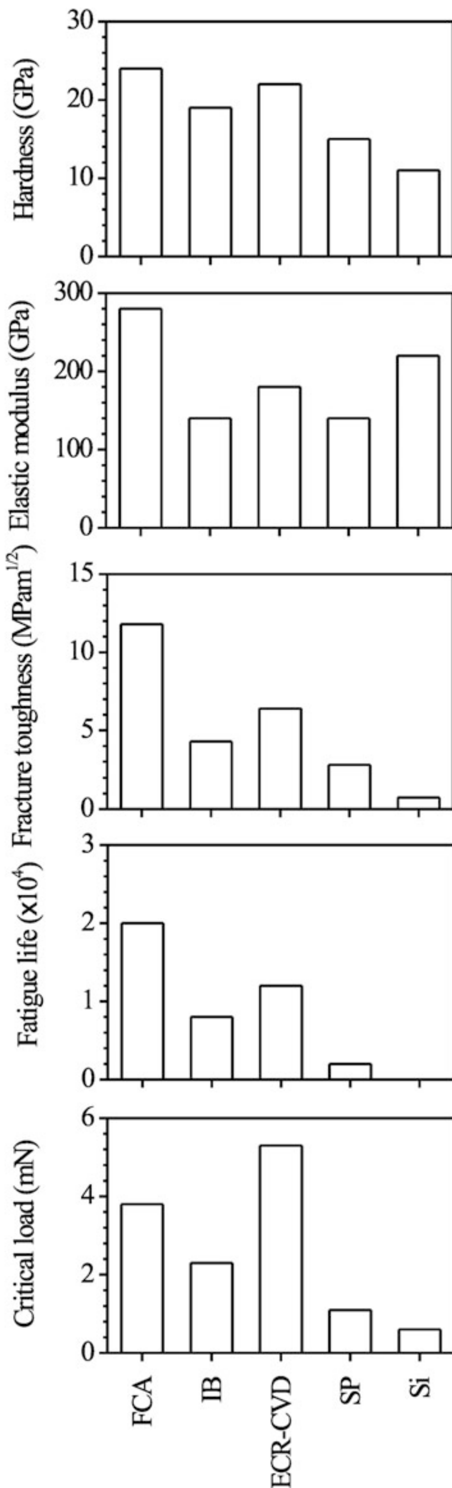

are controlled by the sp^3-to-sp^2 ratio. The sp^3-bonded carbon exhibits the outstanding properties of diamond (Bhushan 1999c). A higher deposition kinetic energy will result in a larger fraction of sp^3-bonded carbon in an amorphous network. Thus, the higher kinetic energy for the FCA could be responsible for its better carbon structure and higher mechanical properties (Bhushan 1999c). Higher adhesion strength between the FCA coating and substrate makes the FCA coating more difficult to delaminate from the substrate.

5.7 Summary

A review of the nanoindentation techniques and various measurement options are presented. Nanoindentation techniques can be used to measure elastic-plastic deformation behavior, hardness, elastic modulus, film-substrate adhesion, residual stresses, time-dependent creep and relaxation properties, fracture toughness, and fatigue of surface layers of bulk materials and thin coatings. The nanoindentation apparatus monitors the load and the position of the indenter relative to the surface of the specimen (displacement) during the indentation process. The load-displacement curve is used to calculate various mechanical properties. A motorized sample stage to move the sample in the lateral direction while loaded against the indenter allows nanoscratch and nanofriction and nanowear tests. A lateral force sensor and/or AE sensor generally are attached to the nanoindenter to monitor changes during the sliding process. The CSM technique in situ probes the mechanical property changes during indentation, and provides useful information for layered materials and nonhomogeneous (such as graded) composites. The CSM

Fig. 5.58 Bar charts summarizing the data of various DLC coatings and single-crystal silicon substrate. Hardness, elastic modulus and fracture toughness were measured on 100-nm thick coatings, and fatigue life and critical load during scratch were measured on 20-nm thick coatings (adapted from Li and Bhushan 2002b)

indentation creep tests can detect creep displacement and stress relaxation at small volumes. Indentation cracking method can be used for measurement of fracture toughness. Load cycles used in the CSM can be used to perform nanoscale fatigue tests.

Nanoindentation techniques can be used at indentation depths as low as about 10 nm. Indentation at an indentation depth less than 20 nm requires sharp indenters with a tip radius less than 20 nm and the use of ultralow loads.

References

Ahn J, Mittal KL, Macqueen RH (1978) Hardness and adhesion of filmed structures as determined by the scratch technique. In: Mittal KL (ed) Adhesion measurement of thin films, thick films, and bulk coatings. STP 640, ASTM, Philadelphia, pp 134–157

Alba S, Loubet JL, Vovelle L (1993) Evaluation of mechanical properties and adhesion of polymer coatings by continous hardness measurements. J Adhesion Sci Technol 7:131–140

Alekhin VP, Berlin GS, Isaev AV, Kalei GN, Merkulov VA, Skvortsov VN, Ternovskii AP, Krushchov MM, Shnyrev GD, Shorshorov MKh (1972) Micromechanical testing by micromechanical testing of materials by microcompression. Zavod Lab 38:619–621

Anonymous (1979) Standard test method for microhardness of materials. ASME designation: E384–73. ASTM, Philadelphia, pp 359–379

Anonymous (1988) Properties of silicon. EMIS data reviews series no. 4. INSPEC, The Institution of Electrical Engineers, London

Anonymous (2014) Keysight Nano Indenter G200 data sheet. Keysight technologies, Santa Rosa, CA

Antis GR, Chantikul P, Lawn BR, Marshall DB (1981) A critical evaluation of indentation techniques for measuring fracture toughness: I direct crack measurements. J Am Ceram Soc 64:533–538

Atkins AG, Silverio A, Tabor D (1966) Indentation hardness and the creep of solids. J Inst Metals 94:369–378

Bell TJ, Field JS, Swain MV (1992) Elastic-plastic characterization of thin films with spherical indentation. Thin Solid Films 220:289–294

Benjamin P, Weaver C (1960) Measurement of adhesion of thin films. Proc R Soc Lond A 254:163–176

Berkovich ES (1951) Three-faceted diamond pyramid for micro-hardness testing. Indus Diamond Rev 11:129–132

Bhattacharya AK, Nix WE (1988a) Finite element simulation of indentation experiments. Int J Solids Struct 24:881–891

Bhattacharya AK, Nix WD (1988b) Analysis of Elastic and plastic deformation associated with indentation testing of the thin films on substrates. Int J Solids Struct 24:1287–1298

Bhushan B (1987) Overview of coating materials, surface treatments, and screening techniques for tribological applications—Part 2: screening techniques. In: Harding WB, DiBari GA (eds) Testing of metallic and inorganic coatings, STP 947. ASTM, Philadelphia, pp 310–319

Bhushan B (1996) Tribology and mechanics of magnetic storage devices, 2nd edn. Springer, New York

Bhushan B (1999a) Nanomechanical properties of solid surfaces and thin films. Handbook of micro/nanotribology, 2nd edn. CRC Press, Boca Raton, pp 443–524

Bhushan B (1999b) Wear and mechanical characterisation on micro- to picoscales using AFM. Int Mater Rev 44:105–117

Bhushan B (1999c) Chemical, mechanical, and tribological characterization of ultra-thin and hard amorphous carbon coatings as thin as 3.5 nm: recent developments. Diam Relat Mater 8:1985–2015

Bhushan B (2001) Modern tribology handbook, vol 1 and 2. CRC Press, Boca Raton

Bhushan B (2011) Nanotribology and nanomechanics I and II. Springer, Heidelberg

Bhushan B (2013a) Principles and applications of tribology, 2nd edn. Wiley, New York

Bhushan B (2013b) Introduction to tribology, 2nd edn. Wiley, New York

Bhushan B (2017) Springer handbook of nanotechnology, 4th edn. Springer International, Switzerland

Bhushan B, Gupta BK (1995) Micromechanical characterization of Ni–P coated aluminum–magnesium, glass, and glass ceramic substrates and finished magnetic thin-film rigid disks. Adv Info Storage Syst 6:193–208

Bhushan B, Gupta BK (1997) Handbook of tribology: materials, coatings and surface treatments. McGraw Hill, New York (1991); Reprint edition (1997), Krieger Publishing Co., Malabar

Bhushan B, Koinkar VN (1994) Nanoindentation hardness measurements using atomic force microscopy. Appl Phys Lett 64:1653–1655

Bhushan B, Li X (1997) Micromechanical and tribological characterization of doped single-crystal silicon and polysilicon films for microelectromechanical system devices. J Mater Res 12:54–63

Bhushan B, Li X (2003) Nanomechanical characterisation of solid surfaces and thin films. Int Mater Rev 48:125–164

Bhushan B, Patton ST (1996) Pole tip recession studies of hard carbon-coated thin-film tape heads. J Appl Phys 79:5916–5918

Bhushan B, Venkatesan S (2005) Effective mechanical properties of layered rough surfaces. Thin Solid Films 473:278–295

Bhushan B, Landesman AL, Shack RV, Vukobratovich D, Walters VS (1985) Instrument for testing thin films

such as magnetic tapes. IBM Tech Discl Bull 28:2975–2976

Bhushan B, Williams VS, Shack RV (1988) In-situ nanoindentation hardness apparatus for mechanical characterization of extremely thin films. ASME J Tribol 110:563–571

Bhushan B, Gupta BK, Azarian MH (1995) Nanoindentation, microscratch, friciton and wear studies of coatings for contact recording applications. Wear 181–183:743–758

Bhushan B, Kulkarni AV, Bonin W, Wyrobek JT (1996a) Nanoindentation and picoindentation measurements using a capacitive transducer system in atomic force microscopy. Philos Mag 74:1117–1128

Bhushan B, Chyung K, Miller RA (1996b) Micromechanical property measurements of glass and glass-ceramic substrates for magnetic thin-film rigid disks for gigabit recording. Adv Info Storage Syst 7:3–16

Bhushan B, Theunissen GSAM, Li X (1997) Tribological studies of chromium oxide films for magnetic recording applications. Thin Solid Films 311:67–80

Bhushan B, Luo D, Schricker SR, Sigmund W, Zauscher S (2014) In: Handbook of nanomaterials properties, vol 1–2. Springer, Heidelberg

Blau PJ, Lawn BR (eds) (1986) Microindentation techniques in materials science and engineering, STP 889. ASTM, Philadelphia

Blau PJ, Oliver WC, Snead L (1997) The scanning micro-sclerometer: a new method for scratch hardness mapping. Tribol Int 30:483–490

Bolshakov A, Oliver WC, Pharr GM (1996) Influences of stress on the measurement of mechanical properties using nanoindentation. II. Finite element simulations. J Mater Res 11:760–768

Buckle H (1973) Use of the hardness test to determine material properties. In: *The Science of Hardness Testing and its Research Applications* (Westbrook JW, and Conrad H, eds.), pp. 453–491, Am. Soc. Metals, Metals Park, Ohio.

Bull SJ, Rickerby DS (1990) New developments in the modelling of the hardness and scratch adhesion of thin films. Surf Coatings Technol 42:149–164

Bulychev SI, Alekhin VP, Shorshorov MKh, Ternovskii AP, Shnyrev GD (1975) Determining Young's Modulus from the indenter penetration diagram. Zavod Lab 41:11137–11140

Bulychev SI, Alekhin VP, Shorshorov MKh (1979) Studies of physico-mechanical properties in surface layers and microvolumes of materials by the method of continuous application of an indenter. Fizika Khim Obrab Materialov, No 5

Burnett PJ, Rickerby DS (1987a) The relationship between hardness and scratch adhesion. Thin Solid Films 154:403–416

Burnett PJ, Rickerby DS (1987b) The mechanical properties of wear resistant coatings I: modelling of hardness behavior. Thin Solid Films 148:41–50

Callahan DL, Morris JC (1992) The extent of phase transformation in silicon hardness indentations. J Mater Res 7:1614–1617

Campbell DS (1970) Mechanical properties of thin films. In: Maissel LI, Glang R (eds) Handbook of Thin Film Technology (Chap. 12). McGraw-Hill, New York

Chantikul P, Anstis GR, Lawn BR, Marshall DB (1981) A critical evaluation of indentation techniques for measuring fracture toughness: II, strength method. J Am Ceram Soc 64:539–543

Chiang SS, Marshall DB, Evans AG (1981) Simple method for adhesion measurement. In: Pask J, Evans AG (eds) Surfaces and interfaces in ceramics and ceramic-metal systems. Plenum, New York, pp 603–612

Chiang SS, Marshall DB, Evans AG (1982) The response of solids to elastic/plastic indentation: I. stresses and residual stresses. J Appl Phys 53:298–311

Cho D, Bhushan B (2016) Nanofriction and nanowear of polypropylene, polyethylene terephthalate, and high-density polyethylene during sliding. Wear 352–353:18–23

Chu SNG, Li JCM (1977) Impression creep: a new creep test. J Mater Sci 12:2200–2208

Chu SNG, Li JCM (1980) Localized stress relaxation by impression testing. Mater Sci Eng 45:167–171

Cook RF, Pharr GM (1990) Direct observation and analysis of indentation cracking in glasses and ceramics. J Am Ceram Soc 73:787–817

Doerner MF, Nix WD (1986) A method for interpreting the data from depth-sensing indentation instruments. J Mater Res 1:601–609

Doerner MF, Gardner DS, Nix WD (1986) Plastic properties of thin films on substrates as measured by submicron indentation hardness and substrate curvature techniques. J Mater Res 1:845–851

Evans AG, Hutchinson JW (1984) On the mechanics of delamination and spalling in compressed films. Int J Solids Struct 20:455–466

Fabes BD, Oliver WC, McKee RA, Walker FJ (1992) The determination of film hardness from the composite response of film and substrate to nanometer scale indentation. J Mater Res 7:3056–3064

Fischer-Cripps AC (2002) Nanoindentation. Springer, New York

Fleck NA, Muller GM, Ashby MF, Hutchinson JW (1994) Strain gradient plasticity: theory and experiments. Acta Metall Mater 42:475–487

Gane N, Cox JM (1970) The micro-hardness of metals at very low loads. Philos Mag 22:881–891

Goken M, Kempf M (2001) Pop-ins in Nanoindentation—The initial yield point. Z Metallikd 92:1061–1067

Greene JE, Woodhouse J, Pestes M (1974) A technique for detecting critical loads in the scratch test for thin-film adhesion. Rev Sci Instrum 45:747–749

Gupta BK, Bhushan B (1994) The nanoindentation studies of ion implanted silicon. Surf Coat Technol 68(69):564–570

Gupta BK, Bhushan B (1995a) Micromechanical properties of amorphous carbon coatings deposited by different deposition techniques. Thin Solid Films 270:391–398

Gupta BK, Bhushan B (1995b) Mechanical and tribological properties of hard carbon coatings for magnetic recording heads. Wear 190:110–122

Gupta BK, Chevallier J, Bhushan B (1993) Tribology of ion bombarded silicon for micromechanical applications. ASME J Tribol 115:392–399

Gupta BK, Bhushan B, Chevallier J (1994) Modification of tribological properties of silicon by boron ion implantation. Tribol Trans 37:601–607

Hainsworth SV, Chandler HW, Page TF (1996) Analysis of nanoindentation load-displacement loading curves. J Mater Res 14:2283–2295

Hainsworth SV, McGurk MR, Page TF (1998) The effect of coating cracking on the indentation response of thin hard-coated systems. Surf Coat Technol 102:97–107

Hannula SP, Wanagel J, Li CY (1986) A miniaturized mechanical testing system for small scale specimen testing. In: Corwin WR, Lucas GE (eds) The use of small-scale specimens for testing irradiated material, STP 888. ASTM, Philadelphia, pp 233–251

Hay JC, Bolshakov A, Pharr GM (1999) A critical examination of the fundamental relations used in the analysis of nanoindentation data. J Mater Res 14:2296–2305

Heavens OS (1950) Some factors influencing the adhesion of films produced by vacuum evaporation. J Phys Rad 11:355–360

Henshall JL, Brookes CA (1985) The measurement of K_{Ic} in single crystal SiC using the indentation method. J Mater Sci Lett 4:783–786

Hong S, Weihs TP, Bravman JC, Nix WD (1990) Measuring stiffnesses and residual stresses of silicon nitride in thin films. J Electron Mater 19:903

Jacobson S, Jonsson B, Sundquist B (1983) The use of fast heavy ions to improve thin film adhesion. Thin Solid Films 107:89–98

Johnson KL (1985) Contact mechanics. Cambridge University Press, Cambridge

Joslin DL, Oliver WC (1990) A new method for analyzing data from continuous depth-sensing microindentation tests. J Mater Res 5:123–126

King RB (1987) Elastic analysis of some punch problems for layered medium. Int J Solids Struct 23:1657–1664

Korsunsky AM, McGurk MR, Bull SJ, Page TF (1998) On the hardness of coated systems. Surf Coat Technol 99:171–183

Kulkarni AV, Bhushan B (1996a) Nanoscale mechanical property measurements using modified atomic force microscopy. Thin Solid Films 290–291:206–210

Kulkarni AV, Bhushan B (1996b) Nano/picoindentation measurements on single-crystal aluminum using modified atomic force microscopy. Mater Lett 29:221–227

Kulkarni AV, Bhushan B (1997) Nanoindentation measurements of amorphous carbon coatings. J Mater Res 12:2707–2714

Kumar A, Bhushan B (2015) Nanomechanical, nanotribological, and macrotribological characterization of hard coatings and surface treatment of H-13 steel. Tribol Int 81:149–158

LaFontaine WR, Yost B, Black RD, Li CY (1990) Indentation load relaxation experiments with indentation depth in the submicron range. J Mater Res 5:1206–2100

LaFontaine WR, Paszkiet CA, Korhonen MA, Li CY (1991) Residual stress measurements of thin aluminum metallizations by continuous indentation and X-ray stress measurement techniques. J Mater Res 6:2084–2090

Lankford J (1981) Threshold-microfracture during elastic/plastic indentation of ceramics. J Mater Sci 16:1177–1182

Laugier M (1981) The development of scratch test technique for the determination of the adhesion of coating. Thin Solid Films 76:289–294

Laursen TA, Simo JC (1992) A study of the mechanics of microindentation using finite elements. J Mater Res 7:618–626

Lawn B (1993) Fracture of brittle solids, 2nd edn. Cambridge University Press, Cambridge

Lawn B, Wilshaw R (1975) Review indentation fracture: principles and applications. J Mater Sci 10:1049–1081

Lawn BR, Evans AG, Marshall DB (1980) Elastic/plastic indentation damage in ceramics: the median/radial crack system. J Am Ceram Soc 63:574–581

Li JCM, Chu SNG (1979) Impression fatigue. Scr Metall 13:1021–1026

Li X, Bhushan B (1998a) Measurement of fracture toughness of ultra-thin amorphous carbon films. Thin Solid Films 315:214–221

Li X, Bhushan B (1998b) Micromechanical and tribological characterization of hard amorphous carbon coatings as thin as 5 nm for magnetic recording heads. Wear 220:51–58

Li X, Bhushan B (1999a) Micro/nanomechanical and tribological characterization of ultra-thin amorphous carbon coatings. J Mater Res 14:2328–2337

Li X, Bhushan B (1999b) Mechanical and tribological studies of ultra-thin hard carbon overcoats for magnetic recording heads. Z Metallkd 90:820–830

Li X, Bhushan B (1999c) Micro/nanomechanical characterization of ceramic films for microdevices. Thin Solid Films 340:210–217

Li X, Bhushan B (1999d) Evaluation of fracture toughness of ultrathin and hard amorphous carbon coatings deposited by different deposition techniques. Thin Solid Films 355–356:330–336

Li X, Bhushan B (2000a) Development of continuous stiffness measurement technique for composite magnetic tapes. Scr Mater 42:929–935

Li X, Bhushan B (2000b) Continuous stiffness measurement and creep behavior of composite magnetic tapes. Thin Solid Films 377–378:401–406

Li X, Bhushan B (2001a) Continuous stiffness measurements of layered materials used in magnetic storage devices. J Info Storage Proc Syst 3:131–142

Li X, Bhushan B (2001b) Dynamic mechanical characterization of magnetic tapes using nanoindentation techniques. IEEE Trans Mag 37:1616–1619

Li X, Bhushan B (2002a) A review of nanoindentation continuous stiffness measurement and its applications. Mater Charact 48:11–36

Li X, Bhushan B (2002b) Development of a nanoscale fatigue measurement technique and its application to ultrathin amorphous carbon coatings. Scr Mater 47:473–479

Li X, Bhushan B (2002c) Nanofatigue studies of ultrathin hard carbon overcoats used in magnetic storage devices. J Appl Phys 91:8334–8336

Li X, Bhushan B (2003) Fatigue studies of nanoscale structures for MEMS/NEMS applications using nanoindentation techniques. Surf and Coat Technol 163–164:521–526

Li WB, Henshall JL, Hooper RM, Easterling KE (1991) The mechanism of indentation creep. Acta Metall Mater 39:3099–3110

Li X, Diao D, Bhushan B (1997) Fracture mechanisms of thin amorphous carbon films in nanoindentation. Acta Mater 45:4453–4461

Li X, Bhushan B, Inoue M (2001) Time-dependent mechanical properties and tribological behavior of magnetic tapes. Wear 251:1150–1158

Li X, Bhushan B, Takashima K, Baek CS, Kim YK (2003) Mechanical characterization of micro/nanoscale structures for MEMS/NEMS applications using nanoindentation techniques. Ultramicroscopy 97:481–494

Lin MR, Ritter JE, Rosenfeld L, Lardner TJ (1990) Measuring the interfacial shear strength of thin polymer coatings on glass. J Mater Res 5:1110–1117

Loubet JL, Georges JM, Marchesini O, Meille G (1984) Vickers indentation curves of magnesium oxide (MgO). ASME J Tribol 106:43–48

Loubet JL, Bauer M, Tonck A, Bec S, Gauthier-Manuel B (1993) Nanoindentation with a surface force apparatus. In: Nastasi M, Parkin DM, Gleiter H (eds) Mechanical properties and deformation behavior of materials having ultra-fine microstructures. Kluwer Academic Pub., Dordrecht, pp 429–447

Lysaght VE (1949) Indentation Hardness testing. Reinhold, New York

Maharaj D, Bhushan B (2015) Friction, wear, and mechanical behavior of nano-objects on the nanoscale. Mater Sci Eng R 95:1–43

Marshall DB, Evans AG (1984) Measurement of adherence of residual stresses in thin films by indentation. I. Mechanics of interface delamination. J Appl Phys 15:2632–2638

Marshall DB, Lawn BR (1979) Residual stress effects in sharp contact cracking part 1 indentation fracture mechanics. J Mater Sci 14:2001–2012

Marshall DB, Oliver WC (1987) Measurement of interfacial mechanical properties in fiber-reinforced ceramic composites. J Am Ceram Soc 70:542–548

Mayo MJ, Nix WD (1988) A micro-indentation study of superplasticity in Pb, Sn, and Sn–38 Wt% Pb. Acta Metall 36:2183–2192

McGurk MR, Page TF (1999) Using the P-δ2 analysis to deconvolute the nanoindentation response of hard-coated systems. J Mater Res 14:2283–2295

Mehrotra PK, Qunito DT (1985) Techniques for evaluating mechanical properties of hard coatings. J Vac Sci Technol A 3:2401–2405

Mittal KL (ed) (1978) Adhesion measurements on thin coatings, thick coatings, and bulk coatings, STP640. ASTM, Philadelphia

Mott BW (1957) Microindentation hardness testing. Butterworths, London

Mulhearn TO, Tabor D (1960) Creep and hardness of metals: a physical study. J Inst Metals 87:7–12

Nastasi M, Parkin DM, Gleiter H (eds) (1993) Mechanical properties and deformation behavior of materials having ultra-fine microstructures. Kluwer Academic Pub, Dordrecht

Newey D, Wilkins MA, Pollock HM (1982) An Ultra-low-load penetration hardness tester. J Phys E Sci Instrum 15:119–122

Nix WD (1989) Mechanical properties of thin films. Metall Trans A 20:2217–2245

Oliver WC (2001) Alternative technique for analyzing instrumented indentation data. J Mater Res 16:3202–3206

Oliver WC, Pharr GM (1992) An improved technique for determining hardness and elastic modulus using load and displacement sensing indentation experiments. J Mater Res 7:1564–1583

Oliver WC, Hutchings R, Pethica JB (1986) Measurement of hardness at indentation depths as small as 20 nm. In: Blau PJ, Lawn BR (eds) Microindentation techniques in materials science and engineering, STP 889. ASTM, Philadelphia, pp 90–108

O'Neill H (1967) Hardness measurement of metals and alloys. Chapman and Hall, London

Page TF, Oliver WC, McHargue CJ (1992) The deformation behavior of ceramic crystals subjected to very low load (nano)indentations. J Mater Res 7:450–473

Palacio M, Bhushan B (2010) Nanomechanical characterization of adaptive optics components in microprojectors. J Micromech Microeng 20:064002

Palacio MLB, Bhushan B (2013) Depth-sensing indentation of nanomaterials and nanostructures. Mater Charact 78:1–20

Palacio M, Bhushan B, Ferrell N, Hansford D (2007a) Nanomechanical characterization of polymer beam structures for BioMEMS applications. Sens Actuators A 135:637–650

Palacio M, Bhushan B, Ferrell N, Hansford D (2007b) Adhesion properties of polymer/silicon interfaces for biological micro-/nanoelectromechanical systems applications. J Vac Sci Technol A 25:1275–1284

Palmquist S (1957) Method of determining the toughness of brittle materials, particularly sintered carbides. Jernkontorets Ann 141:300–307

Patton ST, Bhushan B (1996) Micromechanical and tribological characterization of alternate pole tip materials for magnetic recording heads. Wear 202:99–109

Perry AJ (1981) The adhesion of chemically vapour-deposited hard coatings on steel—The scratch test. Thin Solid Films 78:77–93

Perry AJ (1983) Scratch adhesion testing of hard coatings. Thin Solid Films 197:167–180

Pethica JB, Oliver WC (1989) Mechanical properties of nanometer volumes of material: use of the elastic response of small area indentations. In: Bravman JC, Nix WD, Barnett DM, Smith DA (eds) Thin films: stresses and mechanical properties, vol 130. Mat. Res. Soc., Pittsburgh, pp 13–23

Pethica JB, Hutchings R, Oliver WC (1983) Hardness measurements at penetration depths as small as 20 nm. Philos Mag A 48:593–606

Pharr GM (1992) The anomalous behavior of silicon during nanoindentation. In: Nix WD, Bravman JC, Arzt E, Freund LB (eds) Thin film: stresses and mechanical properties III, vol 239. Mater. Res. Soc., Pittsburgh, pp 301–312

Pharr GM (1998) Measurement of mechanical properties by ultra-low load indentation. Mat Sci Eng A 253:151–159

Pharr GM, Oliver WC, Clarke DR (1989) Hysteresis and discontinuity in the indentation load-displacement behavior of silicon. Scr Metall 23:1949–1952

Pharr GM, Oliver WC, Clarke DR (1990) The mechanical behavior of silicon during small-scale indentation. J Electron Mater 19:881–887

Pharr GM, Oliver WC, Brotzen FR (1992) On the generality of the relationship among contact stiffness, contact area, and elastic modulus during indentation. J Mater Res 7:613–617

Pharr GM, Harding DS, Oliver WC (1993) Measurement of fracture toughness in thin films and small volumes using nanoindentation methods. In: Nastasi M, Parkin DM, Gleiter H (eds) Mechanical properties and deformation behavior of materials having ultra-fine microsctructures. Kluwer Academic, Dordrecht, pp 449–461

Randall NX, Cristoph R, Droz S, Julia-Schmutz C (1996) Localised micro-hardness measurements with a combined scanning force microscope/nanoindentation system. Thin Solid Films 290–291:348–354

Raman V, Berriche R (1992) An investigation of the creep processes in tin and aluminum using a depth-sensing indentation technique. J Mater Res 7:627–638

San Juan J, No ML, Schuh CA (2009) Nanoscale shape-memory alloys for ultrahigh mechanical damping. Nat Nanotechnol 4:415–419

Sargent PM (1986) Use of the indentation size effect on microhardness of materials characterization. In: Blau PJ, Lawn BR (eds) Microindentation techniques in materials science and engineering, STP 889. ASTM, Philadelphia, pp 160–174

Scruby CB (1987) An introduction to acoustic emission. J Phys E Sci Instrum 20:946–953

Sekler J, Steinmann PA, Hintermann HE (1988) The scratch test: different critical load determination techniques. Surf Coat Tech 36:519–529

Shih CW, Yang M, Li JCM (1991) Effect of tip radius on nanoindentation. J Mater Res 6:2623–2628

Sneddon IN (1965) The relation between load and penetration in the axisymmetric boussinesq problem for a punch of arbitrary profile. Int J Eng Sci 3:47–57

Stilwell NA, Tabor D (1961) Elastic recovery of conical indentation. Proc Phys Soc 78:169–179

Stone D, LaFontaine WR, Alexopoulos PS, Wu TW, Li CY (1988) An investigation of hardness and adhesion of sputter-depostied aluminum on silicon by utilizing a continuous indentation test. J Mater Res 3:141–147

Sundararajan S, Bhushan B (2001) Development of a continuous microscratch technique in an atomic force microscope and its application to study scratch resistance of ultra-thin hard amorphous carbon coatings. J Mater Res 16:437–445

Sundararajan S, Bhushan B, Namazu T, Isono Y (2002) Mechanical property measurements of nanoscale structures using an atomic force microscope. Ultramicroscopy 91:111–118

Suresh S (1991) Fatige of materials. Cambridge University Press, Cambridge

Swadener JG, George EP, Pharr GM (2002) The correlation of the indentation size effect measured with indenters of various shapes. J Mech Phys Solids 50:681–694

Swain MV, Hagan JT, Field JE (1977) Determination of the surface residual stresses in tempered glasses by indentation fracture mechanics. J Mater Sci 12:1914–1917

Syed Asif SA, Pethica JB (1997) Nano scale creep and the role of defects. In: Gerberich WW, Gao H, Sundgren JE, Baker SP (eds) Thin films: stresses and mechanical properties IV. Mat Res. Soc. Pittsburgh, PA (MRS Symp Proc 436:201–206)

Tabor D (1951) The hardness of metals. Clarendon Press, Oxford

Tabor D (1970) The hardness of solids. Rev Phys Technol 1:145–179

Tangena AG, Hurkx GAM (1986) The determination of stress-strain curves of thin layers using indentation tests. ASME J Eng Mat Technol 108:230–232

Ternovskii AP, Alekhin VP, Shorshorov MKh, Khrushchov MM, Skvortsov VN (1973) Micromechanical testing of materials by depression. Zavod Lab 39:1620–1624

Tsui TY, Pharr GM (1999) Substrate effects on nanoindentation mechanical property measurement of soft films on hard substrates. J Mater Res 14:292–301

Tsui TY, Oliver WC, Pharr GM (1996) Influences of stress on the measurement of mechanical properties using nanoindentation. I. Experimental studies in an aluminum alloy. J Mater Res 11:752–759

Tsukamoto Y, Yamaguchi H, Yanagisawa M (1987) Mechanical properties of thin films: measurements of ultramicroindentation hardness, Young's modulus and internal stresses. Thin Solid Films 154:171–181

Valli J (1986) A review of adhesion test method for thin hard coatings. J Vac Sci Technol A4:3007–3014

VanLandingham MR, Villarrubia JS, Guthrie WF, Meyers GF (2001) Nanoindentation of polymers: an overview. Macromol Symp 167:15–43

Venkataraman S, Kohlstedt DL, Gerberich WW (1992) Microscratch analysis of the work of adhesion for Pt thin films on NiO. J Mater Res 1:1126–1132

Vinci RP, Vlassak JJ (1996) Mechanical behavior of thin films. Annu Rev Mater Sci 26:431–462

Vitovec FH (1986) Stress and load dependence of microindentation hardness. In: Blau PJ, Lawn BR (eds) Microindentation techniques in materials science and engineering, STP 889. ASTM, Philadelphia, pp. 175–185

Walker WW (1973) Indentation creep at low homologous temperatures. In: *The Science of Hardness Testing and its Research Applications* (Westbrook JH, and Conrad H, eds.), pp. 258–273, Am. Soc. Metals, Metals Park, Ohio.

Wei G, Bhushan B, Ferrell N, Hansford D (2005) Microfabrication and nanomechanical characterization of polymer mems for biological applications. J Vac Sci Technol A 23:811–819

Weihs TP, Lawrence CW, Derby CB, Pethica JB (1992) Acoustic emissions during indentation tests. In: Nix WD, Bravman JC, Arzt E, Freund LB (eds) Thin films: stresses and mechanical properties III. Mat. Res. Soc., Pittsburgh (Symp Proc 239: 361–370)

Westbrook JH (1957) Microhardness testing at high temperatures. Proc Am Soc Test Mater 57:873–895

Westbrook JH, Conrad H (eds) (1973) The science of hardness and its research applications. Am Soc Metals, Metals Park

Whitehead AJ, Page TF (1992) Nanoindentation studies of thin film coated systems. Thin Solid Films 220:277–283

Wierenga PE, Franken AJJ (1984) Ultramicroindentation apparatus for the mechanical characterization of thin films. J Appl Phys 55:4244–4247

Wierenga PE, van der Linden JHM (1986) Quasistatic and dynamic indentation measurements on magnetic tapes. In: Bhushan B, Eiss NS (eds) Tribology and mechanics of magnetic storage systems, vol 3 (SP-21). ASLE, Park Ridge, pp 31–37

Williams VS, Landesman AL, Shack RV, Vukobratovich D, Bhushan B (1988) In situ microviscoelastic measurements by polarization-interferometric monitoring of indentation depth. Appl Opt 27:541–546

Wu TW (1991) Microscratch and load relaxation tests for ultra-thin films. J Mater Res 6:407–426

Wu TW, Hwang C, Lo J, Alexopoulos P (1988) Microhardness and microstructure of ion-beam-sputtered, nitrogen doped nife films. Thin Solid Films 166:299–308

Wu TW, Shull AL, Berriche R (1991) Microindentation fatigue tests on submicron carbon films. Surf Coat Tech 47:696–709

Yanagisawa M, Motomura Y (1987) An ultramicro indentation hardness tester and its application to thin films. Lub Eng 43:52–56

Young WC, Budynas RG, Sadegh AM (2012) Roark's formulas for stress and strain, 8th edn. McGraw-Hill, New York